

# Matrix Equations Models For Nonlinear Dynamic Analysis of Two-Dimensional And Three-Dimensional RC Structures With Lateral Load Resisting Cantilever Elements

Assaf Shmerling (✉ [assafs@bgu.ac.il](mailto:assafs@bgu.ac.il))

Ben-Gurion University of the Negev <https://orcid.org/0000-0002-3550-3578>

---

## Research Article

**Keywords:** vibration and dynamics, nonlinear dynamic analysis, reinforced concrete structures, 28 cyclic loading, structural mechanics

**Posted Date:** June 10th, 2021

**DOI:** <https://doi.org/10.21203/rs.3.rs-560663/v1>

**License:**  This work is licensed under a Creative Commons Attribution 4.0 International License.

[Read Full License](#)

---



30 1. *Introduction*

31 Various nonlinear dynamic analysis of structures methods have been developed for  
32 evaluating the dynamic response of buildings under cyclic loading. Wong and Wang[1] modified  
33 the classical force analogy method for moment-resisting frame models by introducing static  
34 condensation, which reduced the degrees of freedom (DOFs) and resolved in a veritable mass  
35 matrix – essential to the force analogy method. Li and Li[2] utilized the force analogy method to  
36 analyze the dynamic response of moment-resisting frame structures with energy dissipation  
37 devices. Sun et al.[3] propose their numerical substructure method for performing seismic analysis  
38 and determining the locally yielded lateral load resisting elements. Chang et al.[4] presented the  
39 simplified generalized conforming mixed quadrilateral for membrane elements. Pozo et al. [5]  
40 suggested using the Bouc-Wen model to determine the position and acceleration of dynamic systems  
41 under cyclic loads. Finally, Liu and Yu [6] addressed the previously studied quasi-zero stiffness  
42 vibration isolator and enhanced the dynamic model by referring to the damping effects. This paper  
43 aims to develop a novel matrix equations model and formulates the symmetric stiffness and mass  
44 matrices of continuous cantilever structures. The matrix equations models are suitable for control  
45 engineering and nonlinear dynamic analysis purposes.

46 The mechanical understanding of structural elements under cyclic loading has significantly  
47 improved in recent decades. The paper of Fragiadakis and Papadrakakis[7] alone overviews dozens  
48 of finite element and computation methods for addressing the inelastic response of solely beam-  
49 column members. The review paper by Younesian et al. [8] describes methods developed in recent  
50 decades for analyzing nonlinear dynamic systems of various model types (e.g., discrete,  
51 multilayered, discontinuous). Mata et al.[9] showcase dozens of numerical approaches developed  
52 during a 20 years gap for evaluating the response of RC structures with energy dissipation devices.  
53 Very recently, Castaldo et al. [10] and Gino et al. [11] addressed the uncertainties of epistemic nature  
54 in cyclically loaded reinforced concrete systems and propose using a partial safety factor  
55 corresponding to the resistance model uncertainties in the use of nonlinear finite element analyses.  
56 Ismail et al.[12] present a broad survey on the development and utilization of the Bouc-Wen-based  
57 models for the nonlinear analysis of structural elements, mechanical systems, soil behavior, and  
58 more. The paper exemplifies the extent to which the Bouc-Wen-based models are popular and useful  
59 in addressing structural elements' nonlinearities and quantify their yielding energy under cyclic  
60 loading.

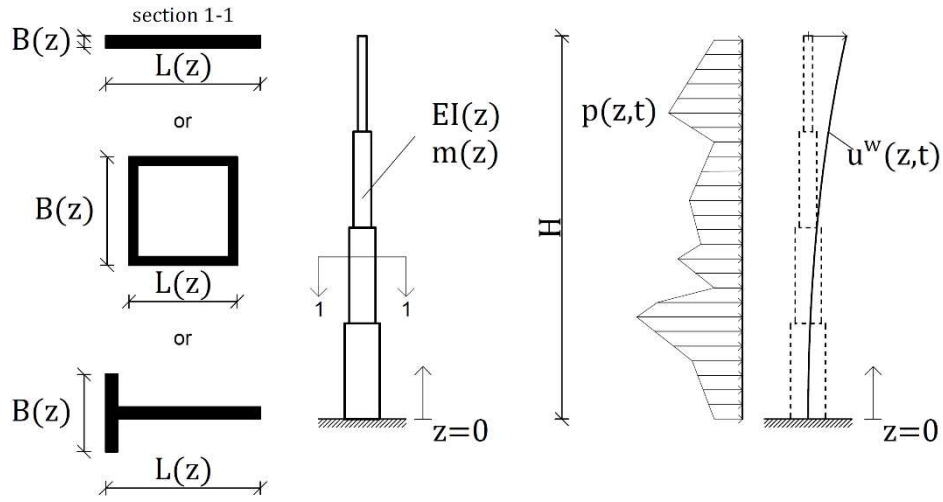
61 Smooth hysteretic models, that stem from the Bouc-Wen equation, have been developed to  
62 provide a continuous change of stiffness or functions that address the bending moment-curvature  
63 relationships (e.g., Sivaselvan and Reinhorn[13]; Wang et al.[14]; Charalampakis and  
64 Koumoussis[15]; Charalampakis[16]). The smooth hysteretic models are utilized to analyze the cyclic  
65 response of a wide variety of mechanical systems such as steel framed-tubes (Lian et al.[17]), shape-  
66 memory-alloy bars (Roh and Reinhorn[18]), wood joints with yielding plates/nails/bolts  
67 (Foliente[19]), bolted joint's dynamic frictional contact (Oldfield et al.[20]), connection-fracture in  
68 low rise steel buildings (Wang and Wen[21]), base-isolation system (Ni et al.[22]), dampers that  
69 interconnect two adjacent structures (Besili and De Angelis[23]) and more. Smooth hysteretic models  
70 have also been incorporated to approximate seismic demands for buildings using cyclic pushover  
71 analysis (Panyakapo[24]) and estimate buildings' collapse seismic fragility curve (Zareian et al.[25];  
72 Xiao et al.[26]). This paper follows suit employs the smooth hysteretic model of Sivaselvan and  
73 Reinhorn[13] for modeling the cyclic behavior mechanical behavior of deteriorating inelastic RC  
74 cantilever elements, which function as the lateral load resisting system of the building.

## 75 2. *Two-dimensional element*

76 The matrix equations model for two-dimensional cantilever element analysis is described in  
77 this section. The section outlines the model assumptions, develops the stiffness matrix related to  
78 lateral DOFs mesh, and ends with examining the model's mesh-size efficiency.

### 79 2.1. *Two-dimensional model assumptions*

80 A general elevation scheme of a slender cantilever element is depicted in Fig. 1. The element  
81 characterized by distributed mass per unit length  $m(z)$ , distributed elasticity  $EI(z)$ , and is subjected  
82 to a distributed lateral load function  $p(z, t)$ . The development process assumes that the element  
83 bends about either the strong/weak axes. Accordingly, the element's cross-section can be one of the  
84 types shown in Fig. 1 or of a different one.



85  
86 **Fig. 1.** Cantilever element of distributed mass and elasticity

87 The partial differential equation (PDE) governing the lateral motion of the undamped system is:

$$\begin{aligned}
 & m(z)\ddot{u}^w(z,t) + f^R(z,t) = p(z,t) \\
 & \text{s. t.} \\
 & 0 \leq z \leq H \\
 & \left. \begin{array}{l}
 \text{i } \mathcal{V}^R(H,t) = 0 \\
 \text{ii } \mathcal{M}^R(H,t) = 0 \\
 \text{iii } u^{w'}(0,t) = 0 \\
 \text{iv } u^w(0,t) = 0
 \end{array} \right\} \text{Boundary Conditions (BC)}
 \end{aligned} \tag{1}$$

89 where  $f^R(z,t)$  is the resisting force at time  $t$  at coordinate  $z$ ,  $u^w(z,t)$  is the lateral displacement at  
90 time  $t$  at coordinate  $z$ , and its second time-derivative  $\ddot{u}^w(z,t)$  is the horizontal acceleration at time  $t$   
91 at coordinate  $z$ , the term  $\mathcal{M}^R(z,t)$  identifies the bending-moment at time  $t$  at coordinate  $z$ , and  
92  $\mathcal{V}^R(z,t)$  the shear-force at time  $t$  at coordinate  $z$ .

93 The Euler-Bernoulli assumption is adopted regarding the lateral movement of the structure.  
94 That means the cross-section movement is constrained to its horizontal plane and its dimensions,  
95  $B(z)$  and  $L(z)$ , remain stationary. Therefore, the angular accelerations and shear deformations are  
96 assumed neglected, which leads to the following relationships:

$$97 \quad \mathcal{V}^R(z,t) = \partial \mathcal{M}^R(z,t) / \partial z \tag{2}$$

$$98 \quad f^R(z,t) = \partial^2 \mathcal{M}^R(z,t) / \partial z^2 \tag{3}$$

99 and the bending relationship:

$$100 \quad \mathcal{M}^R(z,t) = EI(z)\varphi(z,t) \leftrightarrow \varphi(z,t) = u^{w'''}(z,t) \tag{4}$$

101 where  $\varphi(z,t)$  is the bending-curvature. The term of  $f^R(z,t)$  in Eq. (1) is determined by substituting  
102 Eq. (4) into Eq. (3), which yields:

$$103 \quad f^R(z, t) = \partial(EI(z)\varphi(z, t)) / \partial z^2 \quad (5)$$

104 Eqs. (1)-(5) above apply to cantilever shear walls subjected to shear deformations.

105 The analytical solution procedure for Eq. (1) uses the separated variables technique so that  
 106  $u^w(z, t) = \phi(z)q(t)$ . Adhering to the homogeneous boundary conditions (BC) using the shape  
 107 function  $\phi(z)$  leads to superposition of infinite mode shape functions  $\phi_v(z)$  multiplied by their  
 108 respected time governing function  $q_v(t)$ :

$$109 \quad u^w(z, t) = \sum_{v=1}^{\infty} \phi_v(z)q_v(t) \quad (6)$$

110 Substituting Eqs. (5) and (6) into Eq. (1) yields the following formulation:

$$111 \quad \left. \begin{array}{l} m(z) \sum_{v=1}^{\infty} \phi_v(z)\ddot{q}_v(t) + \sum_{v=1}^{\infty} f_v^{R\phi}(z)q_v(t) = p(z, t) \\ s. t. \\ 0 \leq z \leq H \\ f_v^{R\phi}(z) = \partial(EI(z)\phi_v''(z)) / \partial z^2 \\ \left. \begin{array}{l} i \quad EI(H)\phi_v^{(3)}(H) = 0 \\ ii \quad EI(H)\phi_v''(H) = 0 \\ iii \quad \phi_v'(0) = 0 \\ iv \quad \phi_v(0) = 0 \end{array} \right\} B. C. \end{array} \right\} \quad \forall \quad v = 1, \dots, \infty \quad (7)$$

112 where  $f_v^{R\phi}(z)$  is defined herein as the  $v^{\text{th}}$  modal resisting force spatial function.

113 The analytical solution of a cantilever element typically involves defining the shape function  
 114 that solves  $f_v^{R\phi}(z) - \omega_v^2 m(z)\phi_v(z) = 0$  (e.g.,  $\phi_v(z) = C_1 \cos \beta_v z + C_2 \sin \beta_v z + C_3 \cosh \beta_v z +$   
 115  $C_4 \sinh \beta_v z$ ), determining the shape frequencies  $\beta_{v=1,2,\dots,\infty}$  that satisfy the boundary conditions,  
 116 calculating the shape function's coefficients, deriving the modal angular frequencies  $\omega_{v=1,2,\dots,\infty}$ , and  
 117 evaluating  $q_v(t)$ . This section now presents an alternative approach based on matrix structural  
 118 analysis. It offers more simple calculations by approximating the stiffness matrix.

## 119 2.2. Elemental stiffness matrix

120 The cantilever element's stiffness matrix is equivalent to the stiffness distribution operator  
 121  $k(z)$ , which provides the relationship between the  $v^{\text{th}}$  mode shape function  $\phi_v(z)$  and the  $v^{\text{th}}$  modal  
 122 resisting force  $f_v^{R\phi}(z)$ :

$$123 \quad f_v^{R\phi}(z) = k(z)\phi_v(z) \quad \forall \quad v = 1, \dots, \infty \quad (8)$$

124 Accordingly, the stiffness distribution operator is:

$$125 \quad k(z) \equiv \frac{\partial}{\partial z} \frac{\partial}{\partial z} \left( EI(z) \frac{\partial}{\partial z} \frac{\partial}{\partial z} \right) \quad (9)$$

126 Eq. (9) suggests that the stiffness matrix formulation should be comprised of four numerical  
 127 differential transformations. Also, it has to satisfy two fundamental requirements: (i) the matrix has  
 128 to be symmetric so that the modal frequencies are real numbers as suits undamped systems; (ii) the  
 129 matrix must answer the boundary conditions specified in Eq. (7). Nevertheless, the stiffness matrix  
 130 formulation is practically more applicable by implementing numerical integration.

131 Define the flexibility distribution operator  $F(z)$ , which is the inverse of the stiffness  
 132 distribution operator:

$$133 \quad \phi_v(z) = F(z) f_v^{R\phi}(z) \quad \forall \quad v = 1, \dots, \infty \quad (10)$$

134 The operator  $F(z)$  consists of four integral operators in  $z$  such that:

$$135 \quad F(z) \equiv \iint \frac{1}{EI(z)} \iint dz dz dz dz \quad (11)$$

136 The vertical coordinate variable  $z$  is bounded by  $z \in [0 \quad H]$  and, thus, the integration limits of each  
 137 integral operator has to be defined. The integration limits play a crucial role in the stiffness matrix  
 138 development and help obtain a symmetric matrix. More specifically, let us observe the first  
 139 integration operator and examine the two options for integration limits:

$$140 \quad \begin{aligned} \text{option one:} \quad & \int_0^z f_v^{R\phi}(z) dz = EI(z) \phi_v^{(3)}(z) - EI(0) \phi_v^{(3)}(0) \\ \text{option two (preferred):} \quad & \int_H^z f_v^{R\phi}(z) dz = EI(z) \phi_v^{(3)}(z) = \mathcal{V}_v^R(z) \end{aligned} \quad (12)$$

141 Here, option two is preferred because  $EI(H) \phi_v^{(3)}(H) = 0$  and, thus, it gives the distributed modal  
 142 shear force  $\mathcal{V}_v^R(z)$  term only. That concept is repeated in the other three integration operators to  
 143 resolve in:

$$144 \quad \left. \begin{aligned} \int_H^z f_v^{R\phi}(z) dz &= EI(z) \phi_v^{(3)}(z) = \mathcal{V}_v^R(z) && \leftrightarrow EI(H) \phi_v^{(3)}(H) = 0 \\ \int_H^z \int_H^z f_v^{R\phi}(z) dz dz &= EI(z) \phi_v''(z) = \mathcal{M}_v^R(z) && \leftrightarrow EI(H) \phi_v''(H) = 0 \\ \int_0^z \frac{1}{EI(z)} \int_H^z \int_H^z f_v^{R\phi}(z) dz dz dz &= \phi_v'(z) && \leftrightarrow \phi_v'(0) = 0 \\ \int_0^z \int_0^z \frac{1}{EI(z)} \int_H^z \int_H^z f_v^{R\phi}(z) dz dz dz dz &= \phi_v(z) && \leftrightarrow \phi_v(0) = 0 \end{aligned} \right\} \quad \forall \quad v = 1, 2, \dots, \infty \quad (13)$$

145 Accordingly, the flexibility distribution operator  $F(z)$  is:

$$146 \quad \phi_v(z) = F(z) f_v^{R\phi}(z) = \int_0^z \int_0^z \frac{1}{EI(z)} \int_H^z \int_H^z f_v^{R\phi}(z) dz dz dz dz \quad \forall \quad v = 1, 2, \dots, \infty \quad (14)$$

147 Matrix structural analysis is now introduced.

148 Fig. 2 shows the scheme of a discretized vertical cantilever element. The lateral DOFs are  
 149 uniformly distributed with mesh-size  $\Delta z = H/N$  and their index is  $n = 0, 1, 2, \dots, N$ , where  $n = 0$  is the  
 150 ground level and  $n = N$  is the roof level.

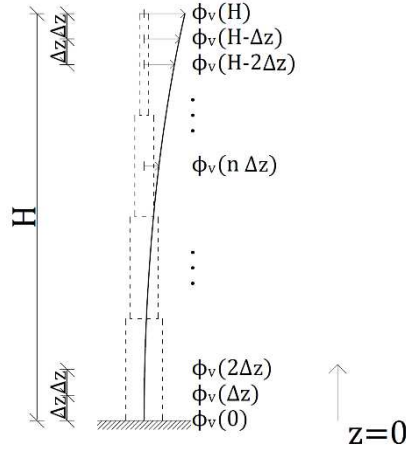


Fig. 2. discretized cantilever element scheme

151  
152

153 Eq. (14) flexibility distribution operator in matrix form is applied as:

$$154 \quad \boldsymbol{\phi}_{\Delta z, v} = \mathbf{F}_{\Delta z} \mathbf{f}_{\Delta z, v}^{\text{R}\phi} \quad \forall \quad v = 1, 2, \dots, \infty \quad (15)$$

155 where  $\mathbf{F}_{\Delta z}$  is the symmetric flexibility transformation matrix,  $\boldsymbol{\phi}_{\Delta z, v}$  is the  $v^{\text{th}}$  mode shape vector and  
156 is the approximation of  $\phi_v(z)$  at the DOFs:

$$157 \quad \boldsymbol{\phi}_{\Delta z, v} \cong [\phi_v(0) \cdots \phi_v(n \Delta z) \cdots \phi_v(N \Delta z)]^T \quad (16)$$

158 and  $\mathbf{f}_{\Delta z, v}^{\text{R}\phi}$  is the  $v^{\text{th}}$  modal resisting force vector and the approximation of  $f_v^{\text{R}\phi}(z)$  at the DOFs:

$$159 \quad \mathbf{f}_{\Delta z, v}^{\text{R}\phi} = [f_v^{\text{R}\phi}(0) \cdots f_v^{\text{R}\phi}(n \Delta z) \cdots f_v^{\text{R}\phi}(N \Delta z)]^T \quad (17)$$

160 It is noted that the matrix/vector terms that follow in this paper are notated with lower case  $\Delta z$  to  
161 signify their dependency on the discretized cantilever element's mesh-size.

162 The symmetric flexibility transformation matrix  $\mathbf{F}_{\Delta z}$  is calculated using the following matrix  
163 expression:

$$164 \quad \mathbf{F}_{\Delta z} = \mathbf{T}_{z \in [0 \rightarrow z]}^{\int dz} \mathbf{T}_{z \in [0 \rightarrow z]}^{\int dz} (\mathbf{EI}_{\Delta z})^{-1} \mathbf{T}_{z \in [H \rightarrow z]}^{\int dz} \mathbf{T}_{z \in [H \rightarrow z]}^{\int dz} \quad (18)$$

165 where  $\mathbf{T}_{z \in [H \rightarrow z]}^{\int dz}$  denotes integration transformation matrix in  $z \in [H \rightarrow z]$ ,  $\mathbf{T}_{z \in [0 \rightarrow z]}^{\int dz}$  denotes  
166 integration transformation matrix in  $z \in [0 \rightarrow z]$ , and  $\mathbf{EI}_{\Delta z}$  is the elasticity matrix so that:

$$167 \quad \mathbf{EI}_{\Delta z} = \Delta z \text{diag}\{EI(0) \cdots EI(n \Delta z) \cdots EI(N \Delta z)\} \quad (19)$$

168 The Left Riemann Sums (LRS) numerical integration method is employed for defining

$$169 \quad \mathbf{T}_{z \in [H \rightarrow z]}^{\int dz} \text{ and } \mathbf{T}_{z \in [0 \rightarrow z]}^{\int dz} \text{ so that:}$$

$$170 \quad \mathbf{T}_{z \in [0 \rightarrow z]}^{f dz} = \Delta z \begin{bmatrix} 0 & 0 & 0 & \cdots & 0 & 0 & 0 \\ 1 & 0 & 0 & \cdots & 0 & 0 & 0 \\ 1 & 1 & 0 & \cdots & 0 & 0 & 0 \\ \vdots & \vdots & \vdots & \ddots & \vdots & \vdots & \vdots \\ 1 & 1 & 1 & \cdots & 0 & 0 & 0 \\ 1 & 1 & 1 & \cdots & 1 & 0 & 0 \\ 1 & 1 & 1 & \cdots & 1 & 1 & 0 \end{bmatrix}_{N+1 \times N+1} \cong \int_0^z dz \quad (20a)$$

$$171 \quad \mathbf{T}_{z \in [H \rightarrow z]}^{f dz} = -\Delta z \begin{bmatrix} 0 & 1 & 1 & \cdots & 1 & 1 & 1 \\ 0 & 0 & 1 & \cdots & 1 & 1 & 1 \\ 0 & 0 & 0 & \cdots & 1 & 1 & 1 \\ \vdots & \vdots & \vdots & \ddots & \vdots & \vdots & \vdots \\ 0 & 0 & 0 & \cdots & 0 & 1 & 1 \\ 0 & 0 & 0 & \cdots & 0 & 0 & 1 \\ 0 & 0 & 0 & \cdots & 0 & 0 & 0 \end{bmatrix}_{N+1 \times N+1} \cong -\int_H^z dz \quad (20b)$$

172 The LRS method is unique since it provides symmetric  $\mathbf{F}_{\Delta z}$  of the general form:

$$173 \quad \mathbf{F}_{\Delta z} = \begin{bmatrix} \mathbf{0}_{2 \times 2} & \mathbf{0}_{2 \times N-1} \\ \mathbf{0}_{N-1 \times 2} & \mathcal{F}_{\Delta z} \end{bmatrix} \quad (21)$$

174 where  $\mathcal{F}_{\Delta z}$  is referred to herein as the  $N-1 \times N-1$  flexibility sub-matrix, and  $\mathbf{0}$  is a matrix of zeros.

175 The inverse form of  $\mathbf{F}_{\Delta z}$  gives the stiffness matrix  $\mathbf{k}_{\Delta z}$ , but  $(\mathbf{F}_{\Delta z})^{-1}$  is singular due to the zeros  
 176 on its diagonal, and static condensation cannot be applied because of  $\mathbf{0}_{2 \times N-1}$  and  $\mathbf{0}_{N-1 \times 2}$ .  
 177 Therefore, the following stiffness matrix and the equivalent to the inverse form of  $\mathbf{F}_{\Delta z}$  is proposed:

$$178 \quad \mathbf{k}_{\Delta z} = \begin{bmatrix} \mathbf{\Lambda} & \mathbf{0}_{2 \times N-1} \\ \mathbf{0}_{N-1 \times 2} & (\mathcal{F}_{\Delta z})^{-1} \end{bmatrix} \leftrightarrow \mathbf{\Lambda} = \begin{bmatrix} \Lambda_1 & 0 \\ 0 & \Lambda_2 \end{bmatrix} \equiv \begin{bmatrix} \infty & 0 \\ 0 & \infty \end{bmatrix} \quad (22)$$

179 where the proposed  $\mathbf{k}_{\Delta z}$  is composed of the invertible part of the flexibility matrix  $(\mathcal{F}_{\Delta z})^{-1}$  and  $\mathbf{\Lambda}$  is  
 180 a  $2 \times 2$  diagonal matrix whose components are large-valued numbers that resemble inverse flexibility  
 181 matrix singularity. It is noted that  $\mathbf{\Lambda}$  does not interfere with the structural analysis. The large-valued  
 182 numbers of  $\mathbf{\Lambda}$  assign large modal frequencies to its' two corresponding modal systems of mode  
 183 shapes  $[1 \ 0 \ 0 \ \cdots \ 0]^T$  and  $[0 \ 1 \ 0 \ \cdots \ 0]^T$  – making these modes irrelevant as they should.  
 184 In this paper's continuation, when the inelastic cantilever element is concerned, the structure is  
 185 analyzed in bending coordinates, and, thus, a different approach is proposed.

186 The cantilever element's dynamic equilibrium presented by Eq. (7) is represented as a matrix  
 187 equations model by using Eqs. (15)-(22):

$$\begin{aligned}
& \mathbf{m}_{\Delta z} \Phi_{\Delta z} \ddot{\mathbf{q}}_{\Delta z}(t) + \mathbf{f}_{\Delta z}^{\text{R}\phi} \mathbf{q}_{\Delta z}(t) = \mathbf{p}_{\Delta z}(t) \\
& \text{s. t.} \\
& n = 1, \dots, N + 1 \quad ; \quad N + 1 = H/\Delta z + 1 \\
& \mathbf{f}_{\Delta z, v}^{\text{R}\phi} = \mathbf{k}_{\Delta z} \Phi_{\Delta z, v} \\
& \left. \begin{aligned}
& \text{i} \quad \left[ \mathbf{T}_{z \in [H \rightarrow 0]}^{\int dz} \Delta z \mathbf{f}_{\Delta z, v}^{\text{R}\phi} \right]_{N+1} = (\mathcal{V}_{\Delta z, v}^{\text{R}})_{N+1} = EI(H) \phi_{\Delta z, v, N+1}^{(3)} = 0 \\
& \text{ii} \quad \left[ \mathbf{T}_{z \in [H \rightarrow 0]}^{\int dz} \Phi_{\Delta z, v}^{(3)} \right]_{N+1} = (\mathcal{M}_{\Delta z, v}^{\text{R}})_{N+1} = EI(H) \phi_{\Delta z, v, N+1}'' = 0 \\
& \text{iii} \quad \phi'_{\Delta z, v_1} = \left[ \mathbf{T}_{z \in [0 \rightarrow H]}^{\int dz} \Phi_{\Delta z, v}'' \right]_1 = 0 \\
& \text{iv} \quad \phi_{\Delta z, v_1} = \left[ \mathbf{T}_{z \in [0 \rightarrow H]}^{\int dz} \Phi_{\Delta z, v}' \right]_1 = 0
\end{aligned} \right\} \text{BC.} \quad \forall \quad v = 1, 2, \dots, \infty
\end{aligned} \tag{23}$$

189 In Eq. (23),  $\mathbf{m}_{\Delta z}$  is the mass matrix of the cantilever element, and  $\mathbf{p}_{\Delta z}(t)$  is the lateral load vector,  
190 which are given by:

$$191 \quad \mathbf{m}_{\Delta z} = \Delta z \text{diag} \left\{ \frac{m(0)}{2} \quad m(\Delta z) \quad \dots \quad m(n \Delta z) \quad \dots \quad m((N-1) \Delta z) \quad \frac{m(N \Delta z)}{2} \right\} \tag{24}$$

$$192 \quad \mathbf{p}_{\Delta z}(t) \cong \Delta z [p(0, t) \dots p(n \Delta z, t) \dots p(N \Delta z, t)]^T \tag{25}$$

193 Also,  $\Phi_{\Delta z}$ ,  $\mathbf{f}_{\Delta z}^{\text{R}\phi}$ , and  $\mathbf{q}_{\Delta z}(t)$  are matrix terms composed of the modal parameters  $\phi_{\Delta z, v}$ ,  $\mathbf{f}_{\Delta z, v}^{\text{R}\phi}$ , and  $q_v(t)$ ,  
194 respectively, as follows:

$$195 \quad \Phi_{\Delta z} = [\phi_{\Delta z, 1} \dots \phi_{\Delta z, v} \dots \phi_{\Delta z, N+1}] \leftrightarrow \Phi_{\Delta z, v} \cong [\phi_v(0) \dots \phi_v(n \Delta z) \dots \phi_v(N \Delta z)]^T \tag{26}$$

$$196 \quad \mathbf{f}_{\Delta z}^{\text{R}\phi} = [\mathbf{f}_{\Delta z, 1}^{\text{R}\phi} \dots \mathbf{f}_{\Delta z, v}^{\text{R}\phi} \dots \mathbf{f}_{\Delta z, N+1}^{\text{R}\phi}] \leftrightarrow \mathbf{f}_{\Delta z, v}^{\text{R}\phi} = [f_v^{\text{R}\phi}(0) \dots f_v^{\text{R}\phi}(n \Delta z) \dots f_v^{\text{R}\phi}(N \Delta z)]^T \tag{27}$$

$$197 \quad \mathbf{q}_{\Delta z}(t) \cong [q_1(t) \dots q_v(t) \dots \phi_{N+1}(t)]^T \tag{28}$$

198 The developed mass and stiffness matrices of the cantilever element,  $\mathbf{m}_{\Delta z}$  and  $\mathbf{k}_{\Delta z}$  replace the  
199 Eq. (7) analytical solution with idealized linear matrix algebra for performing dynamic structural  
200 analysis. The matrix equations model's approximation level is now examined.

### 201 2.3. Mesh-size efficiency

202 The following sub-section exemplifies the linear relation between the mesh-size and the  
203 precision of the matrix equations model based on the LRS method. The mesh-size efficiency  
204 examines the error in modal parameters for a cantilever element of uniform mass per unit length  
205  $m(z) = m$  and uniform elasticity  $EI(z) = EI$ . The PDE governing undamped free vibrations is  
206 formulated as:

$$\begin{aligned}
& m(z)\ddot{u}^w(z, t) + f^R(z, t) = 0 \\
& \text{s. t.} \\
& 0 \leq z \leq H \\
& f^R(z, t) = \partial(EI(z)\varphi(z, t))/\partial z^2 \\
207 \quad & \left. \begin{aligned} & i \quad u^w(0, t) = 0 \\ & ii \quad u^{w'}(0, t) = 0 \\ & iii \quad \mathcal{M}^R(H, t) = 0 \\ & iv \quad \mathcal{V}(H, t) = 0 \end{aligned} \right\} B.C. \tag{29}
\end{aligned}$$

208 The analytical solution yields in the terms for  $\omega_v$  and  $\phi_v(z)$ :

$$209 \quad \omega_v = \frac{(\varepsilon_v H)^2}{H^2} \sqrt{\frac{EI}{m}} \quad \forall \quad v = 1, 2, \dots, \infty \tag{30}$$

$$210 \quad \phi_v(z) = C_v \left[ \cosh(\varepsilon_v z) + \cos(\varepsilon_v z) + \frac{\cosh(\varepsilon_v H) - \cos(\varepsilon_v H)}{\sinh(\varepsilon_v H) - \sin(\varepsilon_v H)} (\sinh(\varepsilon_v z) - \sin(\varepsilon_v z)) \right] \tag{31}$$

211 where  $C_v$  is an arbitrary coefficient, and the quantity of  $\varepsilon_v H$  stems from:

$$212 \quad 1 + \cos(\varepsilon_v H) \cosh(\varepsilon_v H) = 0 \quad \leftrightarrow \quad 0 < \varepsilon_1 H < \varepsilon_2 H < \dots < \varepsilon_v H < \dots \tag{32}$$

213 The coefficient  $C_v$  is taken so that the Euclidean norm of a vector composed of  $\phi_v(z)$  values in  $z =$   
214  $0, \Delta z, \dots, H$  equals 1.0. The modal frequencies and mode shapes of the matrix equations model are  
215 simply the eigenvalues (in square root) and eigenvectors of the system matrices  $\mathbf{m}_{\Delta z}$  and  $\mathbf{k}_{\Delta z}$ :

$$216 \quad \det|\mathbf{m}_{\Delta z}^{-1} \mathbf{k}_{\Delta z} - \omega_{\Delta z, v}^2 \mathbf{I}| = 0 \quad \leftrightarrow \quad \omega_{\Delta z, 1} < \omega_{\Delta z, 2} < \dots \tag{33}$$

$$217 \quad (\mathbf{m}_{\Delta z}^{-1} \mathbf{k}_{\Delta z} - \omega_{\Delta z, v}^2 \mathbf{I}) \boldsymbol{\phi}_{\Delta z, v} = \mathbf{0} \quad \leftrightarrow \quad \|\boldsymbol{\phi}_{\Delta z, v}\|_2 = 1.0 \quad \forall \quad v = 1, 2, \dots, \infty \tag{34}$$

218 where  $\mathbf{I}$  is the  $N+1 \times N+1$  identity matrix. For the desired  $\Delta z$ , the mass and stiffness matrices are  
219 calculated as:

$$220 \quad \mathbf{m}_{\Delta z} = \Delta z \operatorname{diag} \left\{ \frac{m}{2} \quad m \quad \dots \quad m \quad \dots \quad m \quad \frac{m}{2} \right\}_{N+1}$$

$$221 \quad \mathbf{k}_{\Delta z, \ell} = \begin{bmatrix} \boldsymbol{\Lambda} & \mathbf{0} \\ \mathbf{0} & (\mathcal{F}_{\Delta z})^{-1} \end{bmatrix}$$

222 where:

$$223 \quad \boldsymbol{\Lambda} = \begin{bmatrix} \Lambda_1 & 0 \\ 0 & \Lambda_2 \end{bmatrix} = \begin{bmatrix} 10^{20} & 0 \\ 0 & 10^{20} \end{bmatrix}$$

$$224 \quad \mathbf{F}_{\Delta z} = \mathbf{T}_{z \in [0 \rightarrow z]}^{\int dz} \mathbf{T}_{z \in [0 \rightarrow z]}^{\int dz} (\Delta z EI \mathbf{I})^{-1} \mathbf{T}_{z \in [H \rightarrow z]}^{\int dz} \mathbf{T}_{z \in [H \rightarrow z]}^{\int dz} = \begin{bmatrix} \mathbf{0} & \mathbf{0} \\ \mathbf{0} & \mathcal{F}_{\Delta z} \end{bmatrix} \rightarrow \mathcal{F}_{\Delta z}$$

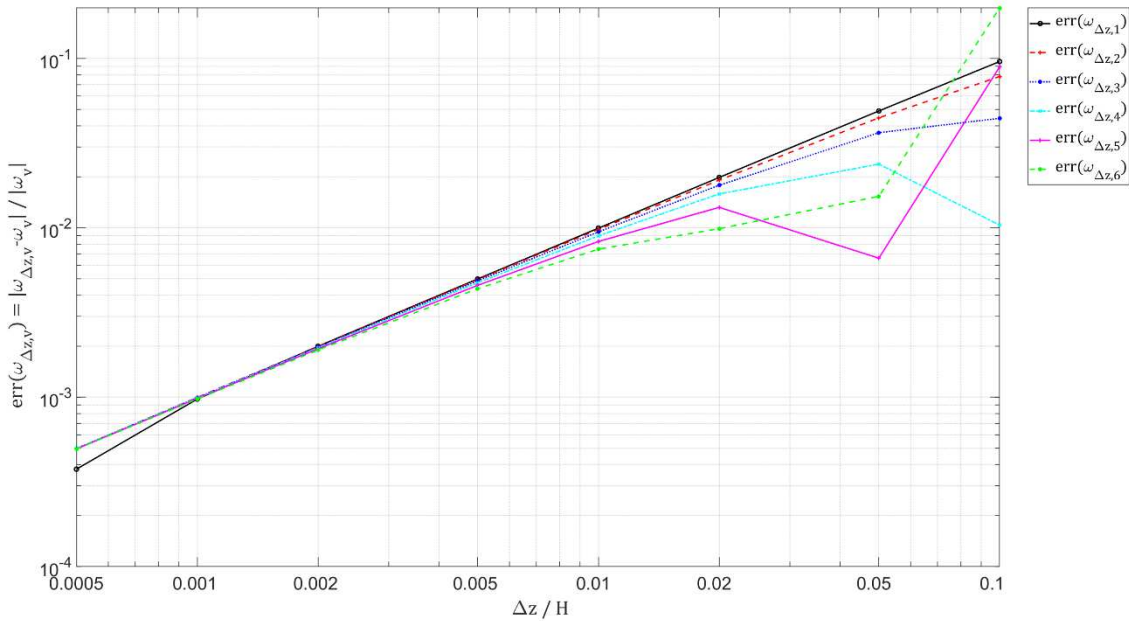
225 and the forms of  $\mathbf{T}_{z \in [0 \rightarrow z]}^{\int dz}$  and  $\mathbf{T}_{z \in [H \rightarrow z]}^{\int dz}$  are provided in Eq. (20).

226 The relative error between the analytical solution and the matrix equations model is given  
227 by:

$$228 \quad \text{err}(\omega_{\Delta z,v}) = \frac{|\omega_{\Delta z,v} - \omega_v|}{|\omega_v|} \quad (35)$$

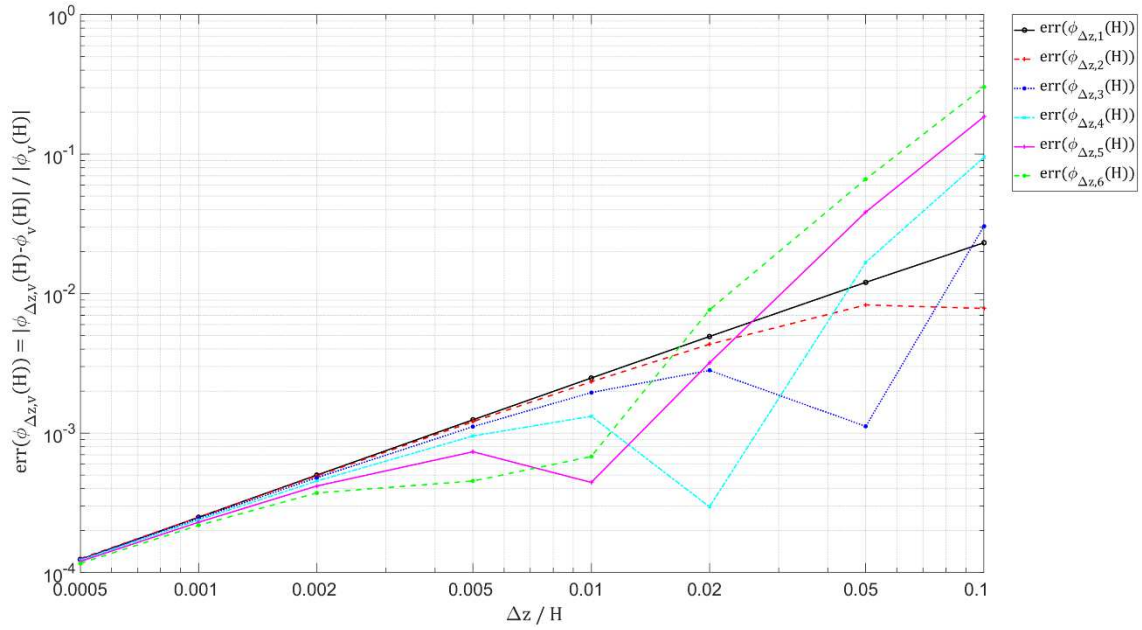
$$229 \quad \text{err}(\phi_{\Delta z,v}(H)) = \frac{|\phi_{\Delta z,v}(H) - \phi_v(H)|}{|\phi_v(H)|} \leftrightarrow \left\| \begin{array}{c} \phi_v(0) \\ \phi_v(\Delta z) \\ \vdots \\ \phi_v(H) \end{array} \right\|_2 = 1.0 \quad (36)$$

230 where  $\phi_v(H)$  and  $\phi_{\Delta z,v}(H)$  are the modal roof displacement and the approximated modal roof  
 231 displacements, respectively. The examination observes the first six modal systems and employs  
 232 eight mesh-size cases of  $\Delta z = \{H/2,000, H/1,000, H/500, H/200, H/100, H/50, H/20, H/10\}$  so that  
 233 the corresponding number of lateral DOFs is  $N + 1 = \{2,001, 1,001, 501, 201, 101, 51, 21, 11\}$ . The  
 234 functions of  $\text{err}(\omega_{\Delta z,v})$  and  $\text{err}(\phi_{\Delta z,v}(H))$  versus  $\Delta z/H$  are depicted in Fig. 3 and Fig. 4, respectively.  
 235 Fig. 3 shows that for  $\Delta z/H < 0.01$  the value of  $\text{err}(\omega_{\Delta z,v})$  decreases linearly with  $\Delta z/H$  with  
 236 approximately similar error level for all modes. Fig. 4 shows almost the same for  $\text{err}(\phi_{\Delta z,v}(H))$  but  
 237 when  $\Delta z/H < 0.002$ . Overall, it is shown that the matrix equations model can provide very small  
 238 errors. The optimal choice for mesh-size should minimize its quantity as much as possible while  
 239 considering the work station's computational capabilities.



240  
241

**Fig. 3.** The relative error of the modal angular frequency approximation

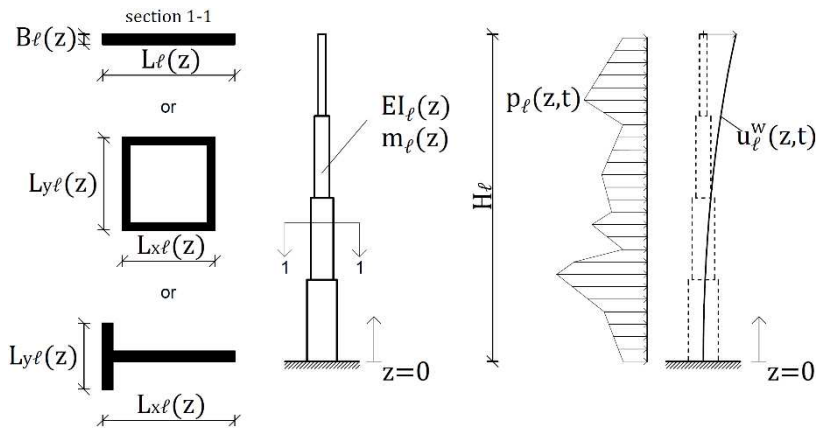


242  
243

**Fig. 4.** The relative error of the modal roof displacement approximation

244 3. *Three-dimensional structure*

245 The cantilever element's mass and stiffness matrices are used for developing the matrix  
 246 equations model of three-dimensional structures. The element is considered a part of the lateral load  
 247 resisting system and is notated henceforth as the  $\ell^{\text{th}}$  element (within the three-dimensional  
 248 structure). Fig. 5 shows the cantilever element scheme with the new parametric notations, and Fig.  
 249 6 illustrates the three-dimensional structure. In Fig. 6,  $r$  is the ceilings' index so that  $r = 1, \dots, R$ . Also,  
 250  $\mathcal{H}_r$  denotes the height of the  $r^{\text{th}}$  ceiling above ground level and  $\mathcal{H}_R$  is the roof level. For mesh-size  
 251  $\Delta z = \mathcal{H}_R/N$  the DOFs' index is  $n = 0, 1, \dots, N$ . A cantilever element can have less than  $N$ -DOFs when  
 252 its' height is  $H_\ell < \mathcal{H}_R$ , and that element is of  $N_\ell = H_\ell/\Delta z$  DOFs number – see Fig. 7.



253  
254

**Fig. 5.** The  $\ell^{\text{th}}$  element of distributed mass and elasticity

255  
256

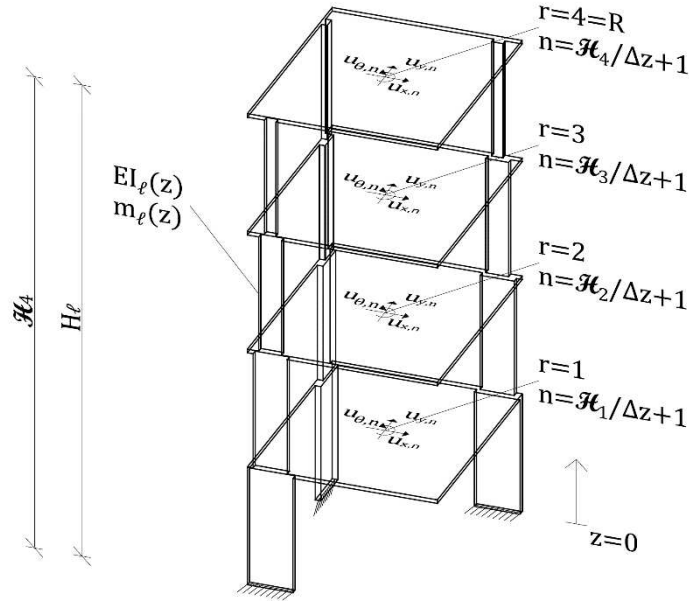


Fig. 6. Three-dimensional structure with cantilever elements illustration

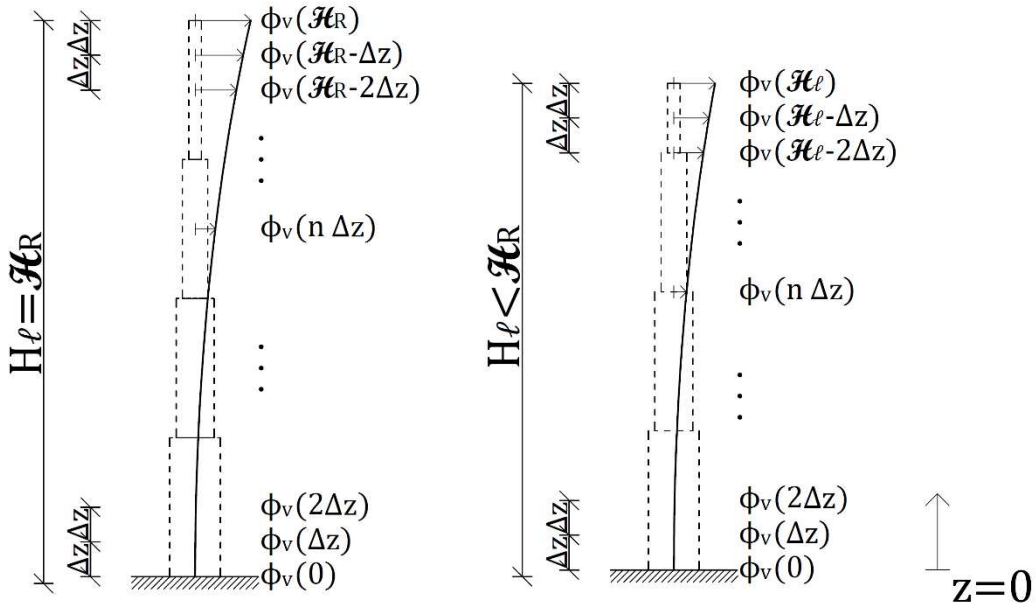


Fig. 7. Element's DOFs for  $H_\ell = \mathcal{H}_R$  (left) and  $H_\ell < \mathcal{H}_R$  (right)

257  
258

259 The three-dimensional model is associated with the Euler-Bernoulli assumption (as the two-  
260 dimensional cantilever model in section 2). Accordingly, the ceilings are considered rigid  
261 diaphragms of zero mutuality between their movement in the  $x$ -direction and  $y$ -direction, with no  
262 movement in the  $z$ -direction. It should be noted that the proposed modelling does not catch the  
263 torsional behavior of cantilever structures and does not fit to cross sections without axial symmetry.

264 The  $\ell^{\text{th}}$  cantilever element's mass matrix  $\mathbf{m}_{\Delta z, \ell}$  and stiffness matrix  $\mathbf{k}_{\Delta z, \ell}$  are determined  
265 according to the element's  $N_\ell + 1$  DOFs (which can be less than the global  $N + 1$  DOFs number):

$$\begin{aligned}
& \mathbf{m}_{\Delta z, \ell} = \Delta z \operatorname{diag} \left\{ \frac{m_\ell(0)}{2} \quad m_\ell(\Delta z) \quad \cdots \quad m_\ell(n \Delta z) \quad \cdots \quad m_\ell(N_\ell - \Delta z) \quad \frac{m_\ell(N_\ell \Delta z)}{2} \right\} \\
& \mathbf{k}_{\Delta z, \ell} = \begin{bmatrix} \Lambda & \mathbf{0} \\ \mathbf{0} & (\mathcal{F}_{\Delta z, \ell})^{-1} \end{bmatrix} \\
& \mathbf{F}_{\Delta z, \ell} = \mathbf{T}_{z \in [0 \rightarrow z]}^{\int dz} \mathbf{T}_{z \in [0 \rightarrow z]}^{\int dz} (\mathbf{EI}_{\Delta z, \ell})^{-1} \mathbf{T}_{z \in [H_\ell \rightarrow z]}^{\int dz} \mathbf{T}_{z \in [H_\ell \rightarrow z]}^{\int dz} = \cdots \\
& \quad \begin{bmatrix} \mathbf{0} & \mathbf{0} \\ \mathbf{0} & \mathcal{F}_{\Delta z, \ell} \end{bmatrix} \\
& \mathbf{EI}_{\Delta z, \ell} = \Delta z \operatorname{diag} \{ EI_\ell(0) \quad EI_\ell(\Delta z) \quad \cdots \quad EI_\ell(n \Delta z) \quad \cdots \quad EI_\ell(N_\ell \Delta z) \} \\
& \mathbf{T}_{z \in [0 \rightarrow z]}^{\int dz} = \Delta z \begin{bmatrix} 0 & 0 & 0 & \cdots & 0 & 0 & 0 \\ 1 & 0 & 0 & \cdots & 0 & 0 & 0 \\ 1 & 1 & 0 & \cdots & 0 & 0 & 0 \\ \vdots & \vdots & \vdots & \ddots & \vdots & \vdots & \vdots \\ 1 & 1 & 1 & \cdots & 0 & 0 & 0 \\ 1 & 1 & 1 & \cdots & 1 & 0 & 0 \\ 1 & 1 & 1 & \cdots & 1 & 1 & 0 \end{bmatrix}_{N_\ell+1 \times N_\ell+1} \cong \int_0^z dz \\
& \mathbf{T}_{z \in [H_\ell \rightarrow z]}^{\int dz} = -\Delta z \begin{bmatrix} 0 & 1 & 1 & \cdots & 1 & 1 & 1 \\ 0 & 0 & 1 & \cdots & 1 & 1 & 1 \\ 0 & 0 & 0 & \cdots & 1 & 1 & 1 \\ \vdots & \vdots & \vdots & \ddots & \vdots & \vdots & \vdots \\ 0 & 0 & 0 & \cdots & 0 & 1 & 1 \\ 0 & 0 & 0 & \cdots & 0 & 0 & 1 \\ 0 & 0 & 0 & \cdots & 0 & 0 & 0 \end{bmatrix}_{N_\ell+1 \times N_\ell+1} \cong -\int_{H_\ell}^z dz \\
& N_\ell = H_\ell / \Delta z
\end{aligned} \quad \left. \vphantom{\begin{aligned} \mathbf{m}_{\Delta z, \ell} \\ \mathbf{k}_{\Delta z, \ell} \\ \mathbf{F}_{\Delta z, \ell} \\ \mathbf{EI}_{\Delta z, \ell} \\ \mathbf{T}_{z \in [0 \rightarrow z]}^{\int dz} \\ \mathbf{T}_{z \in [H_\ell \rightarrow z]}^{\int dz} \end{aligned}} \right\} \forall \ell = 1, 2, \dots \quad (37)$$

267 The equation-of-damped-motion of the three-dimensional structure, subjected to lateral and  
268 torsional loading, is formulated as:

$$269 \quad \tilde{\mathbf{m}}_{\Delta z} \ddot{\tilde{\mathbf{u}}}_{\Delta z}(t) + \tilde{\mathbf{c}}_{\Delta z} \dot{\tilde{\mathbf{u}}}_{\Delta z}(t) + \tilde{\mathbf{k}}_{\Delta z} \tilde{\mathbf{u}}_{\Delta z}(t) = \tilde{\mathbf{p}}_{\Delta z}(t) \quad (38)$$

270 where the matrices  $\tilde{\mathbf{m}}_{\Delta z}$ ,  $\tilde{\mathbf{c}}_{\Delta z}$ , and  $\tilde{\mathbf{k}}_{\Delta z}$  are the global mass matrix, global inherent damping matrix,  
271 and global stiffness matrix, respectively. The  $3N+3$ -dimensional global displacement vector  $\tilde{\mathbf{u}}_{\Delta z}(t)$  is  
272 composed of three  $N+1$ -dimensional sub-vectors  $\tilde{\mathbf{u}}_{\Delta z, x}(t)$ ,  $\tilde{\mathbf{u}}_{\Delta z, y}(t)$ , and  $\tilde{\mathbf{u}}_{\Delta z, \theta}(t)$  of the form:

$$273 \quad \tilde{\mathbf{u}}_{\Delta z}(t) = \begin{Bmatrix} \tilde{\mathbf{u}}_{\Delta z, x}(t) \\ \tilde{\mathbf{u}}_{\Delta z, y}(t) \\ \tilde{\mathbf{u}}_{\Delta z, \theta}(t) \end{Bmatrix}; \quad \tilde{\mathbf{u}}_{\Delta z, x}(t) = \begin{Bmatrix} \tilde{u}_{x,1}(t) \\ \vdots \\ \tilde{u}_{x,n}(t) \\ \vdots \\ \tilde{u}_{x,N+1}(t) \end{Bmatrix}; \quad \tilde{\mathbf{u}}_{\Delta z, y}(t) = \begin{Bmatrix} \tilde{u}_{y,1}(t) \\ \vdots \\ \tilde{u}_{y,n}(t) \\ \vdots \\ \tilde{u}_{y,N+1}(t) \end{Bmatrix}; \quad \tilde{\mathbf{u}}_{\Delta z, \theta}(t) = \begin{Bmatrix} \tilde{u}_{\theta,1}(t) \\ \vdots \\ \tilde{u}_{\theta,n}(t) \\ \vdots \\ \tilde{u}_{\theta,N+1}(t) \end{Bmatrix} \quad (39)$$

274 The DOFs  $\tilde{u}_{x,n}(t)$  and  $\tilde{u}_{y,n}(t)$  denote lateral deformations at the  $z = n\Delta z$  level in the  $x$ -direction and  
275  $y$ -direction, respectively, and  $\tilde{u}_{\theta,n}(t)$  is the rotation about the DOFs origin. The developed model  
276 allows the global DOFs to be located anywhere within the RC ceiling slabs' boundaries and not  
277 necessarily at the ceiling center-of-mass (CM). The  $3N+3$ -dimensional load vector  $\tilde{\mathbf{p}}_{\Delta z}(t)$  is composed  
278 of three  $N+1$ -dimensional sub-vectors  $\tilde{\mathbf{p}}_{\Delta z, x}(t)$ ,  $\tilde{\mathbf{p}}_{\Delta z, y}(t)$ , and  $\tilde{\mathbf{p}}_{\Delta z, \theta}(t)$  applied in the directions of  
279  $\tilde{\mathbf{u}}_{\Delta z, x}(t)$ ,  $\tilde{\mathbf{u}}_{\Delta z, y}(t)$ , and  $\tilde{\mathbf{u}}_{\Delta z, \theta}(t)$ , respectively:

$$280 \quad \tilde{\mathbf{p}}_{\Delta z}(t) = \begin{pmatrix} \tilde{\mathbf{p}}_{\Delta z,x}(t) \\ \tilde{\mathbf{p}}_{\Delta z,y}(t) \\ \tilde{\mathbf{p}}_{\Delta z,\theta}(t) \end{pmatrix} \quad (40)$$

281 The global mass matrix of the three-dimensional structure is of the diagonal form:

$$282 \quad \tilde{\mathbf{m}}_{\Delta z} = \begin{bmatrix} \mathbf{m}_{\Delta z}^* & & \\ & \mathbf{m}_{\Delta z}^* & \\ & & \mathbf{I}_{\Delta z}^{m*} \end{bmatrix} \quad (41)$$

283 where  $\mathbf{m}_{\Delta z}^*$  is the  $N+1 \times N+1$  diagonal mass matrix of the structure, and  $\mathbf{I}_{\Delta z}^{m*}$  is the  $N+1 \times N+1$  diagonal  
 284 moment-of-inertia matrix. The  $n^{\text{th}}$  diagonal component of  $\mathbf{m}_{\Delta z}^*$  and  $\mathbf{I}_{\Delta z}^{m*}$  refers to the  $z = n \Delta z$  level.  
 285 The global mass matrix  $\tilde{\mathbf{m}}_{\Delta z}$  is formed using transformation matrices  $\mathbf{a}_{m1,\ell}$  for the respected  $\ell^{\text{th}}$   
 286 element and  $\mathbf{a}_{m2,r}$  for the  $r^{\text{th}}$  ceiling, so that:

$$287 \quad \tilde{\mathbf{m}}_{\Delta z} = \sum_{\ell} \mathbf{a}_{m1,\ell} \begin{bmatrix} \mathbf{m}_{\Delta z,\ell} & \mathbf{0}_{N_{\ell} \times N - N_{\ell}} \\ \mathbf{0}_{N - N_{\ell} \times N_{\ell}} & \mathbf{0}_{N - N_{\ell} \times N - N_{\ell}} \end{bmatrix} \mathbf{a}_{m1,\ell}^T + \sum_{r=1}^R \mathbf{a}_{m2,r} m_r \mathbf{a}_{m2,r}^T \quad (42)$$

288 where:

$$289 \quad \mathbf{a}_{m1,\ell} = \begin{bmatrix} \mathbf{I} & \mathbf{0} & \mathbf{0} \\ \mathbf{0} & \mathbf{I} & \mathbf{0} \\ \mathbf{0} & \mathbf{0} & \mathbf{ROI}_{\Delta z,\ell} \mathbf{ROI}_{\Delta z,\ell} \end{bmatrix} \quad (43)$$

$$290 \quad \mathbf{a}_{m2,r} = \begin{bmatrix} \mathbf{e}_r & \tilde{\mathbf{0}} & \tilde{\mathbf{0}} \\ \tilde{\mathbf{0}} & \mathbf{e}_r & \tilde{\mathbf{0}} \\ \tilde{\mathbf{0}} & \tilde{\mathbf{0}} & \mathbf{ROI}_r^2 \mathbf{e}_r \end{bmatrix} \quad (44)$$

291 In Eq. (42), the zeros matrices ( $\mathbf{0}_{N_{\ell} \times N - N_{\ell}}$ ,  $\mathbf{0}_{N - N_{\ell} \times N_{\ell}}$ , and  $\mathbf{0}_{N - N_{\ell} \times N - N_{\ell}}$ ) treat the case of  $H_{\ell} < \mathcal{H}_R$ ,  $m_r$  is  
 292 the  $r^{\text{th}}$  ceiling mass,  $\mathbf{a}_{m1,\ell}$  is a  $3N+3 \times 3N+3$  transformation matrix defined according to Eq. (43), and  
 293  $\mathbf{a}_{m2,\ell}$  is a  $3N+3 \times 3$  transformation matrix defined according to Eq. (44). Furthermore, in Eq. (43),  $\mathbf{0}$  is  
 294 a  $N+1 \times N+1$  matrix of zeros,  $\mathbf{ROI}_{\Delta z,\ell}$  is a diagonal matrix whose components are the  $\ell^{\text{th}}$  element's  
 295 radius-of-inertia matrix:

$$296 \quad \mathbf{ROI}_{\Delta z,\ell} = \text{diag}\{\mathbf{ROI}_{\ell,0}, \dots, \mathbf{ROI}_{\ell,n}, \dots, \mathbf{ROI}_{\ell,N}\} \quad (45)$$

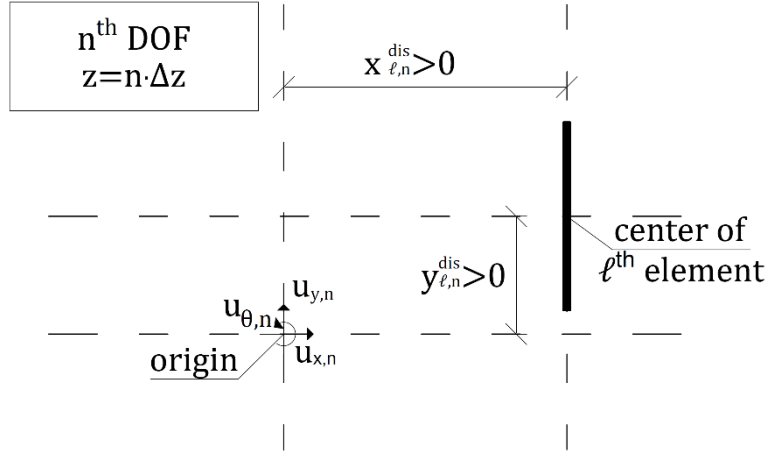
297 so that:

$$298 \quad \mathbf{ROI}_{\ell,n} = \left( \frac{B(n \Delta z)^2 + L(n \Delta z)^2}{12} + x_{\ell,n}^{\text{dis}^2} + y_{\ell,n}^{\text{dis}^2} \right)^{0.5} \quad \forall \quad n = 0, 1, \dots, N_{\ell} \quad (46)$$

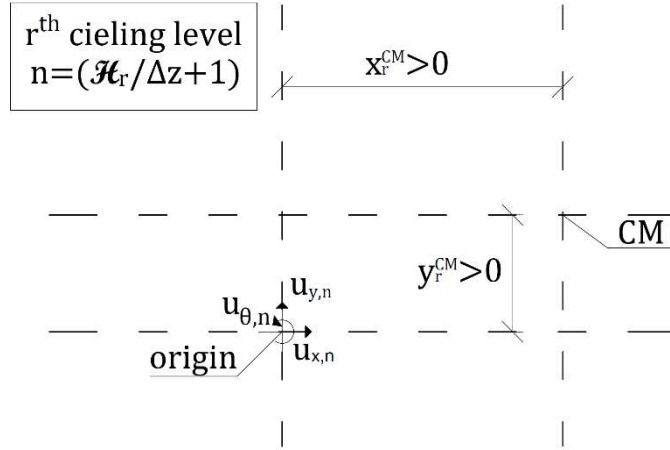
299 The parameters  $x_{\ell,n}^{\text{dis}}$  and  $y_{\ell,n}^{\text{dis}}$  are the horizontal distances between the center of the  $\ell^{\text{th}}$  element and  
 300 the DOFs origin – depicted in Fig. 8. In Eq. (44),  $\tilde{\mathbf{0}}$  is a  $N+1$ -dimensional vector of zeros,  $\mathbf{e}_r$  denotes a  
 301 vector whose elements are all zero except for the  $r = \mathcal{H}_r / \Delta z + 1$  component whose value is "1.0",  
 302 and  $\mathbf{ROI}_r$  is the  $r^{\text{th}}$  ceiling radius-of-inertia about the DOFs origin, which is given by:

303  $ROI_r^2 = (ROI_r^{CM})^2 + (x_r^{CM})^2 + (y_r^{CM})^2 \quad \forall \quad r = 1, 2, \dots, R$  (47)

304 where  $ROI_r^{CM}$  is the  $r^{\text{th}}$  ceiling radius-of-inertia about its CM, and the parameters  $x_r^{CM}$  and  $y_r^{CM}$  are  
 305 the horizontal distances between the ceiling's CM and the DOFs origin – depicted in Fig. 9.



306  
 307 **Fig. 8.** Distances between the  $l^{\text{th}}$  element and the global DOFs origin



308  
 309 **Fig. 9.** Distances between the CM and the global DOFs origin

310 The global stiffness matrix  $\tilde{\mathbf{k}}_{\Delta z}$  is the combination of the element stiffness matrices  $\mathbf{k}_{\Delta z, \ell=1, 2, \dots}$   
 311 transformed into global displacement coordinates using the Direct Stiffness Method (DSM):

312  $\tilde{\mathbf{k}}_{\Delta z} = \sum_{\ell} \mathbf{a}_{k, \ell} \begin{bmatrix} \mathbf{k}_{\Delta z, \ell} & \mathbf{0}_{N_{\ell} \times N - N_{\ell}} \\ \mathbf{0}_{N - N_{\ell} \times N_{\ell}} & \mathbf{0}_{N - N_{\ell} \times N - N_{\ell}} \end{bmatrix} \mathbf{a}_{k, \ell}^T$  (48)

313  $\mathbf{a}_{k, \ell} = \begin{bmatrix} 1 & & \rho_{xy \ell, 0} & & -y_{\ell, 0}^{\text{dis}} & & \\ & \ddots & & \ddots & & & \\ & & 1 & & \rho_{xy \ell, N} & & -y_{\ell, N}^{\text{dis}} \end{bmatrix}^T$  (49a)

314  $\mathbf{a}_{k, \ell} = \begin{bmatrix} \rho_{yx \ell, 0} & & & & 1 & & x_{\ell, 0}^{\text{dis}} & & \\ & \ddots & & & & & & \ddots & \\ & & \rho_{yx \ell, N} & & & & 1 & & x_{\ell, N}^{\text{dis}} \end{bmatrix}^T$  (49b)

315 In Eq. (48), the zeros matrices ( $\mathbf{0}_{N_{\ell} \times N - N_{\ell}}$ ,  $\mathbf{0}_{N - N_{\ell} \times N_{\ell}}$ , and  $\mathbf{0}_{N - N_{\ell} \times N - N_{\ell}}$ ) treat the case of  $H_{\ell} < H_R$ . The  
 316 transformation matrix  $\mathbf{a}_{k, \ell}$  of Eq. (49a) transforms an element whose strong\primary moment-of-

317 inertia is in the  $x$ - $z$  plane, and  $\rho_{xy\ell,n}$  is the stiffness mutuality from the  $x$ -direction to the  $y$ -direction  
 318 at the  $n^{\text{th}}$  DOF level. The transformation matrix  $\mathbf{a}_{k,\ell}$  of Eq. (49b) transforms an element whose strong  
 319 moment-of-inertia is in the  $y$ - $z$  plane, and  $\rho_{yx\ell,n}$  is the stiffness mutuality from the  $y$ -direction to the  
 320  $x$ -direction at the  $n^{\text{th}}$  DOF level. If an element has significant moment-of-inertia quantities in its'  
 321 primary perpendicular directions, it is transformed twice for each direction.

322 The  $3N+3 \times 3N+3$  global inherent damping matrix  $\tilde{\mathbf{c}}_{\Delta z}$  is determined according to  $\tilde{\mathbf{m}}_{\Delta z}$  and  $\tilde{\mathbf{k}}_{\Delta z}$   
 323 using Caughey classical damping:

$$324 \quad \tilde{\mathbf{c}}_{\Delta z} = \tilde{\mathbf{m}}_{\Delta z} \left( \sum_{v=1}^{3N+3} 2 \zeta_v \tilde{\omega}_{\Delta z,v} / \left( \tilde{\Phi}_{\Delta z,v}^T \tilde{\mathbf{m}}_{\Delta z} \tilde{\Phi}_{\Delta z,v} \right) \tilde{\Phi}_{\Delta z,v} \tilde{\Phi}_{\Delta z,v}^T \right) \tilde{\mathbf{m}}_{\Delta z} \quad (50)$$

325 where  $\zeta_v$  is the damping ratio assigned to the  $v^{\text{th}}$  mode and  $\tilde{\omega}_v$  and  $\tilde{\Phi}_v$  denote the  $v^{\text{th}}$  modal angular  
 326 frequency and  $v^{\text{th}}$  mode shape vector, respectively, which stem from:

$$327 \quad \det|\tilde{\mathbf{m}}_{\Delta z}^{-1} \tilde{\mathbf{k}}_{\Delta z} - \tilde{\omega}_{\Delta z,v}^2 \mathbf{I}| = 0 \quad \leftrightarrow \quad \tilde{\omega}_{\Delta z,1} < \tilde{\omega}_{\Delta z,2} < \dots \quad (51)$$

$$328 \quad (\tilde{\mathbf{m}}_{\Delta z}^{-1} \tilde{\mathbf{k}}_{\Delta z} - \tilde{\omega}_{\Delta z,v}^2 \mathbf{I}) \tilde{\Phi}_{\Delta z,v} = \mathbf{0} \quad \forall \quad v = 1, 2, \dots, \infty \quad (52)$$

329 Eqs. (38)-(50) conclude the three-dimensional structure's matrix equations model. Continuing, the  
 330 matrix equations models of the two-dimensional cantilever element and three-dimensional structure  
 331 are now enhanced with the material's inelastic mechanical properties.

#### 332 4. Inelastic two-dimensional element

##### 333 4.1. Smooth hysteretic model

334 The smooth hysteretic model for deteriorating inelastic structures in Sivaselvan and  
 335 Reinhorn[13] is employed to implement mechanical behavior of a cross-section subjected to  
 336 gravitational load and time-varying bending-moment. The smooth hysteretic model defines the  
 337 relation between the first-order-time-derivatives of the bending-moment and the bending-curvature  
 338 through the bending-stiffness:

$$339 \quad \dot{\mathcal{M}}^R(z, t) = \kappa(z, \varphi, \dot{\varphi}) \dot{\varphi}(z, t) \quad (53)$$

340 where  $\kappa(z, \varphi, \dot{\varphi})$  is the inelastic bending-stiffness. The bending-stiffness considers nonsymmetrical  
 341 yielding between the positive and negative yield bending-moments, stiffness degradation, strength  
 342 degradation, and the possibility of a pinching effect.

343 In the case where the pinching effect is not regarded,  $\kappa(z, \varphi, \dot{\varphi})$  is a combination of the  
 344 permanent portion of the initial bending-stiffness and the hysteretic bending-stiffness portion:

345  $\kappa(z, \varphi, \dot{\varphi}) = a \kappa^0(z) + \kappa^*(z, \mathcal{M}^{R*}, \dot{\varphi})$  (54)

346 where  $\kappa^0(z)$  denote the initial bending-stiffness and since shear deformations are neglected, due to  
 347 the introduction of Euler-Bernoulli assumption, it is equal to the elasticity distribution:

348  $\kappa^0(z) = EI(z)$  (55)

349 Also, in Eq. (54),  $\kappa^*(z, \mathcal{M}^{R*}, \dot{\varphi})$  is the hysteretic bending-stiffness portion, and  $a$  is the ratio of post-  
 350 yielding to initial stiffness. The function  $\mathcal{M}^{R*}(z,t)$  is the hysteretic portion of  $\mathcal{M}^R(z,t)$  and is given by

351  $\mathcal{M}^{R*}(z, t) = \mathcal{M}^R(z, t) - a \kappa^0(z) \varphi(z, t)$  (56)

352 In the case where the pinching effect is regarded, the total bending-stiffness is calculated as follows:

353  $\kappa(z, \varphi, \dot{\varphi}) = a \kappa^0(z) + \frac{\kappa^*(z, \mathcal{M}^{R*}, \dot{\varphi}) \kappa^P(\mathcal{M}^{R*}, \vartheta)}{\kappa^*(z, \mathcal{M}^{R*}, \dot{\varphi}) + \kappa^P(\mathcal{M}^{R*}, \vartheta)}$  (57)

354 where  $\kappa^P(\mathcal{M}^{R*}, \vartheta)$  is the pinching stiffness and is connected in "series" to  $\kappa^*(z, \mathcal{M}^{R*}, \dot{\varphi})$ .

355 The equation of  $\kappa^*(z, \mathcal{M}^{R*}, \dot{\varphi})$  is formulated so that the hysteretic portion is related to the  
 356 ratio between the bending-moment and the yielding moment:

357  $\kappa^*(z, \mathcal{M}^{R*}, \dot{\varphi}) = (R^K(z, \mathcal{M}^R, \varphi) - a) \kappa^0(z) \left| \frac{\mathcal{M}^{R*}(z,t)}{\mathcal{M}^{yld*}(z)} \right|^v \left[ \eta_1 \operatorname{sgn}(\mathcal{M}^{R*}(z, t) \dot{\varphi}(z, t)) + \eta_2 \right]$  (58)

358 In Eq. (58),  $v$  is the parameter controlling the smoothness of the transition from elastic to plastic  
 359 region,  $\eta_1$  and  $\eta_2 = 1 - \eta_1$  are parameters controlling the shape of the unloading curve,  $R^K(z, \mathcal{M}^R, \varphi)$   
 360 is the stiffness degradation factor in  $z$  whose behavior is adjusted by the degradation parameter  $\alpha$   
 361 as follows:

362  $R^K(z, \mathcal{M}^R, \varphi) = \frac{(|\mathcal{M}^R(z,t)| + \alpha \mathcal{M}^{yld}(z))}{(|\kappa^0(z) \vartheta(z,t)| + \alpha \mathcal{M}^{yld}(z))}$  (59)

363 Also, in Eq. (58),  $\mathcal{M}^{yld*}(z)$  is the hysteretic portion of the yielding moment  $\mathcal{M}^{yld}(z)$  and is given by:

364  $\mathcal{M}^{yld*}(z) = (1 - a) \mathcal{M}^{yld}(z)$  (60)

365 In Eqs. (59) and (60), in a case where  $\mathcal{M}^{yld}(z)$  is nonsymmetric, it is defined as:

366  $\mathcal{M}^{yld}(z) = 0.5 \left[ \left( 1 + \operatorname{sgn}(\mathcal{M}^{R*}(z, t)) \right) \mathcal{M}^{yld,+}(z) + \left( 1 - \operatorname{sgn}(\mathcal{M}^{R*}(z, t)) \right) \mathcal{M}^{yld,-}(z) \right]$  (61)

367 in which  $\mathcal{M}^{yld,+}(z)$  and  $\mathcal{M}^{yld,-}(z)$  denote the positive/negative yielding bending-moments. Eq (61)  
 368 is added with a correction suggested by Wang et al.[14]. The yielding bending-moments' degraded  
 369 quantity (i.e., degraded strength) is calculated using the following continuous terms:

$$\begin{aligned}
370 \quad \dot{\mathcal{M}}^{yld,+}(z) = \mathcal{M}^{y0,+}(z) & \left\{ \left[ 1 - \frac{\beta_2}{1-\beta_2} \frac{E^{yld}(z,t)}{E^{ult}(z)} \right] \left[ -\frac{1}{\beta_1} \left( \frac{1}{\varphi^{ult,+}(z)} \right)^{\frac{1}{\beta_1}} \max_t |\varphi^+(z,t)|^{\frac{1-\beta_1}{\beta_1}} \right] \frac{d \max_t |\varphi^+(z,t)|}{dt} + \dots \right. \\
& \left. \left[ 1 - \left( \frac{\max_t |\varphi^+(z,t)|}{\varphi^{ult,+}(z)} \right)^{\frac{1}{\beta_1}} \right] \left[ -\frac{\beta_2}{1-\beta_2} \frac{1}{E^{ult}(z)} \right] \dot{E}^{yld}(z,t) \right\} \quad (62)
\end{aligned}$$

$$\begin{aligned}
371 \quad \dot{\mathcal{M}}^{yld,-}(z) = \mathcal{M}^{y0,-}(z) & \left\{ \left[ 1 - \frac{\beta_2}{1-\beta_2} \frac{E^{yld}(z,t)}{E^{ult}(z)} \right] \left[ -\frac{1}{\beta_1} \left( \frac{1}{\varphi^{ult,-}(z)} \right)^{\frac{1}{\beta_1}} \max_t |\varphi^-(z,t)|^{\frac{1-\beta_1}{\beta_1}} \right] \frac{d \max_t |\varphi^-(z,t)|}{dt} + \dots \right. \\
& \left. \left[ 1 - \left( \frac{\max_t |\varphi^-(z,t)|}{\varphi^{ult,-}(z)} \right)^{\frac{1}{\beta_1}} \right] \left[ -\frac{\beta_2}{1-\beta_2} \frac{1}{E^{ult}(z)} \right] \dot{E}^{yld}(z,t) \right\} \quad (63)
\end{aligned}$$

372 where  $\mathcal{M}^{y0,+}(z)/\mathcal{M}^{y0,-}(z)$  are the *initial* positive/negative yield bending-moments,  $\varphi^+(z,t)/\varphi^-(z,t)$   
373 are the positive/negative bending-curvatures,  $\varphi^{ult,+}(z)/\varphi^{ult,-}(z)$  are the ultimate positive/negative  
374 bending-curvatures,  $\beta_1$  is the ductility-based strength degradation parameter,  $E^{yld}(z,t)$  is the  
375 energy dissipated by yielding,  $\beta_2$  is the energy-based strength degradation parameter, and  $E^{ult}(z)$   
376 is the ultimate dissipated energy by yielding, which is calculated by loading the cross-section  
377 monotonically to reach the ultimate curvature without any degradation:

$$378 \quad E^{ult}(z) = \min \left\{ \int_0^{\varphi^{ult,+}} \mathcal{M}^R(z, \varphi) d\varphi \quad , \quad \int_0^{\varphi^{ult,-}} \mathcal{M}^R(z, \varphi) d\varphi \right\} \quad (64)$$

379 The pinching stiffness  $\kappa^P(\mathcal{M}^{R*}, \varphi)$  is usually a result of cracks closure and is added in series  
380 to the hysteretic bending-stiffness to model this effect. The pinching stiffness is modeled as the  
381 inverse of the probability density function of the normal distribution with an expected value  
382  $\bar{\mathcal{M}}^{R*}(z) = \lambda \mathcal{M}^{yld*}(z)$  (i.e., the mean moment level about which pinching occurs) and with variance  
383  $\mathcal{M}^{\sigma*}(z) = \sigma \mathcal{M}^{yld*}(z)$  (i.e., the measure of the moment range over which slip occurs):

$$384 \quad \kappa^P(\mathcal{M}^{R*}, \varphi) = \sqrt{\frac{\pi \mathcal{M}^{\sigma*}}{2s}} \exp \left\{ \frac{2(\mathcal{M}^{\sigma*}(z))^2}{(\mathcal{M}^{R*}(z,t) - \bar{\mathcal{M}}^{R*}(z))^2} \right\} \quad (65)$$

385 Here,  $s$  is the pinching length and is defined according to the pinching length factor  $R_s$  as follows:

$$386 \quad s = R_s \left[ \max_t \{\varphi^+(z,t)\} - \min_t \{\varphi^-(z,t)\} \right] \quad (66)$$

387 That sums up the smooth hysteretic model. Equations (53)-(66) above define the inelastic bending-  
388 stiffness behavior and are now implemented in the two-dimensional cantilever element's matrix  
389 equations modeling.

#### 390 4.2. Inelastic matrix equations model

391 The structural analysis of the inelastic model is performed in bending-curvature coordinates.  
 392 Double integrating both sides of Eq. (1) using  $\int_H^z \int_H^z dz dz$  integration limits leads to the following  
 393 bending-moment equilibrium with no additional integration coefficients:

$$\begin{aligned}
 & \mathcal{M}^I(z, t) + \mathcal{M}^R(z, t) = \mathcal{M}^P(z, t) \\
 & \text{s. t.} \\
 & \dot{\mathcal{M}}^R(z, t) = \kappa(z, \varphi, \dot{\varphi}) \varphi(z, t) \\
 & 0 \leq z \leq H \\
 394 \quad & i \quad \left. \begin{aligned} & \mathcal{V}^R(H, t) = 0 \\ & \mathcal{V}^I(H, t) = 0 \\ & \mathcal{V}^P(H, t) = 0 \end{aligned} \right\} \text{BC} \\
 & ii \quad \left. \begin{aligned} & \mathcal{M}^R(H, t) = 0 \\ & \mathcal{M}^I(H, t) = 0 \\ & \mathcal{M}^P(H, t) = 0 \end{aligned} \right\} \text{BC}
 \end{aligned} \tag{67}$$

395 where  $\mathcal{M}^I(z, t)$  is the bending-moment in  $z$  applied by the lateral inertia force  $m(z)\ddot{u}^w(z, t)$ , and  
 396  $\mathcal{M}^P(z, t)$  is the bending-moment in  $z$  applied by the lateral load  $p(z, t)$ . In the boundary conditions,  
 397  $\mathcal{V}^I(z, t)$  is the distributed shear force due to the lateral inertia force and  $\mathcal{V}^P(z, t)$  is the distributed  
 398 shear force due to the lateral load.

399 Eq. (68) represents Eq. (67) in matrix equations form by referring to the bending-moments'  
 400 equilibrium at the  $n = 0, 1, \dots, N$  lateral DOF levels.

$$\begin{aligned}
 & \mathcal{M}_{\Delta z}^I(t) + \mathcal{M}_{\Delta z}^R(t) = \mathcal{M}_{\Delta z}^P(t) \\
 & \text{s. t.} \\
 & \dot{\mathcal{M}}_{\Delta z}^R(t) = \kappa_{\Delta z}(\varphi_{\Delta z}, \dot{\varphi}_{\Delta z}) \varphi_{\Delta z}(t) \\
 401 \quad & i \quad \left. \begin{aligned} & \mathcal{V}_{\Delta z N+1}^R(t) = \left[ \mathbf{T}_{z \in [H \rightarrow 0]}^f \mathbf{f}_{\Delta z}^R(t) \right]_{N+1} = 0 \\ & \mathcal{V}_{\Delta z N+1}^I(t) = \left[ \mathbf{T}_{z \in [H \rightarrow 0]}^f \mathbf{m}_{\Delta z} \ddot{\mathbf{u}}_{\Delta z}^w(t) \right]_{N+1} = 0 \\ & \mathcal{V}_{\Delta z N+1}^P(t) = \left[ \mathbf{T}_{z \in [H \rightarrow 0]}^f \mathbf{p}_{\Delta z}(t) \right]_{N+1} = 0 \end{aligned} \right\} \\
 & ii \quad \left. \begin{aligned} & \mathcal{M}_{\Delta z N+1}^R(t) = \left[ \mathbf{T}_{z \in [H \rightarrow 0]}^f \mathcal{V}_{\Delta z}^R \right]_{N+1} = 0 \\ & \mathcal{M}_{\Delta z N+1}^I(t) = \left[ \mathbf{T}_{z \in [H \rightarrow 0]}^f \mathcal{V}_{\Delta z}^I \right]_{N+1} = 0 \\ & \mathcal{M}_{\Delta z N+1}^P(t) = \left[ \mathbf{T}_{z \in [H \rightarrow 0]}^f \mathcal{V}_{\Delta z}^P \right]_{N+1} = 0 \end{aligned} \right\} \text{BC.} \\
 & iii \quad \mathbf{u}_{\Delta z 1}^{w'}(t) = \left[ \mathbf{T}_{z \in [0 \rightarrow H]}^f \boldsymbol{\varphi}_{\Delta z}(t) \right]_1 = 0 \\
 & iv \quad \mathbf{u}_{\Delta z 1}^w(t) = \left[ \mathbf{T}_{z \in [0 \rightarrow H]}^f \mathbf{u}_{\Delta z}^{w'}(t) \right]_1 = 0 \\
 & n = 1, \dots, N+1 \quad ; \quad N+1 = H/\Delta z + 1
 \end{aligned} \tag{68} \quad \forall \quad v = 1, 2, \dots, \infty$$

402 where the newly introduced vector terms in Eq. (68) refer to the value of their respected continuous  
 403 functions at the lateral DOF levels:

$$\begin{aligned}
\mathcal{M}_{\Delta z}^R(t) &= [\mathcal{M}^R(0, t), \dots, \mathcal{M}^R(n \Delta z, t), \dots, \mathcal{M}^R(N \Delta z, t)]^T \\
\mathcal{M}_{\Delta z}^I(t) &= [\mathcal{M}^I(0, t), \dots, \mathcal{M}^I(n \Delta z, t), \dots, \mathcal{M}^I(N \Delta z, t)]^T \\
\mathcal{M}_{\Delta z}^P(t) &= [\mathcal{M}^P(0, t), \dots, \mathcal{M}^P(n \Delta z, t), \dots, \mathcal{M}^P(N \Delta z, t)]^T \\
\mathcal{V}_{\Delta z}^R(t) &= [\mathcal{V}^R(0, t), \dots, \mathcal{V}^R(n \Delta z, t), \dots, \mathcal{V}^R(N \Delta z, t)]^T \\
\mathcal{V}_{\Delta z}^I(t) &= [\mathcal{V}^I(0, t), \dots, \mathcal{V}^I(n \Delta z, t), \dots, \mathcal{V}^I(N \Delta z, t)]^T \\
\mathcal{V}_{\Delta z}^P(t) &= [\mathcal{V}^P(0, t), \dots, \mathcal{V}^P(n \Delta z, t), \dots, \mathcal{V}^P(N \Delta z, t)]^T \\
\mathbf{f}_{\Delta z}^R(t) &= [f^R(0, t), \dots, f^R(n \Delta z, t), \dots, f^R(N \Delta z, t)]^T \\
\boldsymbol{\varphi}_{\Delta z}(t) &= [\varphi(0, t), \dots, \varphi(n \Delta z, t), \dots, \varphi(N \Delta z, t)]^T \\
\dot{\boldsymbol{\varphi}}_{\Delta z}(t) &= [\dot{\varphi}(0, t), \dots, \dot{\varphi}(n \Delta z, t), \dots, \dot{\varphi}(N \Delta z, t)]^T \\
\mathbf{u}_{\Delta z}^W(t) &= [u^W(0, t), \dots, u^W(n \Delta z, t), \dots, u^W(N \Delta z, t)]^T \\
\mathbf{u}_{\Delta z}^{W'}(t) &= [u^{W'}(0, t), \dots, u^{W'}(n \Delta z, t), \dots, u^{W'}(N \Delta z, t)]^T \\
\ddot{\mathbf{u}}_{\Delta z}^W(t) &= [\ddot{u}^W(0, t), \dots, \ddot{u}^W(n \Delta z, t), \dots, \ddot{u}^W(N \Delta z, t)]^T
\end{aligned} \tag{69}$$

405 The bending-moment due to the lateral load vector is  $\mathcal{M}_{\Delta z}^P(t)$ :

$$406 \quad \mathcal{M}_{\Delta z}^P(t) = \mathbf{T}_{z \in [H \rightarrow z]}^{f dz} \mathbf{T}_{z \in [H \rightarrow z]}^{f dz} \mathbf{p}_{\Delta z}(t) \tag{70}$$

407 and the bending-stiffness matrix is of the diagonal form:

$$408 \quad \boldsymbol{\kappa}_{\Delta z}(\boldsymbol{\varphi}_{\Delta z}, \dot{\boldsymbol{\varphi}}_{\Delta z}) = \Delta z \text{diag}\{\kappa(0, \varphi, \dot{\varphi}) \quad \dots \quad \kappa(n \Delta z, \varphi, \dot{\varphi}) \quad \dots \quad \kappa(N \Delta z, \varphi, \dot{\varphi})\} \tag{71}$$

409 Note that since Eqs. (68)-(71) analyze the structure in bending-coordinates; no matrix inversion is  
410 required by the terms above. The displacement vector  $\mathbf{u}_{\Delta z}^W(t)$  is determined using the LRS integration  
411 transformation matrix. For determining the modal properties of the structure, one requires the  
412 bending-stiffness matrix  $\boldsymbol{\kappa}_{\Delta z}(\boldsymbol{\varphi}_{\Delta z}, \dot{\boldsymbol{\varphi}}_{\Delta z})$  and the bending-curvature-related-mass matrix, denoted as  
413  $\mathbf{m}_{\Delta z}$ , which is given by:

$$414 \quad \mathbf{m}_{\Delta z} = \mathbf{T}_{z \in [H \rightarrow 0]}^{f dz} \mathbf{T}_{z \in [H \rightarrow 0]}^{f dz} \mathbf{m}_{\Delta z} \mathbf{T}_{z \in [0 \rightarrow H]}^{f dz} \mathbf{T}_{z \in [0 \rightarrow H]}^{f dz} \leftrightarrow \mathcal{M}_{\Delta z}^I(t) = \mathbf{m}_{\Delta z} \ddot{\boldsymbol{\varphi}}_{\Delta z}(t) \tag{72}$$

415 That ends the matrix equations model formulation of the inelastic cantilever element. Next, the  
416 inelastic three-dimensional structure model is developed.

### 417 5. Inelastic three-dimensional structure

418 The equation-of-damped-motion of the inelastic three-dimensional structure, subjected to  
419 lateral and torsional loadings, is written as:

$$420 \quad \tilde{\mathbf{m}}_{\Delta z} \ddot{\tilde{\mathbf{u}}}_{\Delta z}(t) + \tilde{\mathbf{c}}_{\Delta z} \dot{\tilde{\mathbf{u}}}_{\Delta z}(t) + \tilde{\mathbf{f}}_{\Delta z}^H(\tilde{\mathbf{u}}_{\Delta z}, \dot{\tilde{\mathbf{u}}}_{\Delta z}) = \tilde{\mathbf{p}}_{\Delta z}(t) \tag{73}$$

421 where  $\tilde{\mathbf{m}}_{\Delta z}$ ,  $\tilde{\mathbf{c}}_{\Delta z}$ ,  $\tilde{\mathbf{p}}_{\Delta z}(t)$ ,  $\dot{\tilde{\mathbf{u}}}_{\Delta z}(t)$ , and  $\ddot{\tilde{\mathbf{u}}}_{\Delta z}(t)$  are given by the matrix equations model in 3 and  $\tilde{\mathbf{f}}_{\Delta z}^H$  is the  
422 introduced global hysteretic resisting force vector. Since this paper implements the smooth  
423 hysteretic model in 4.1, the three-dimensional structure is analyzed in bending-coordinates.



444 Performing matrix structural analysis using the above equations assess the global bending-  
 445 curvature and its' time derivatives,  $\tilde{\boldsymbol{\varphi}}_{\Delta z}(t)$ ,  $\dot{\tilde{\boldsymbol{\varphi}}}_{\Delta z}(t)$ , and  $\ddot{\tilde{\boldsymbol{\varphi}}}_{\Delta z}(t)$ . The global displacement vector, and  
 446 its time-derivatives, are calculated using the transformation matrix  $\mathbf{T}_{f \rightarrow \mathcal{M}}$ :

$$447 \left. \begin{aligned} \tilde{\mathbf{u}}_{\Delta z}(t) &= \mathbf{T}_{f \rightarrow \mathcal{M}}^T \tilde{\boldsymbol{\varphi}}_{\Delta z}(t) \\ \dot{\tilde{\mathbf{u}}}_{\Delta z}(t) &= \mathbf{T}_{f \rightarrow \mathcal{M}}^T \dot{\tilde{\boldsymbol{\varphi}}}_{\Delta z}(t) \\ \ddot{\tilde{\mathbf{u}}}_{\Delta z}(t) &= \mathbf{T}_{f \rightarrow \mathcal{M}}^T \ddot{\tilde{\boldsymbol{\varphi}}}_{\Delta z}(t) \end{aligned} \right\} \text{global DOFs} \quad (82)$$

448 Also, the elemental bending-curvature vector, lateral deformation vector, and their time-derivatives  
 449 are determined using the transformations:

$$450 \left. \begin{aligned} \boldsymbol{\varphi}_{\Delta z, \ell} &= \mathbf{a}_{k, \ell}^T \tilde{\boldsymbol{\varphi}}_{\Delta z}(t) \\ \dot{\boldsymbol{\varphi}}_{\Delta z, \ell} &= \mathbf{a}_{k, \ell}^T \dot{\tilde{\boldsymbol{\varphi}}}_{\Delta z}(t) \\ \mathbf{u}_{\Delta z, \ell}^w &= \mathbf{T}_{z \in [\mathcal{H}_R \rightarrow z]}^{\int dz} \mathbf{T}_{z \in [\mathcal{H}_R \rightarrow z]}^{\int dz} \boldsymbol{\varphi}_{\Delta z, \ell} \\ \dot{\mathbf{u}}_{\Delta z, \ell}^w &= \mathbf{T}_{z \in [\mathcal{H}_R \rightarrow z]}^{\int dz} \mathbf{T}_{z \in [\mathcal{H}_R \rightarrow z]}^{\int dz} \dot{\boldsymbol{\varphi}}_{\Delta z, \ell} \end{aligned} \right\} \text{element DOFs} \quad (83)$$

451 That concludes the matrix equations model of the inelastic three-dimensional structure and the  
 452 models' development.

## 453 6. Examples

454 Four examples for utilizing the developed matrix equations model are presented herein. All  
 455 examples refer to a  $B_\ell(z) = 0.3m$  thick RC wall of  $L_\ell(z) = 4.5m$  length and  $H_\ell = 60m$  height. The RC  
 456 wall elevation scheme is depicted in Fig. 10 and, as shown, it is of uniform mass distribution  $m_\ell(z) =$   
 457  $3.375 \text{ ton}/m$ , and uniform elasticity  $EI_\ell(z) = 6.424 \cdot 10^7 \text{ kNm}^2$ . The analysis mesh-size is set as  $\Delta z =$   
 458  $H_\ell/2,000 = 0.03m$  in all examples for resolving in minimal numerical error and relatively fast  
 459 calculation time.

460 The first example employs the matrix equations model developed in 2.2 for analyzing a two-  
 461 dimensional linearly-elastic model and determines its' modal properties. In example 2, the cantilever  
 462 wall is placed in a three-dimensional structure and studied using the equations model in 3. In  
 463 example 3 and example 4, the two-dimensional and three-dimensional structures' inelastic  
 464 mechanical behavior are implemented, respectively. In example 3, pushover analysis is applied to  
 465 the cantilever element, and in example 4 earthquake analysis is performed for the three-dimensional  
 466 structure.

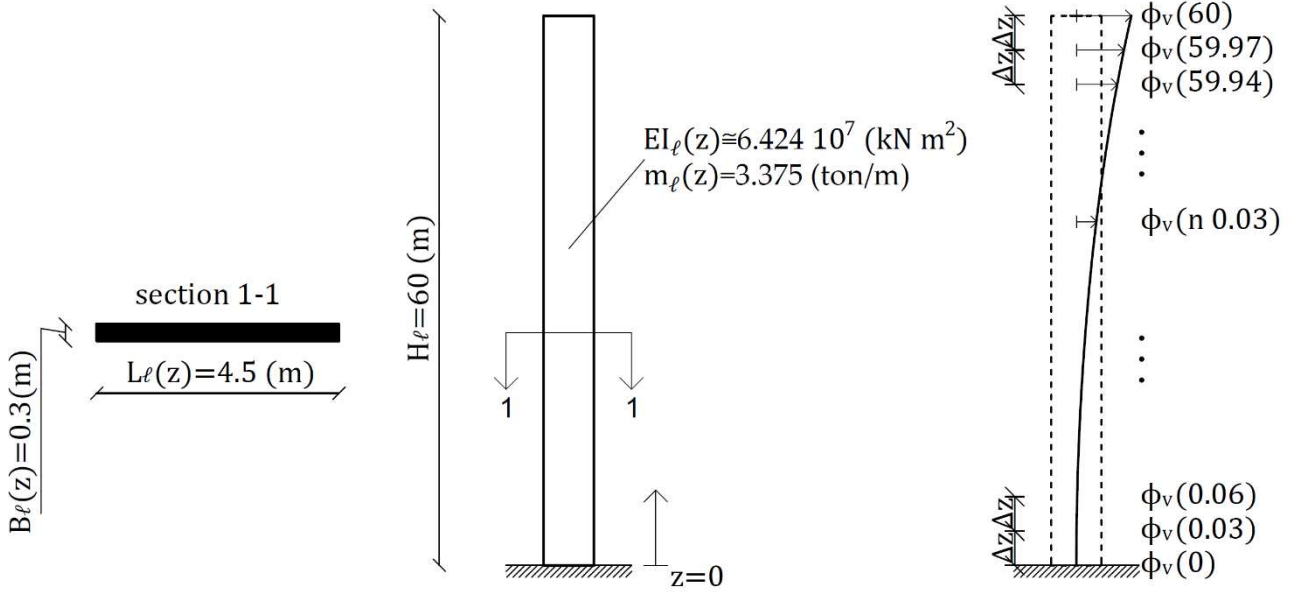


Fig. 10. Elevation scheme of the RC cantilever wall

### 6.1. Example 1: two-dimensional model

The first example acquires the cantilever wall's mass and stiffness matrices and examines the first eight modal systems. The number of lateral DOF levels is  $N = H_l / \Delta z = 2,000$  and, thus, the size of all matrices provided in the current example is  $2001 \times 2001$ . A stage-by stage-description for determining the mass and stiffness matrix is provided herein.

**Stage-a.** Define the integration matrices  $\mathbf{T}_{z \in [0 \rightarrow H_l]}^{\int dz}$  and  $\mathbf{T}_{z \in [H_l \rightarrow 0]}^{\int dz}$  – using Eq. (20)

Knowing that  $\Delta z = 0.03m$  and  $N = 2000$ , the  $2001 \times 2001$  LRS integration matrices are:

$$\mathbf{T}_{z \in [0 \rightarrow 60]}^{\int dz} = 0.03 \begin{bmatrix} 0 & 0 & 0 & \dots & 0 & 0 & 0 \\ 1 & 0 & 0 & \dots & 0 & 0 & 0 \\ 1 & 1 & 0 & \dots & 0 & 0 & 0 \\ \vdots & \vdots & \vdots & \ddots & \vdots & \vdots & \vdots \\ 1 & 1 & 1 & \dots & 0 & 0 & 0 \\ 1 & 1 & 1 & \dots & 1 & 0 & 0 \\ 1 & 1 & 1 & \dots & 1 & 1 & 0 \end{bmatrix}; \quad \mathbf{T}_{z \in [60 \rightarrow 0]}^{\int dz} = -0.03 \begin{bmatrix} 0 & 1 & 1 & \dots & 1 & 1 & 1 \\ 0 & 0 & 1 & \dots & 1 & 1 & 1 \\ 0 & 0 & 0 & \dots & 1 & 1 & 1 \\ \vdots & \vdots & \vdots & \ddots & \vdots & \vdots & \vdots \\ 0 & 0 & 0 & \dots & 0 & 1 & 1 \\ 0 & 0 & 0 & \dots & 0 & 0 & 1 \\ 0 & 0 & 0 & \dots & 0 & 0 & 0 \end{bmatrix}$$

**Stage-b.** Calculate the mass matrix  $\mathbf{m}_{\Delta z, \ell}$  – using Eq. (24)

Given that  $m_\ell(z) = 3.375 \text{ ton/m}$ , the mass matrix is:

$$\mathbf{m}_{\Delta z, \ell} = 3.375 \mathbf{I} \frac{\text{ton}}{m}$$

where  $\mathbf{I}$  is the  $2001 \times 2001$  identity matrix.

**Stage-c.** Determine the inverse form of the flexibility sub-matrix  $\mathcal{F}_{\Delta z, \ell}$  – using Eq. (18)

Given that  $EI_\ell(z) = 6.424 \cdot 10^7 \text{ kNm}^2$ , the elasticity matrix is:

$$\mathbf{EI}_{\Delta z, \ell} = 0.03 \cdot 6.424 \cdot 10^7 \mathbf{I} = 1.927 \cdot 10^6 \mathbf{I} \text{ kNm}^2.$$

484 The 2001×2001 flexibility matrix is calculated using the term:

$$485 \quad \mathbf{F}_{\Delta z, \ell} = \mathbf{T}_{z \in [0 \rightarrow H_\ell]}^{f dz} \mathbf{T}_{z \in [0 \rightarrow H_\ell]}^{f dz} (\mathbf{EI}_{\Delta z, \ell})^{-1} \mathbf{T}_{z \in [H_\ell \rightarrow 0]}^{f dz} \mathbf{T}_{z \in [H_\ell \rightarrow 0]}^{f dz} = \begin{bmatrix} \mathbf{0} & \mathbf{0} \\ \mathbf{0} & \mathcal{F}_{\Delta z, \ell} \end{bmatrix} \frac{m}{kN}$$

486 Then, the consequent 1,999×1,999 flexibility sub-matrix  $\mathcal{F}_{\Delta z, \ell}$  is extracted and employed in the next  
487 stage.

488 **Stage-d.** Construct the stiffness matrix  $\mathbf{k}_{\Delta z, \ell}$  – using Eqs. (22)

489 The matrices  $\mathcal{F}_{\Delta z, \ell}^{-1}$  and  $\mathbf{\Lambda}$  are used to construct  $\mathbf{k}_{\Delta z, \ell}$ . The components of  $\mathbf{\Lambda}$  are set as:

$$490 \quad \mathbf{\Lambda} = \begin{bmatrix} \Lambda_1 & 0 \\ 0 & \Lambda_2 \end{bmatrix} = \begin{bmatrix} 10^{20} & 0 \\ 0 & 10^{20} \end{bmatrix} \frac{kN}{m}$$

491 and the stiffness matrix is:

$$492 \quad \mathbf{k}_{\Delta z, \ell} = \begin{bmatrix} \mathbf{\Lambda} & \mathbf{0}_{2 \times N-1} \\ \mathbf{0}_{N-1 \times 2} & (\mathcal{F}_{\Delta z, \ell})^{-1} \end{bmatrix} \frac{kN}{m}$$

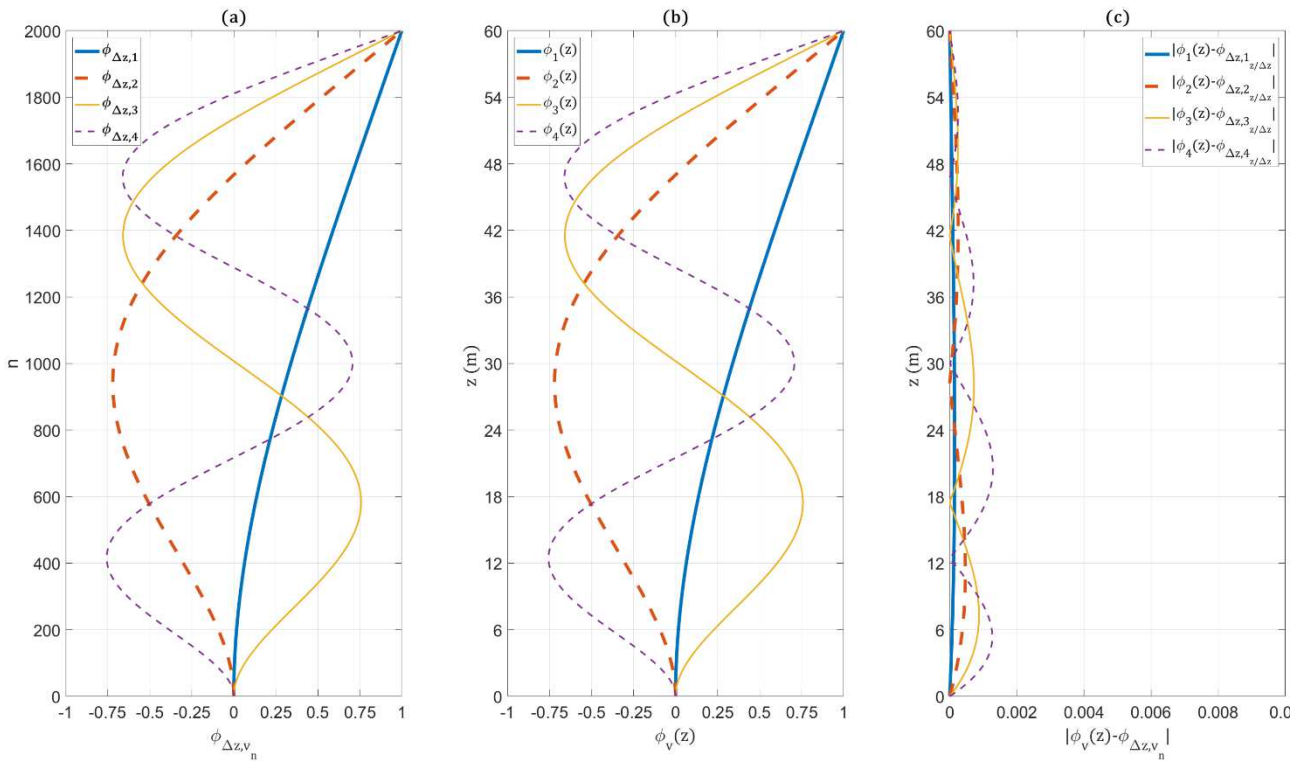
493 That concludes deriving the mass and stiffness matrices.

494 The modal frequencies and mode shapes are approximated (using Eqs. (33) and (34)) and  
495 compared to those of the analytical solution (using Eqs. (30)-(32)). Table 1 shows the relative error  
496 between the modal frequencies, and Fig. 11 and Fig. 12 illustrate the absolute error between the first  
497 eight mode shapes in  $z \in [0 \quad H_\ell]$ . It is shown that the more significant errors are located where the  
498 mode shape displacement is nearing zero (i.e.,  $\phi_v(z) \approx 0$ ). Nevertheless, the absolute error does not  
499 exceed the value of  $4 \cdot 10^{-3}$ .

500 **Table 1.** Example 1 RC wall's modal frequencies

v	$\omega_{\Delta z, v}$ rad/sec	$\omega_v$ rad/sec	$\frac{ \omega_{\Delta z, v} - \omega_v }{ \omega_v }$ rad/sec
1	4.26	4.26	$2.29 \cdot 10^{-5}$
2	26.70	26.70	$2.73 \cdot 10^{-7}$
3	74.77	74.77	$1.16 \cdot 10^{-6}$
4	146.52	146.52	$4.61 \cdot 10^{-6}$
5	242.21	242.21	$9.57 \cdot 10^{-6}$
6	361.82	361.83	$1.63 \cdot 10^{-5}$
7	505.35	505.36	$2.45 \cdot 10^{-5}$
8	672.79	672.82	$3.45 \cdot 10^{-5}$

501



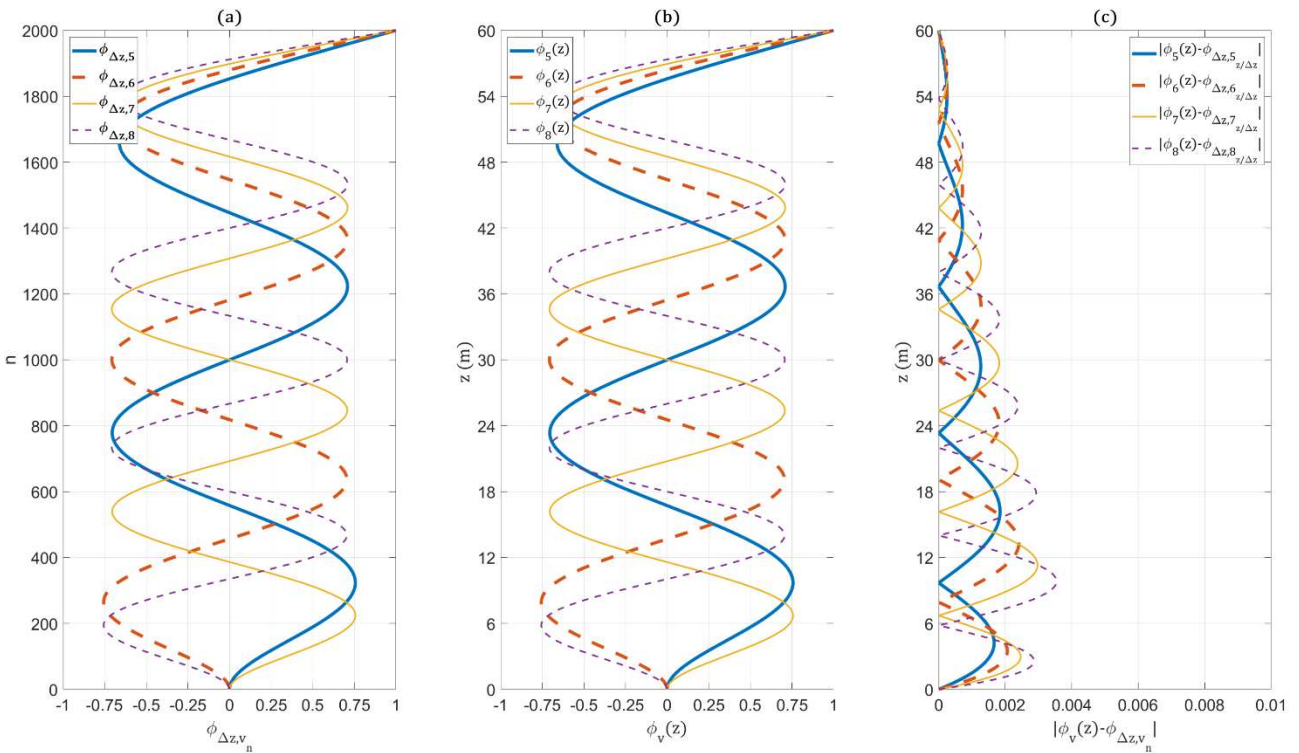
502

503

504

**Fig. 11.** Example 1 RC wall's mode shapes  $v=1,2,3,4$ : (a) matrix model, (b) analytical solution, (c) absolute error

505



506

507

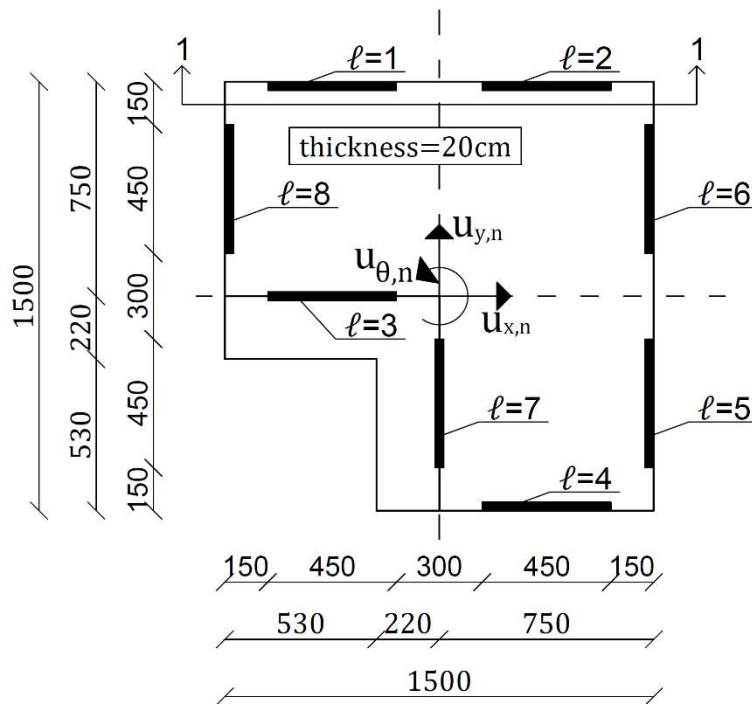
508

**Fig. 12.** Example 1 RC wall's mode shapes  $v=5,6,7,8$ : (a) matrix model, (b) analytical solution, (c) absolute error

509

510 6.2. Example 2: three-dimensional model

511 The RC wall in Example 1 is used to carry the gravitational and lateral loads of a 20-story  
 512 building. Fig. 13 and Fig. 14 depict its' floor plan and elevation scheme, respectively. The RC walls  
 513 are located asymmetrically about the global DOFs origin, chosen to be positioned at the center of the  
 514 circumscribed square. The ceiling thickness is 20cm, and the stories height is 3.0m (i.e.,  $\mathcal{H}_{r=1} = 3.0m$ ,  
 515  $\mathcal{H}_{r=2} = 6.0m, \dots, \mathcal{H}_{R=20} = 60.0m$ ). Considering the structure's geometry and the cantilever wall's  
 516 stiffness and mass matrices from the previous example, the current example first calculates the mass  
 517 and stiffness matrices of the three-dimensional structure according to the stage-by-stage-description  
 518 below.



519 **Fig. 13.** Example 2 asymmetrical floor plan  
 520

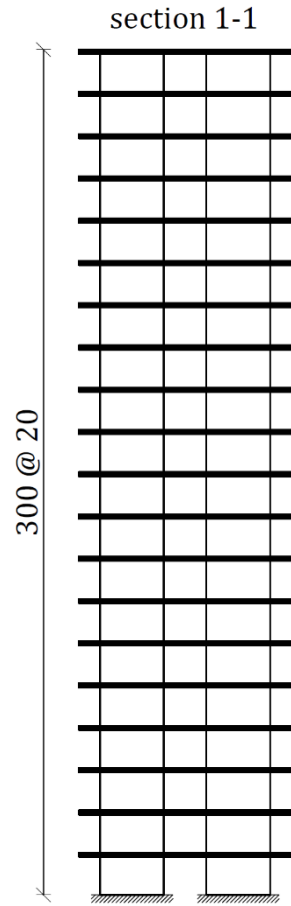


Fig. 14. Example 2 building elevation scheme

521  
522

523 **Stage-a.** Determine the transformation matrices  $\mathbf{a}_{m1,\ell}$  for the  $\ell=1,2,\dots,8$  elements – using Eq. (43)  
 524 The matrix  $\mathbf{a}_{m1,\ell}$  transforms the  $\ell^{\text{th}}$  cantilever wall mass matrix into the global coordinates and adds  
 525 its' contribution to the global mass matrix  $\tilde{\mathbf{m}}_{\Delta z}$ . The elements' distance coordinates about the DOF  
 526 origin are:

$$\begin{array}{l}
 \ell = 1: \left\{ \begin{array}{l} x_{1,n}^{\text{dis}} = -3.75 \text{ m} \\ y_{1,n}^{\text{dis}} = 7.35 \text{ m} \end{array} \right. \quad \ell = 5: \left\{ \begin{array}{l} x_{5,n}^{\text{dis}} = 7.35 \text{ m} \\ y_{5,n}^{\text{dis}} = -3.75 \text{ m} \end{array} \right. \\
 \ell = 2: \left\{ \begin{array}{l} x_{2,n}^{\text{dis}} = 3.75 \text{ m} \\ y_{2,n}^{\text{dis}} = 7.35 \text{ m} \end{array} \right. \quad \ell = 6: \left\{ \begin{array}{l} x_{6,n}^{\text{dis}} = 7.35 \text{ m} \\ y_{6,n}^{\text{dis}} = 3.75 \text{ m} \end{array} \right. \\
 \ell = 3: \left\{ \begin{array}{l} x_{3,n}^{\text{dis}} = -3.75 \text{ m} \\ y_{3,n}^{\text{dis}} = 0.0 \text{ m} \end{array} \right. \quad \ell = 7: \left\{ \begin{array}{l} x_{7,n}^{\text{dis}} = 0.0 \text{ m} \\ y_{7,n}^{\text{dis}} = -3.75 \text{ m} \end{array} \right. \\
 \ell = 4: \left\{ \begin{array}{l} x_{4,n}^{\text{dis}} = 3.75 \text{ m} \\ y_{4,n}^{\text{dis}} = -7.35 \text{ m} \end{array} \right. \quad \ell = 8: \left\{ \begin{array}{l} x_{8,n}^{\text{dis}} = -7.35 \text{ m} \\ y_{8,n}^{\text{dis}} = 3.75 \text{ m} \end{array} \right.
 \end{array} \quad \forall \quad n = 0,1, \dots, 2000$$

527

528 Using the distance coordinates in Eqs. (45) and (46) gives the cantilever walls' radius-of-inertia  
 529 matrices:

$$\begin{array}{l}
 \ell = 1: \mathbf{ROI}_{\Delta z,1} = 8.353 \text{ I m} \quad ; \quad \ell = 5: \mathbf{ROI}_{\Delta z,5} = 8.353 \text{ I m} \\
 \ell = 2: \mathbf{ROI}_{\Delta z,2} = 8.353 \text{ I m} \quad ; \quad \ell = 6: \mathbf{ROI}_{\Delta z,6} = 8.353 \text{ I m} \\
 \ell = 3: \mathbf{ROI}_{\Delta z,3} = 3.97 \text{ I m} \quad ; \quad \ell = 7: \mathbf{ROI}_{\Delta z,7} = 3.97 \text{ I m} \\
 \ell = 4: \mathbf{ROI}_{\Delta z,4} = 8.353 \text{ I m} \quad ; \quad \ell = 8: \mathbf{ROI}_{\Delta z,8} = 8.353 \text{ I m}
 \end{array}$$

530

531 and, closing *Stage-a*, we determine  $\mathbf{a}_{m1,\ell}$  of  $6003 \times 6003$  size for all the RC walls:

$$532 \quad \mathbf{a}_{m1,\ell} = \begin{bmatrix} \mathbf{I} & \mathbf{0} & \mathbf{0} \\ \mathbf{0} & \mathbf{I} & \mathbf{0} \\ \mathbf{0} & \mathbf{0} & \mathbf{ROI}_{\Delta z,\ell} \mathbf{ROI}_{\Delta z,\ell} \end{bmatrix} \quad \forall \quad \ell = 1, \dots, 8$$

533 **Stage-b.** Determine the transformation matrices  $\mathbf{a}_{m2,r}$  for the  $r=1, \dots, 20$  ceilings – using Eq. (44)

534 The matrix  $\mathbf{a}_{m2,r}$  is used for transforming the  $r^{\text{th}}$  ceiling mass matrix into the global coordinates and  
535 adding it to the global mass matrix. The distances between the ceilings' CM and the DOFs origin:

$$536 \quad \left. \begin{array}{l} x_r^{\text{CM}} = 0.692 \text{ m} \\ y_r^{\text{CM}} = 0.692 \text{ m} \end{array} \right\} \quad \forall \quad r = 1, 2, \dots, 20$$

537 The ceilings' radius-of-inertia about the DOFs origin is:

$$538 \quad \text{ROI}_r = \left( (\text{ROI}_r^{\text{CM}})^2 + (x_r^{\text{CM}})^2 + (y_r^{\text{CM}})^2 \right)^{0.5} = 5.956 \text{ m} \quad \forall \quad r = 1, 2, \dots, 20$$

539 and the  $6003 \times 3$  transformation matrix of the  $r^{\text{th}}$  ceiling is:

$$540 \quad \mathbf{a}_{m2,r} = \begin{bmatrix} \mathbf{e}_r & \tilde{\mathbf{0}} & \tilde{\mathbf{0}} \\ \tilde{\mathbf{0}} & \mathbf{e}_r & \tilde{\mathbf{0}} \\ \tilde{\mathbf{0}} & \tilde{\mathbf{0}} & \text{ROI}_r^2 \mathbf{e}_r \end{bmatrix} \quad \forall \quad r = 1, 2, \dots, 20$$

541 where  $\mathbf{e}_r$  is a vector whose components are all zero except for the  $\mathcal{H}_r/0.03 + 1$  component whose  
542 value is "1.0" ( $\mathcal{H}_r$  is the ceiling height above ground).

543 **Stage-c.** Determine the DSM transformation matrices  $\mathbf{a}_{k,\ell}$  for  $\ell=1, \dots, 8$  elements – using Eq. (49)

544 The matrix  $\mathbf{a}_{k,\ell}$  transforms the  $\ell^{\text{th}}$  cantilever wall stiffness matrix into the global coordinates and  
545 adds its' contribution to the global stiffness matrix  $\tilde{\mathbf{k}}_{\Delta z}$ . The employed RC wall is slender (i.e.,  
546  $L_\ell(z) \gg B_\ell(z)$ ). Therefore, the stiffness mutuality between the lateral directions can be neglected and  
547  $\rho_{xy,n}$  and  $\rho_{yx,n}$  are set as:

$$548 \quad \left. \begin{array}{l} \text{elements in } x - z \text{ plane: } \rho_{xy,n} = 0 \\ \text{elements in } y - z \text{ plane: } \rho_{yx,n} = 0 \end{array} \right\} \quad \forall \quad n = 0, 1, \dots, 2000$$

549 The DSM transformation matrices are:

$$550 \quad \begin{array}{l} \ell = 1: \mathbf{a}_{k,1} = [\mathbf{I} \quad \mathbf{0} \quad -7.35 \mathbf{I}] \quad ; \quad \ell = 5: \mathbf{a}_{k,5} = [\mathbf{0} \quad \mathbf{I} \quad -7.35 \mathbf{I}] \\ \ell = 2: \mathbf{a}_{k,2} = [\mathbf{I} \quad \mathbf{0} \quad -7.35 \mathbf{I}] \quad ; \quad \ell = 6: \mathbf{a}_{k,6} = [\mathbf{0} \quad \mathbf{I} \quad -7.35 \mathbf{I}] \\ \ell = 3: \mathbf{a}_{k,3} = [\mathbf{I} \quad \mathbf{0} \quad \mathbf{0}] \quad ; \quad \ell = 7: \mathbf{a}_{k,7} = [\mathbf{0} \quad \mathbf{I} \quad \mathbf{0}] \\ \ell = 4: \mathbf{a}_{k,4} = [\mathbf{I} \quad \mathbf{0} \quad 7.35 \mathbf{I}] \quad ; \quad \ell = 8: \mathbf{a}_{k,8} = [\mathbf{0} \quad \mathbf{I} \quad 7.35 \mathbf{I}] \end{array}$$

551 **Stage-d.** Calculate  $\tilde{\mathbf{m}}_{\Delta z}$  using the transformation matrices  $\mathbf{a}_{m1,\ell}$  and  $\mathbf{a}_{m2,r}$  – using Eq. (42)

552 The ceiling mass is  $m_r = 196.91 \text{ ton}$  when considering its' self-load and the assumed amount of  
 553 additional load  $0.5 \text{ ton}/m^2$ . Given  $\mathbf{a}_{m1,\ell}$ ,  $\mathbf{a}_{m2,r}$ ,  $\mathbf{m}_{\Delta z,\ell}$ , and  $m_r$  the global mass matrix is calculated  
 554 using the term:

$$555 \quad \tilde{\mathbf{m}}_{\Delta z} = \sum_{\ell=1}^8 \mathbf{a}_{m1,\ell} \mathbf{m}_{\Delta z,\ell} \mathbf{a}_{m1,\ell}^T + \sum_{r=1}^{20} \mathbf{a}_{m2,r} m_r \mathbf{a}_{m2,r}^T$$

556 In this example, the components of  $\tilde{\mathbf{m}}_{\Delta z}$  equal to  $8m\Delta z = 1.62 \text{ ton}$  and at the ceilings' DOFs the  
 557 components of  $\tilde{\mathbf{m}}$  equal to  $8m\Delta z + m_r = 198.53 \text{ ton}$ . The general  $n^{\text{th}}$  inertia component of  $\tilde{\mathbf{m}}_{\Delta z}$   
 558 (associated with rotation  $u_{\theta,n}(t)$  DOF) equals  $6,017 \text{ ton}\cdot m^2$ , and at the ceilings' DOFs it equals  $253,760$   
 559  $\text{ton}\cdot m^2$ .

560 **Stage-e.** Calculate  $\tilde{\mathbf{k}}_{\Delta z}$  using the transformation matrices  $\mathbf{a}_{k,\ell}$  – using Eq. (48)

561 The global stiffness matrix is calculated using the DSM transformation:

$$562 \quad \tilde{\mathbf{k}}_{\Delta z} = \sum_{\ell=1}^8 \mathbf{a}_{k,\ell} \mathbf{k}_{\Delta z,\ell} \mathbf{a}_{k,\ell}^T$$

563 Consequently, the  $6003 \times 6003$  global stiffness matrix of the three-dimensional structure is:

$$564 \quad \tilde{\mathbf{k}}_{\Delta z} \cong \begin{bmatrix} 4.0 \mathbf{k}_{\Delta z,\ell} & \mathbf{0} & -7.35 \mathbf{k}_{\Delta z,\ell} \\ \mathbf{0} & 4.0 \mathbf{k}_{\Delta z,\ell} & 7.35 \mathbf{k}_{\Delta z,\ell} \\ -7.35 \mathbf{k}_{\Delta z,\ell} & 7.35 \mathbf{k}_{\Delta z,\ell} & 324.135 \mathbf{k}_{\Delta z,\ell} \end{bmatrix}$$

565 That concludes example 2's stage-by-stage-description.

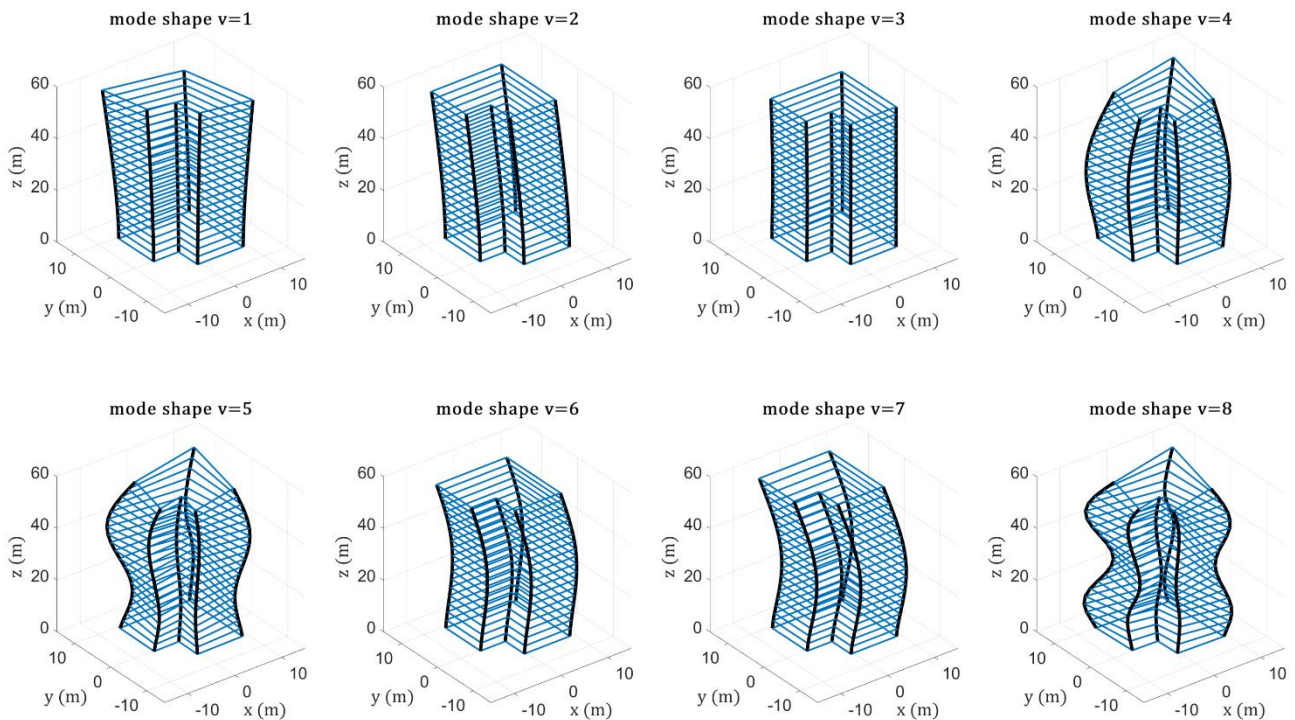
566 The modal frequencies and mode shapes of the three-dimensional structure are determined  
 567 using Eqs. (51) and (52). The 16 highest modal periods are specified in Table 2, and their respected  
 568 mode shapes are depicted in Fig. 15 (modes 1-8) and Fig. 16 (modes 9-16). The modal systems'  
 569 seismic contributions are also quantified and specified in Table 2. The seismic contribution refers to  
 570 the participation in base shear using modal static response subjected to earthquake load distribution  
 571 with additional-eccentricity of 5% of the floor-dimension perpendicular to the direction of the  
 572 seismic action (i.e.,  $\pm 0.75m$  in  $x$  and  $y$  directions).

573 The participation factors in Table 2 indicate that the modes that bend in the  $x$  and  $y$  direction  
 574 are of neglectable contribution, while those who bend diagonally, by  $45^\circ$ , are more effective. That  
 575 indication feat the building's asymmetric plan, which is of minor lateral resistance in the diagonal  
 576 direction.

577

v	modal period sec	modal participation factor (seismic analysis)	
		x-direction; eccentricity +0.75m y-direction; eccentricity -0.75m	x-direction; eccentricity +0.75m y-direction; eccentricity -0.75m
1	20.409	61.89%	61.70%
2	3.989	0.15%	0.36%
3	3.891	0.24%	0.41%
4	3.260	18.96%	18.91%
5	1.162	6.54%	6.52%
6	0.655	0.01%	0.06%
7	0.637	0.04%	0.08%
8	0.593	3.35%	3.35%
9	0.359	2.02%	2.01%
10	0.240	1.36%	1.36%
11	0.227	0.01%	0.02%
12	0.227	0.01%	0.03%
13	0.172	0.97%	0.97%
14	0.129	0.73%	0.72%
15	0.116	0.00%	0.00%
16	0.116	0.01%	0.02%
<b>Sum.</b>		<b>96.28%</b>	<b>96.52%</b>

579



580

581

**Fig. 15.** Example 2 three-dimensional structure's mode shapes v=1,2,3,4,5,6,7,8

582

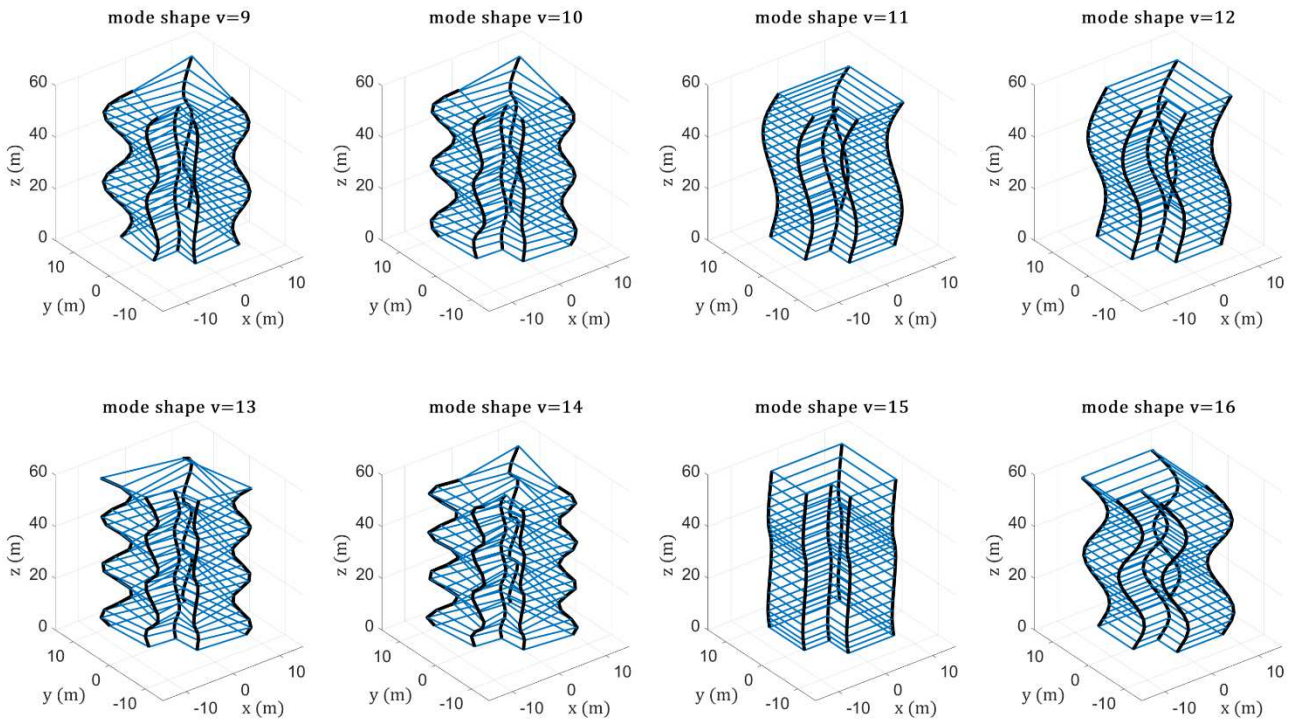


**Fig. 16.** Example 2 three-dimensional structure's mode shapes  $v=9,10,11,12,13,14,15,16$

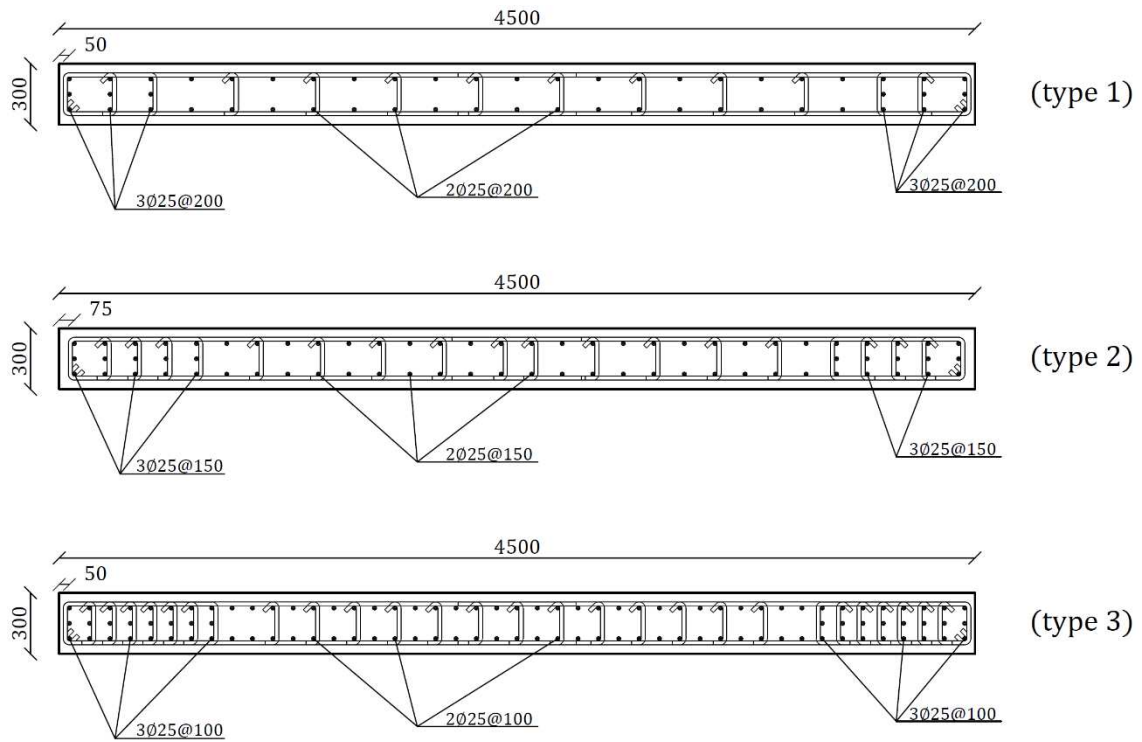
### 6.3. Example 3: inelastic two-dimensional model

The 3<sup>rd</sup> example introduces inelastic mechanical behavior to the two-dimensional cantilever wall from example 1, using the smooth hysteretic model in 4.1 and the matrix equations model developed in 4.2, and performs pushover analysis. The RC material strength properties are compressive strength of  $40.0MPa$  (say according to cube strength testing), modulus of elasticity  $28,200MPa$ , and yield strength  $16.0MPa$ . The reinforcing steel's modulus of elasticity is  $200,000MPa$ , and its' yield strength is  $400MPa$ . The stress-strain relationship of the concrete and the reinforcing steel is taken according to EC 2 [27].

The three types of RC cross-section designs, depicted in Fig. 17, are employed. Each design is provided with a different amount of steel reinforcement distribution to address the stories' varying gravitational load levels. The elastic/plastic axial force bending-moment interaction diagrams for the cross-section designs are depicted in Fig. 18 and Fig. 19. Fig. 18 refers to bending in the longitudinal (strong) direction, and Fig. 19 refers to bending in the transverse (weak) direction.

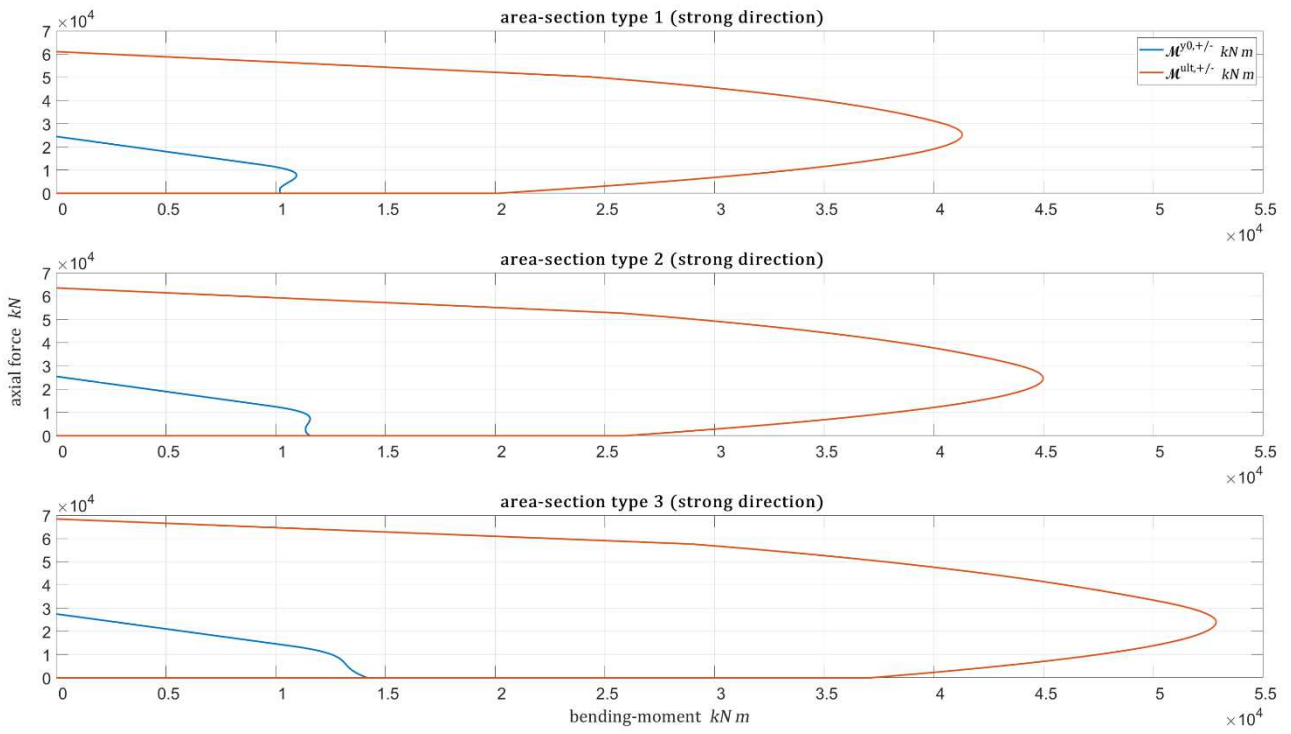
The smooth hysteretic model's parameters stem from the axial force bending-moment interaction diagrams. The gravitational load (including the ceiling's load and wall's self-weight) applied to all stories' walls is specified in Table 3. For each gravitational load quantity, the initial positive/negative yield bending-moments ( $\mathcal{M}^{y0,+}(z)$  and  $\mathcal{M}^{y0,-}(z)$ ) and the ultimate positive/negative bending-moments ( $\mathcal{M}^{ult,+}(z)$  and  $\mathcal{M}^{ult,-}(z)$ ) are determined, and the consequent

603 positive/negative ductility demand ( $\varphi^{ult,+}$  and  $\varphi^{ult,-}$ ) is defined. Table 4 shows the calculated values  
 604 in the strong direction, and Table 5 shows the calculated values in the weak direction. The other  
 605 smooth hysteretic model parameters are defined as  $\eta_1 = \eta_2 = 0.5$  (unloading stiffness equals to  $aEI$ ),  
 606  $\nu = 10$  (fast transition from elastic to the plastic range),  $\alpha = 200$  (stiffness deterioration is neglected),  
 607 and  $R_s = \infty$  (no pinching effect is regarded). Also, according to Table 6.5 in ASCE/SEI 41-06[28], the  
 608 post-yielding ratio to initial stiffness is considered  $a=0.5$ .



609  
 610

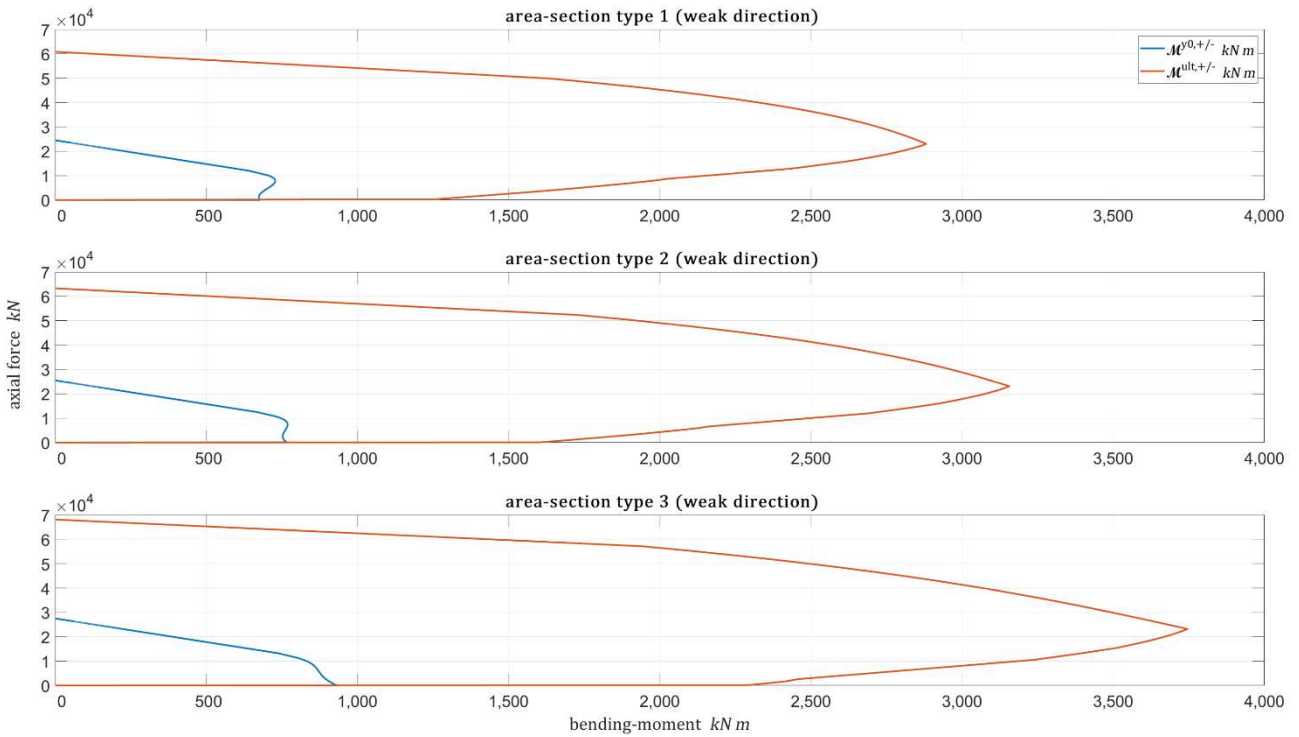
**Fig. 17.** RC cross-section designs of varying vertical steel reinforcement distribution



611  
612

**Fig. 18.** Axial force bending-moment interaction diagrams – strong direction

613



614  
615

**Fig. 19.** Axial force bending-moment interaction diagrams – weak direction

616

617 **Table 3.** The gravitational load applied to the RC walls at the bottom of each  $r^{\text{th}}$  story

r:type	Axial force applied to the walls' cross-section at the bottom of each story		
	$\ell=1,2,5,6$	$\ell=3,7$	$\ell=4,8$
	kN		
20:1	305	517	235
19:1	611	1,033	470
18:1	916	1,550	705
17:1	1,222	2,066	941
16:2	1,527	2,583	1,176
15:2	1,833	3,099	1,411
14:2	2,138	3,616	1,646
13:2	2,444	4,132	1,881
12:2	2,749	4,649	2,116
11:2	3,054	5,166	2,351
10:2	3,360	5,682	2,586
9:2	3,665	6,199	2,822
8:3	3,971	6,715	3,057
7:3	4,276	7,232	3,292
6:3	4,582	7,748	3,527
5:3	4,887	8,265	3,762
4:3	5,192	8,781	3,997
3:3	5,498	9,298	4,232
2:3	5,803	9,814	4,467
1:3	6,109	10,331	4,703

618

619 **Table 4.** RC walls' yielding bending-moment and ductility demand about the strong direction at the  
620 bottom of each  $r^{\text{th}}$  story

r:type	$\ell=1,2,5,6$		$\ell=3,7$		$\ell=4,8$	
	$\mathcal{M}_{\Delta,\ell}^{y0,+/-}$ n kN m	$\varphi_{\ell,n}^{\text{ult},+/-}$	$\mathcal{M}_{\Delta,\ell}^{y0,+/-}$ n kN m	$\varphi_{\ell,n}^{\text{ult},+/-}$	$\mathcal{M}_{\Delta,\ell}^{y0,+/-}$ n kN m	$\varphi_{\ell,n}^{\text{ult},+/-}$
20:1	10,211	3.0	10,194	3.1	10,217	3.0
19:1	10,188	3.1	10,172	3.3	10,198	3.1
18:1	10,175	3.2	10,173	3.4	10,183	3.2
17:1	10,169	3.3	10,197	3.6	10,174	3.3
16:2	11,386	3.9	11,348	4.2	11,414	3.8
15:2	11,368	4.0	11,353	4.3	11,394	3.9
14:2	11,356	4.1	11,370	4.5	11,378	4.0
13:2	11,349	4.2	11,397	4.6	11,366	4.0
12:2	11,348	4.3	11,431	4.7	11,356	4.1
11:2	11,352	4.3	11,468	4.8	11,351	4.2
10:2	11,360	4.4	11,505	4.8	11,348	4.2
9:2	11,372	4.5	11,537	4.9	11,349	4.3
8:3	13,387	5.3	13,109	5.8	13,513	5.0
7:3	13,351	5.3	13,054	5.9	13,478	5.1
6:3	13,317	5.4	12,991	6.0	13,445	5.2
5:3	13,285	5.4	12,918	6.1	13,414	5.2
4:3	13,255	5.5	12,832	6.2	13,384	5.3

3:3	13,225	5.6	12,728	6.4	13,356	5.3
2:3	13,196	5.6	12,605	6.5	13,330	5.4
1:3	13,167	5.7	12,457	6.7	13,304	5.4

621

622 **Table 5.** RC walls' yielding bending-moment and ductility demand about the weak direction at the  
623 bottom of each  $r^{\text{th}}$  story

r:type	$\ell=1,2,5,6$		$\ell=3,7$		$\ell=4,8$	
	$\mathcal{M}_{\Delta,\ell}^{y0,+/-}$	$\varphi_{\ell,n}^{\text{ult},+/-}$	$\mathcal{M}_{\Delta,\ell}^{y0,+/-}$	$\varphi_{\ell,n}^{\text{ult},+/-}$	$\mathcal{M}_{\Delta,\ell}^{y0,+/-}$	$\varphi_{\ell,n}^{\text{ult},+/-}$
	kN m		kN m		kN m	
20:1	676	2.7	675	2.8	676	2.7
19:1	674	2.8	673	3.0	675	2.8
18:1	674	2.9	674	3.1	674	2.9
17:1	673	3.0	676	3.3	674	2.9
16:2	755	3.6	753	3.9	756	3.5
15:2	754	3.7	753	4.0	755	3.6
14:2	753	3.8	755	4.2	754	3.7
13:2	753	3.9	757	4.3	753	3.7
12:2	753	4.0	759	4.4	753	3.8
11:2	753	4.0	762	4.4	753	3.9
10:2	754	4.1	764	4.5	753	3.9
9:2	755	4.2	766	4.6	753	4.0
8:3	883	4.8	867	5.6	891	4.6
7:3	881	4.9	863	5.7	889	4.6
6:3	879	5.0	860	5.9	887	4.7
5:3	877	5.0	855	6.1	885	4.7
4:3	875	5.1	849	6.3	883	4.8
3:3	874	5.2	843	6.4	881	4.9
2:3	872	5.3	835	6.6	880	4.9
1:3	870	5.4	825	6.8	878	5.0

624

625 Matrix structural analysis is performed and applies an incremental load to RC wall  $\ell=4$ . The  
626 mass and stiffness matrices, in bending coordinates, of wall  $\ell=4$  are determined according to the  
627 stage-by-stage-description below.

628 **Stage-a.** Define the integration matrices  $\mathbf{T}_{z \in [0 \rightarrow H_{\ell=4}]}^{\int dz}$  and  $\mathbf{T}_{z \in [H_{\ell=4} \rightarrow 0]}^{\int dz}$  – using Eq. (20)

629 Repeats *Stage-a* in Example 1 (same as the linearly-elastic two-dimensional wall).

630 **Stage-b.** Calculate the bending-curvature-related-mass matrix  $\mathbf{m}_{\Delta z,4}$  – using Eq. (72)

631 The mass matrix of the two-dimensional wall is  $\mathbf{m}_{\Delta z,4} = 3.375 \mathbf{I} \frac{\text{ton}}{\text{m}}$ , and the bending-curvature-  
632 related-mass matrix  $\mathbf{m}_{\Delta z,4}$  is:

633 
$$\mathbf{m}_{\Delta z,4} = \mathbf{T}_{z \in [H_{\ell=4} \rightarrow 0]}^{\int dz} \mathbf{T}_{z \in [H_{\ell=4} \rightarrow 0]}^{\int dz} \mathbf{m}_{\Delta z,\ell} \mathbf{T}_{z \in [0 \rightarrow H_{\ell=4}]}^{\int dz} \mathbf{T}_{z \in [0 \rightarrow H_{\ell=4}]}^{\int dz} \leftrightarrow \mathcal{M}_{\Delta z,4}^{\text{I}}(t) = \mathbf{m}_{\Delta z,4} \dot{\Phi}_{\Delta z,4}(t)$$

634 *Stage-c. Define the bending-stiffness matrix components' term – see 4.1Eq. (71)*

635 The smooth hysteretic model parameters are specified above. Since no pinching-effect is regarded,  
636 the hysteretic bending-stiffness is:

$$637 \quad \kappa_4(z, \varphi_4, \dot{\varphi}_4) = 3.212 \cdot 10^7 + \kappa_4^*(z, \mathcal{M}_4^{R*}, \dot{\varphi}_4)$$

638 and the hysteretic portion is formulated as:

$$639 \quad \kappa^*(z, \mathcal{M}_4^{R*}, \dot{\varphi}_4) = \dots$$

$$640 \quad \left( \frac{(|\mathcal{M}_4^R(z,t)| + 200 \mathcal{M}_4^{yld}(z))}{(|6.424 \cdot 10^7 \varphi_4(z,t)| + 200 \mathcal{M}_4^{yld}(z))} - 0.5 \right) 6.424 \cdot 10^7 \left| \frac{\mathcal{M}_4^{R*}(z,t)}{\mathcal{M}_4^{yld*}(z)} \right|^{100} \left[ 0.5 \operatorname{sgn}(\mathcal{M}_4^{R*}(z,t) \dot{\varphi}_4(z,t)) + 0.5 \right]$$

641 The hysteretic bending-stiffness terms at the  $z = 0, \Delta z, \dots, N$  levels are the components of the  
642 2001×2001 diagonal bending-stiffness matrix:

$$643 \quad \mathbf{\kappa}_{\Delta z,4}(\boldsymbol{\varphi}_{\Delta z,4}, \dot{\boldsymbol{\varphi}}_{\Delta z,4}) = 0.03 \begin{bmatrix} \kappa(0, \varphi_4, \dot{\varphi}_4) & & & \\ & \ddots & & \\ & & \kappa(0.03n, \varphi_4, \dot{\varphi}_4) & \\ & & & \ddots \\ & & & & \kappa(60, \varphi_4, \dot{\varphi}_4) \end{bmatrix}$$

644 At this point, the mass and stiffness matrices in bending-coordinates are determined, and the RC  
645 wall is ready to undergo matrix structural analysis.

646 The applied uniform load is linearly increasing to the level of  $p_{max} = 24.50 \text{ kN/m}$  to meet  
647 the wall's ultimate bending-moment  $\mathcal{M}_4^{ult,+}(0) = 44,109 \text{ kNm}$ . The force duration is defined as 100s,  
648 and the analysis is of 0.01s time increments to simulate a quasi-static loading case:

$$649 \quad \mathbf{M}_{\Delta z,4}^p(t) = 24.50 \frac{i \cdot 0.01}{100} \mathbf{T}_{z \in [H_4 \rightarrow 0]}^{f \, dz} \mathbf{T}_{z \in [H_4 \rightarrow 0]}^{f \, dz} \mathbf{1} \quad \forall \quad i = 0, 1, 2, \dots, 10,000$$

650 The analysis is performed for three cases of strength degradation: (i) no strength degradation, (ii)  
651  $\beta_1 = 0.5$  and  $\beta_2 = 0$ , and (iii)  $\beta_1 = 0.5$  and  $\beta_2 = 0.25$ . The relationship between the wall's base  
652 bending-moment  $\mathcal{M}_{\Delta z,4_1}^R(t)$  and the normalized bending-curvature  $\varphi_{\Delta z,4_1}(t)/\varphi_4^{ult,+}(0)$  is depicted in  
653 Fig. 20. The variation of the yield bending-moment in time  $\mathcal{M}_{\Delta z,4_1}^{yld,+}(t)$  is also depicted. All plots  
654 indicate  $\mathcal{M}_{\Delta z,4_1}^R(t)$  enters the plastic state exactly when it meets with  $\mathcal{M}_{\Delta z,4_1}^{yld,+}(t)$ , and in simulations  
655 (ii) and (iii), when strength degradation is considered,  $\mathcal{M}_{\Delta z,4_1}^{yld,+}(t)$  equals zero (no strength left)  
656 precisely when the normalized bending-curvature equals 1.0 – demonstrating the model's integrity.

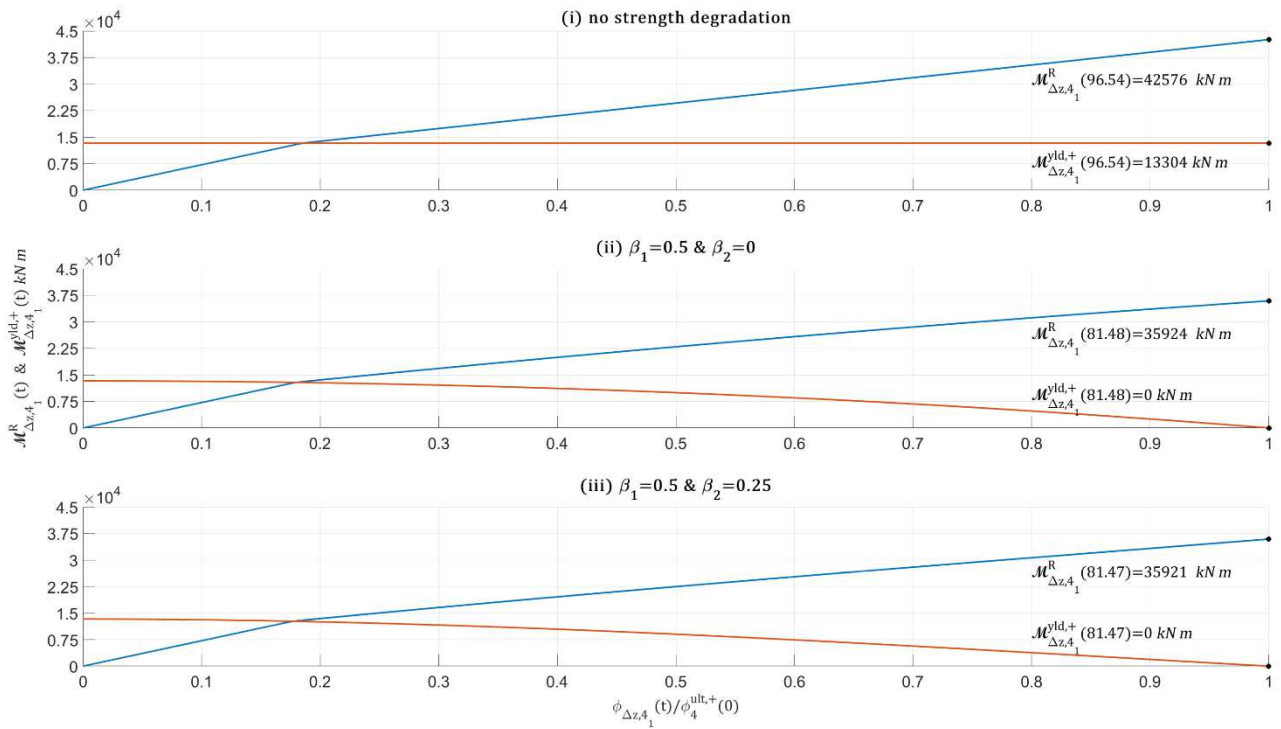


**Fig. 20.** Wall  $\ell=4$  base bending-moment and yielding bending-moment versus normalized bending-curvature

657  
658  
659

660

661 **6.4. Example 4 inelastic three-dimensional**

662 The following example analyzes the three-dimensional structure in example 2 and employs the wall  
663 cross-section designs and smooth hysteretic model properties defined in example 3. The following  
664 seven stages are initiated for obtaining the global mass matrix and global stiffness matrix in bending-  
665 coordinates.

666 **Stage-a.** Determine the transformation matrices  $\mathbf{a}_{m1,\ell}$  for the  $\ell=1,\dots,8$  elements – using Eq. (43)

667 Repeats Stage-a in Example 2.

668 **Stage-b.** Determine the transformation matrices  $\mathbf{a}_{m2,r}$  for the  $r=1,\dots,20$  ceilings – using Eq. (44)

669 Repeats Stage-b in Example 2.

670 **Stage-c.** Determine the DSM transformation matrices  $\mathbf{a}_{k,\ell}$  for  $\ell=1,\dots,8$  elements – using Eq. (49)

671 Repeats Stage-c in Example 2.

672 **Stage-d.** Determine the transformation matrix  $\mathbf{T}_{f \rightarrow \mathcal{M}}$  – using Eq. (74)

673 The 2001×2001 LRS integration matrices are of the form:



692

$$\tilde{\mathbf{\kappa}}_{\Delta z}(\mathbf{\kappa}_{\Delta z, \ell=1, \dots, 8}) = \sum_{\ell=1}^8 (\mathbf{a}_{k, \ell} \mathbf{\kappa}_{\Delta z, \ell}(\boldsymbol{\varphi}_{\Delta z, \ell}, \boldsymbol{\psi}_{\Delta z, \ell}) \mathbf{a}_{k, \ell}^T)$$

693 That ends the stage-by-stage description.

694

695

696

697

698

699

700

701

702

The inelastic three-dimensional structure's earthquake response is now analyzed for the strong Valparaiso earthquake (Chile 2017). The processed ground acceleration sequence recorded by Torpederas station is chosen, and its' horizontal components in the E-W and N-S directions are depicted in Fig. 21. The E-W component is applied in the  $x$ -direction, and the N-S component is applied in the  $y$ -direction. The global inherent-damping matrix in bending-coordinates is calculated using Eq. (79) with a damping ratio of  $\zeta = 1\%$  assigned to all modes. The Newmark- $\beta$  of average acceleration method is utilized for evaluating the dynamic response of the structure, and the hysteretic bending-moment vector  $\tilde{\mathbf{M}}_{\Delta z}^H(t)$  is addressed implicitly using the Newton-Raphson iteration method.

703

704

705

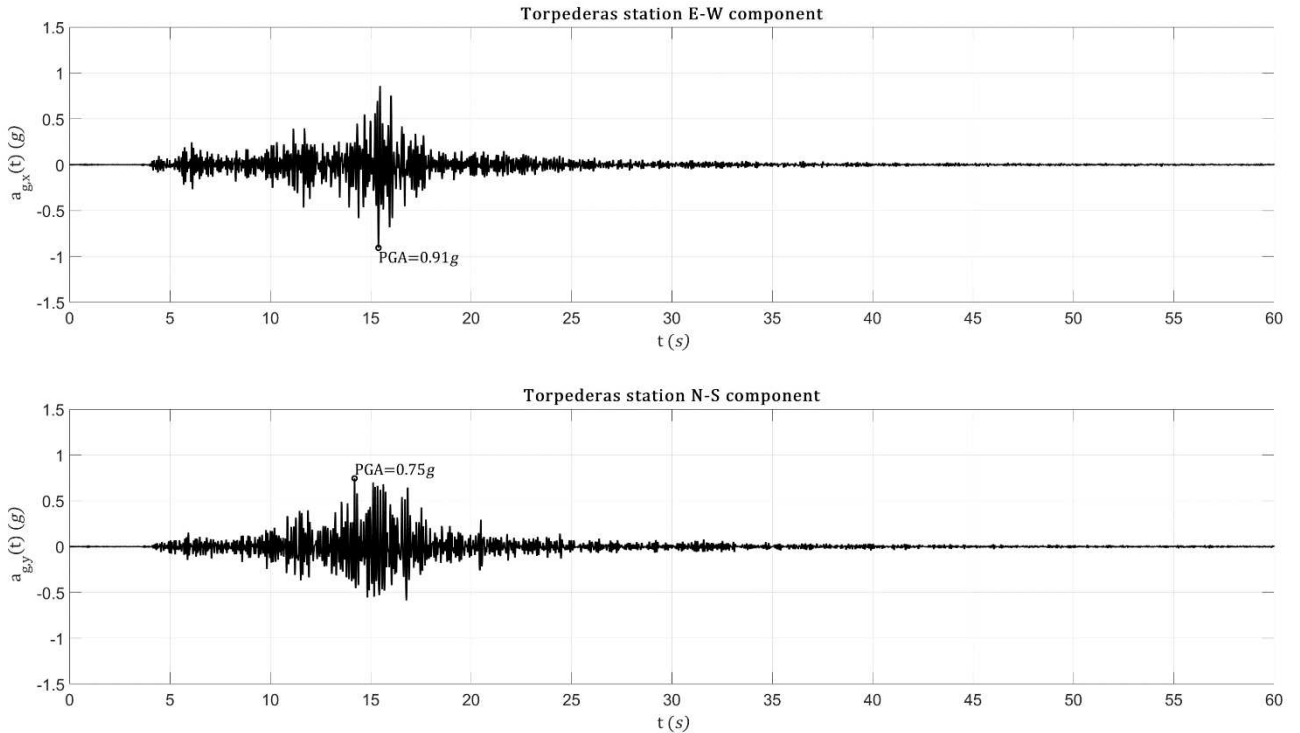
706

707

708

709

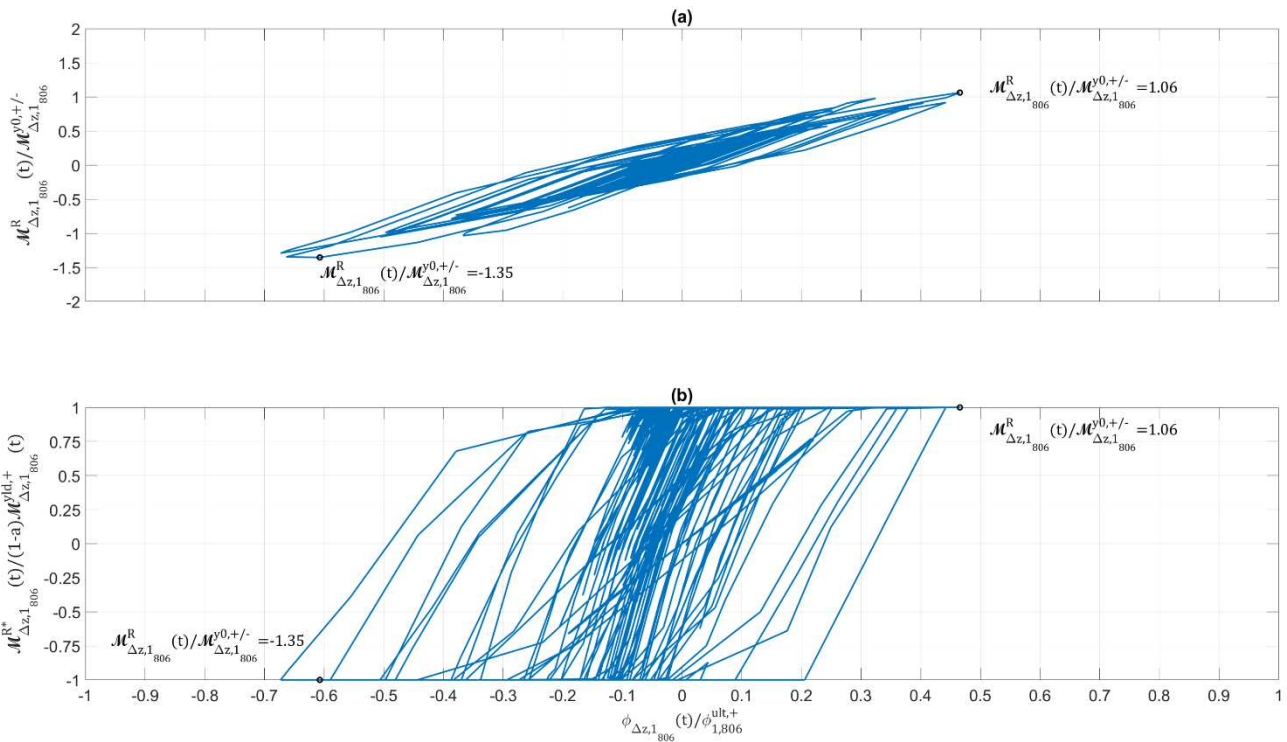
The matrix structural analysis indicates that RC wall  $\ell=1$  is the closest to its' ultimate curvature at  $z=48.3m$  (i.e., DOF  $n=806$ ), where it reached 70% of ductility demand. Fig. 22 depicts the corresponding area sections' cyclic behavior and the cyclic hysteretic portion at  $z=48.3m$ . Fig. 23 illustrates the time-variation of the normalized bending-moment and degradation yielding bending-moment. Fig. 24 shows the roof displacements in the  $x$  and  $y$  directions, and Fig. 25 illustrates the deformation of the whole structure when the roof displacements, in  $x$  and  $y$  directions, are at their maximum.



710

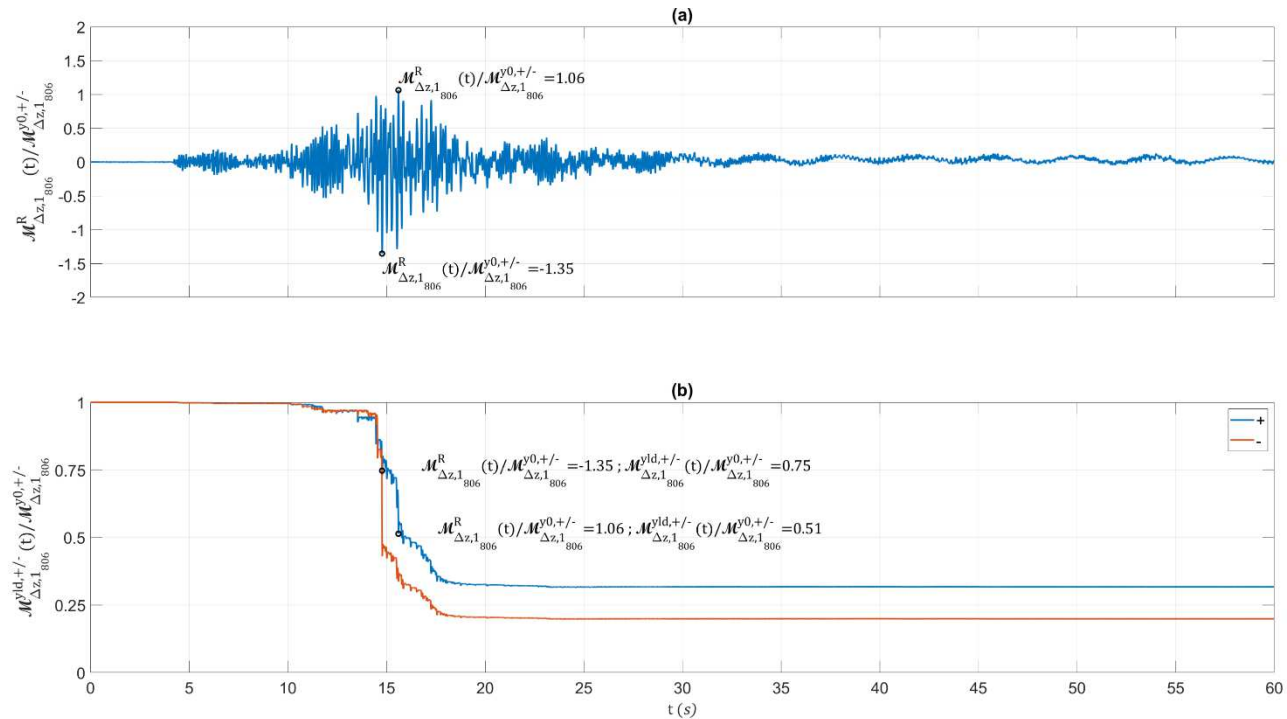
711

Fig. 21. Valparaiso earthquake (Chile 2017) ground acceleration records



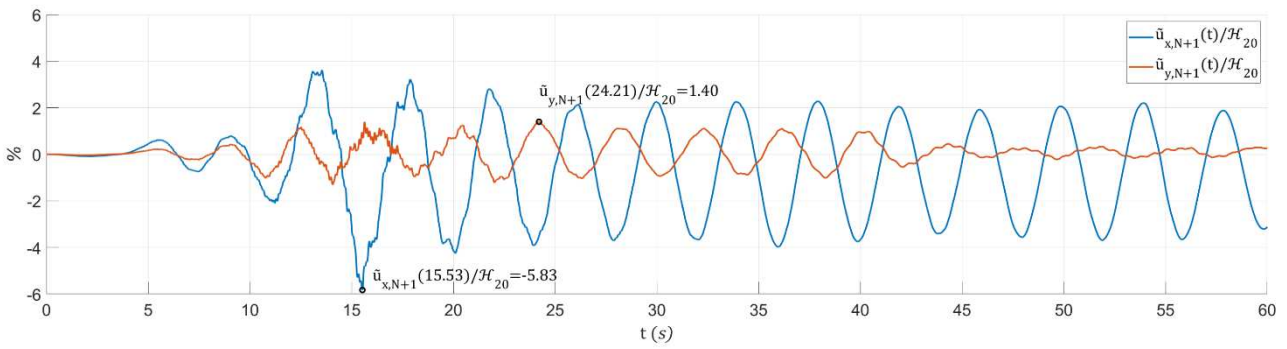
**Fig. 22.** Wall  $\ell=1$  cross-section at  $z=48.3m$   $n=806$ : (a) normalized bending-moment cyclic earthquake response, (b) normalized hysteretic portion of bending-moment

712  
713  
714  
715



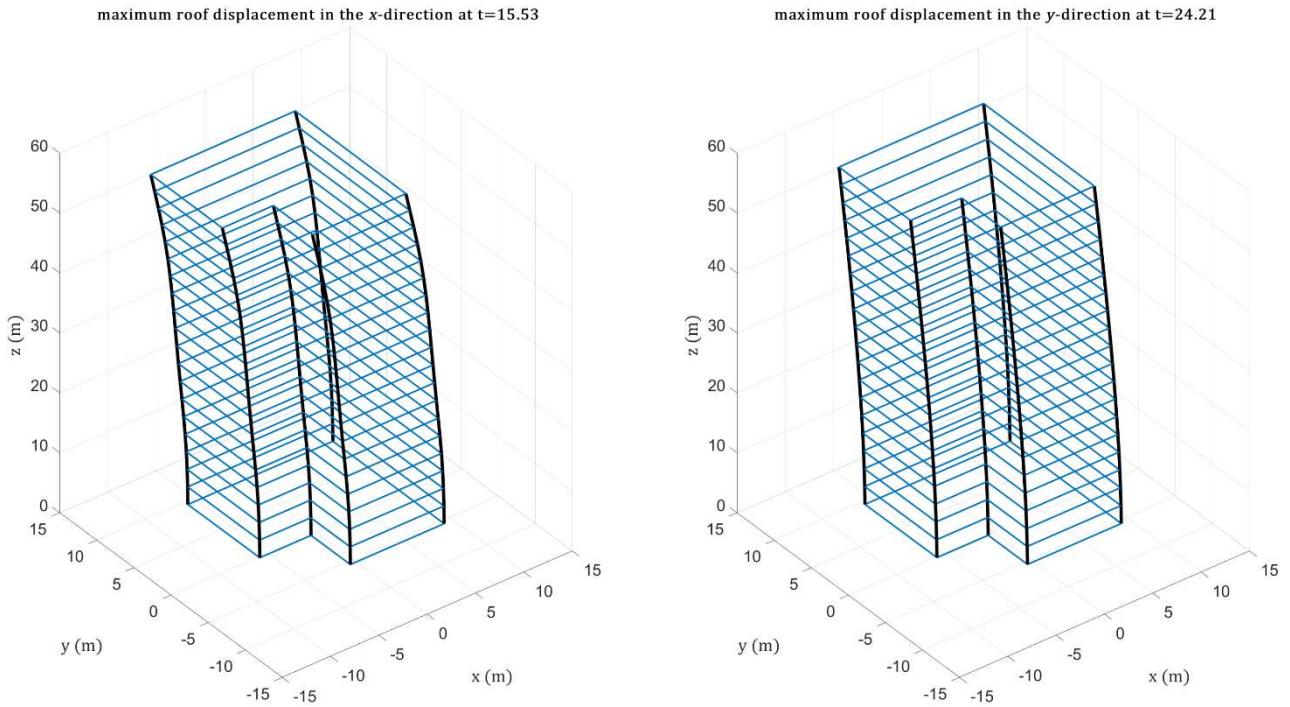
**Fig. 23.** Wall  $\ell=1$  cross-section at  $z=48.3m$   $n=806$ : (a) normalized bending-moment in time, (b) normalized yielding bending-moment quantity in time

716  
717  
718  
719



720  
721

**Fig. 24. Relative roof displacement in the  $x$  and  $y$  directions**



722  
723

**Fig. 25. Structural deformation at maximum roof displacements**

724 **7. Conclusions**

725 The paper develops a novel matrix equations model for the dynamic analysis of two-  
 726 dimensional and three-dimensional RC buildings with cantilever elements lateral load resisting  
 727 system that can be introduced to control engineering and structural dynamics' equation-of-motion.  
 728 The development starts with discretizing the PDE governing the dynamic equilibrium of a cantilever  
 729 element subjected to lateral load while introducing the Euler-Bernoulli assumption. The  
 730 displacement-related stiffness matrix is evaluated using The LRS numerical integration – catering to  
 731 the structure's boundary conditions. The mesh-size efficiency examination demonstrates the high  
 732 numerical precision the stiffness matrix provides.

733 The three-dimensional structure's matrix equations employ the elements' stiffness matrices  
 734 and combine them into the global stiffness matrix using the DSM method. The elements' mass  
 735 matrices and the ceilings' mass quantities are combined into the global mass matrix using the

736 defined transformation matrices. The matrix equations model considers the element's lateral  
737 resistance in both directions and the element's stiffness mutuality from the  $x$ -direction to the  $y$ -  
738 direction and vice-versa.

739 The nonlinear RC mechanical behavior is addressed using a smooth hysteretic model whose  
740 parameters refer to an RC wall cross-section subjected to gravitational load and bending-moment  
741 simultaneously. In the nonlinear analysis case, the matrix equations model refers to the bending-  
742 moment equilibrium. The LRS integration transformation matrix is now used to define the mass  
743 matrix in bending-coordinates while the bending-stiffness matrix is diagonal. Working in bending-  
744 coordinates exempts matrix inversion – saving computational efforts.

745 The paper presents four examples for utilizing the developed matrix equations models. Each  
746 example provides a stage-by-stage description for defining the stiffness and mass matrices. In  
747 examples 1 and 2, two-dimensional and three-dimensional structures, respectively, of linearly-  
748 elastic properties are addressed, and their mode shapes are illustrated. The 3<sup>rd</sup> example addresses  
749 an inelastic cantilever element and performs pushover analysis. The 4<sup>th</sup> and last example deals with  
750 modeling a three-dimensional inelastic structure and performs earthquake analysis. The four  
751 examples demonstrate the practicability of the developed matrix equations models, which offer an  
752 idealized approach for performing dynamic structural analysis.

#### 753 *Compliance with ethical standards*

754 The author declare that there is no conflict of interest regarding the publication of this paper

#### 755 *Data availability statement*

756 Data will be made available on reasonable request to the author

757

758 8. *References*

- 759 1. Wong, K.K.F., Wang, Y.: Energy-based design of structures using modified force analogy  
760 method. *Struct. Des. Tall Spec. Build.* 12, 393–407 (2003). <https://doi.org/10.1002/tal.234>
- 761 2. Li, G., Li, H.N.: Seismic response analysis of structure with energy dissipation devices using  
762 force analogy method. *Struct. Des. Tall Spec. Build.* 20, 291–313 (2011).  
763 <https://doi.org/10.1002/tal.541>
- 764 3. Sun, B., Gu, Q., Zhang, P., Ou, J.: A practical numerical substructure method for seismic  
765 nonlinear analysis of tall building structures. *Struct. Des. Tall Spec. Build.* 26, e1377 (2017).  
766 <https://doi.org/10.1002/tal.1377>
- 767 4. Chang, T.L., Lee, C.L., Carr, A.J., Dhakal, R.P.: Numerical evaluations of a novel membrane  
768 element in response history analysis of reinforced concrete shear walls. *Eng. Struct.* 220, 110760  
769 (2020). <https://doi.org/10.1016/j.engstruct.2020.110760>
- 770 5. Pozo, F., Acho, L., Rodríguez, A., Pujol, G.: Nonlinear modeling of hysteretic systems with  
771 double hysteretic loops using position and acceleration information. *Nonlinear Dyn.* 57, 1–12  
772 (2009). <https://doi.org/10.1007/s11071-008-9414-7>
- 773 6. Liu, C., Yu, K.: Accurate modeling and analysis of a typical nonlinear vibration isolator with  
774 quasi-zero stiffness. *Nonlinear Dyn.* 100, 2141–2165 (2020). [https://doi.org/10.1007/s11071-020-](https://doi.org/10.1007/s11071-020-05642-2)  
775 [05642-2](https://doi.org/10.1007/s11071-020-05642-2)
- 776 7. Fragiadakis, M., Papadrakakis, M.: Modeling, analysis and reliability of seismically excited  
777 structures: Computational issues. *Int. J. Comput. Methods.* 5, 483–511 (2008).  
778 <https://doi.org/10.1142/S0219876208001674s>
- 779 8. Younesian, D., Hosseinkhani, A., Askari, H., Esmailzadeh, E.: Elastic and viscoelastic  
780 foundations: a review on linear and nonlinear vibration modeling and applications. *Nonlinear*  
781 *Dyn.* 97, 853–895 (2019). <https://doi.org/10.1007/s11071-019-04977-9>
- 782 9. Mata, P., Barbat, A.H., Oller, S., Boroschek, R.: Constitutive and geometric nonlinear models for  
783 the seismic analysis of RC structures with energy dissipators. *Arch. Comput. Methods Eng.* 15,  
784 489–539 (2008). <https://doi.org/10.1007/s11831-008-9024-z>
- 785 10. Castaldo, P., Gino, D., Bertagnoli, G., Mancini, G.: Resistance model uncertainty in non-linear  
786 finite element analyses of cyclically loaded reinforced concrete systems. *Eng. Struct.* 211, 110496  
787 (2020). <https://doi.org/10.1016/j.engstruct.2020.110496>
- 788 11. Gino, D., Castaldo, P., Giordano, L., Mancini, G.: Model uncertainty in non-linear numerical  
789 analyses of slender reinforced concrete members. *Struct. Concr.* (2021).  
790 <https://doi.org/10.1002/suco.202000600>
- 791 12. Ismail, M., Ikhouane, F., Rodellar, J.: The hysteresis Bouc-Wen model, a survey. *Arch. Comput.*  
792 *Methods Eng.* 16, 161–188 (2009). <https://doi.org/10.1007/s11831-009-9031-8>
- 793 13. Sivaselvan, M. V, Reinhorn, A.M.: Hysteretic models for deteriorating inelastic structures. *J. Eng.*  
794 *Mech.* 126, 633–640 (2000)
- 795 14. Wang, C., Foliente, G.C., Sivaselvan, M. V., Reinhorn, A.M.: Hysteretic Models for Deteriorating  
796 Inelastic Structures. *J. Eng. Mech.* 127, 1200–1202 (2001). [https://doi.org/10.1061/\(asce\)0733-](https://doi.org/10.1061/(asce)0733-9399(2001)127:11(1200))  
797 [9399\(2001\)127:11\(1200\)](https://doi.org/10.1061/(asce)0733-9399(2001)127:11(1200))
- 798 15. Charalampakis, A.E., Koumoussis, V.K.: On the response and dissipated energy of Bouc–Wen  
799 hysteretic model. *J. Sound Vib.* 309, 887–895 (2008)

- 800 16. Charalampakis, A.E.: The response and dissipated energy of Bouc–Wen hysteretic model  
801 revisited. *Arch. Appl. Mech.* 85, 1209–1223 (2015). <https://doi.org/10.1007/s00419-014-0937-8>
- 802 17. Lian, M., Guan, B., Cheng, Q., Zhang, H., Su, M.: Experimental and numerical study of seismic  
803 performance of high-strength steel fabricated framed-tube structures with replaceable shear  
804 links. *Structures*. 28, 2714–2732 (2020). <https://doi.org/10.1016/j.istruc.2020.10.081>
- 805 18. Roh, H., Reinhorn, A.M.: Hysteretic behavior of precast segmental bridge piers with superelastic  
806 shape memory alloy bars. *Eng. Struct.* 32, 3394–3403 (2010).  
807 <https://doi.org/10.1016/j.engstruct.2010.07.013>
- 808 19. Foliente, G.C.: Hysteresis Modeling of Wood Joints and Structural Systems. *J. Struct. Eng.* 121,  
809 1013–1022 (1995). [https://doi.org/10.1061/\(asce\)0733-9445\(1995\)121:6\(1013\)](https://doi.org/10.1061/(asce)0733-9445(1995)121:6(1013))
- 810 20. Oldfield, M., Ouyang, H., Mottershead, J.E.: Simplified models of bolted joints under harmonic  
811 loading. *Comput. Struct.* 84, 25–33 (2005). <https://doi.org/10.1016/j.compstruc.2005.09.007>
- 812 21. Wang, C.-H., Wen, Y.-K.: Evaluation of pre-Northridge low-rise steel buildings. I: Modeling. *J.*  
813 *Struct. Eng.* 126, 1160–1168 (2000)
- 814 22. Ni, Y.Q., Ko, J.M., Wong, C.W.: Identification of non-linear hysteretic isolators from periodic  
815 vibration tests. *J. Sound Vib.* 217, 737–756 (1998). <https://doi.org/10.1006/jsvi.1998.1804>
- 816 23. Basili, M., De Angelis, M.: Optimal passive control of adjacent structures interconnected with  
817 nonlinear hysteretic devices. *J. Sound Vib.* 301, 106–125 (2007).  
818 <https://doi.org/10.1016/j.jsv.2006.09.027>
- 819 24. Panyakapo, P.: Cyclic Pushover Analysis procedure to estimate seismic demands for buildings.  
820 *Eng. Struct.* 66, 10–23 (2014). <https://doi.org/10.1016/j.engstruct.2014.02.001>
- 821 25. Zareian, F., Krawinkler, H., Ibarra, L., Lignos, D.: Basic concepts and performance measures in  
822 prediction of collapse of buildings under earthquake ground motions. *Struct. Des. Tall Spec.*  
823 *Build.* 19, 167–181 (2010). <https://doi.org/10.1002/tal.546>
- 824 26. Xiao, Y., Zeng, L., Chen, Y., Du, G., Zhang, J., Chen, J.: Seismic fragility analysis of concrete  
825 encased frame-reinforced concrete core tube hybrid structure based on quasi-static cyclic test.  
826 *Struct. Des. Tall Spec. Build.* 28, e1665 (2019). <https://doi.org/10.1002/tal.1665>
- 827 27. EN 1992-1-1 Eurocode 2: design of concrete structures – Part 1–1: General rules and rules for  
828 buildings; 2004.
- 829 28. ASCE. Seismic rehabilitation of existing buildings, American Society of Civil Engineers; 2007.  
830 <https://doi.org/10.1061/9780784408841>.

# Figures

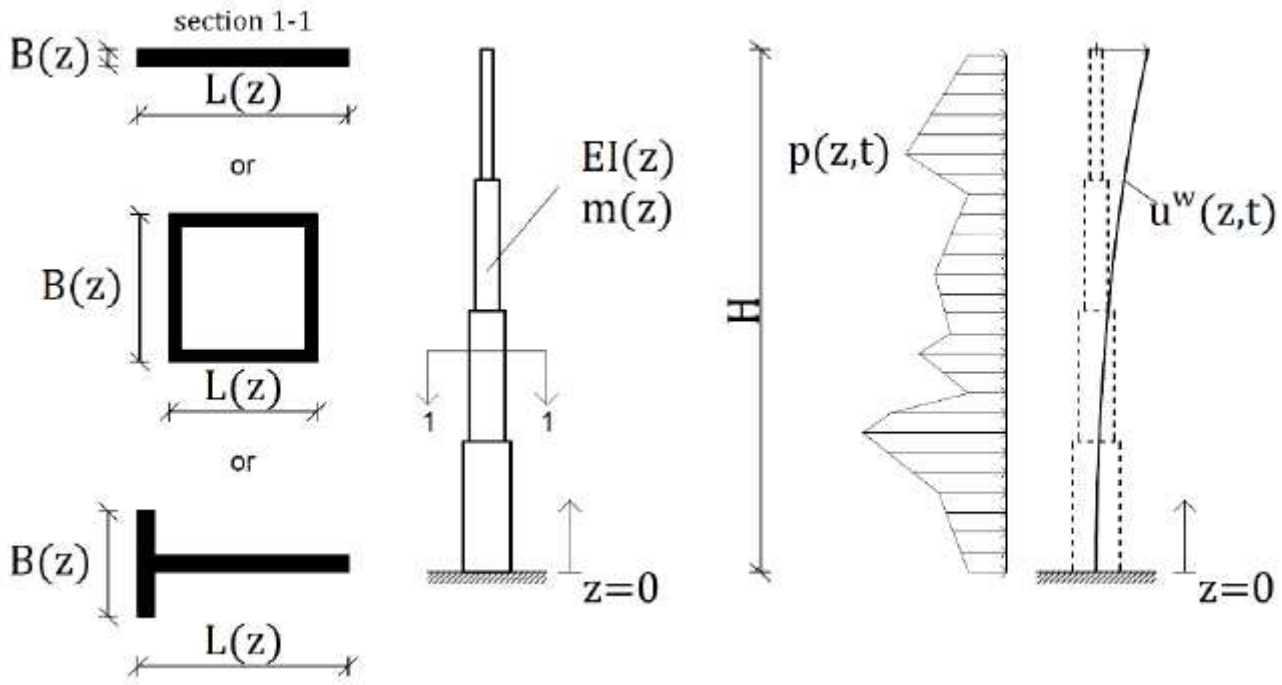


Figure 1

Cantilever element of distributed mass and elasticity

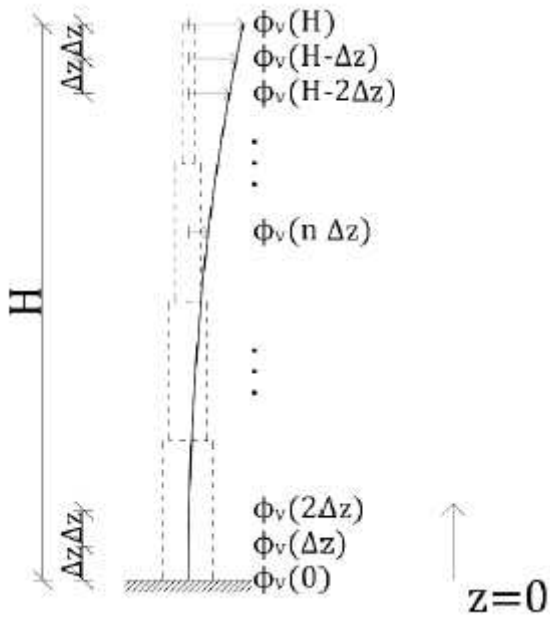


Figure 2

discretized cantilever element scheme

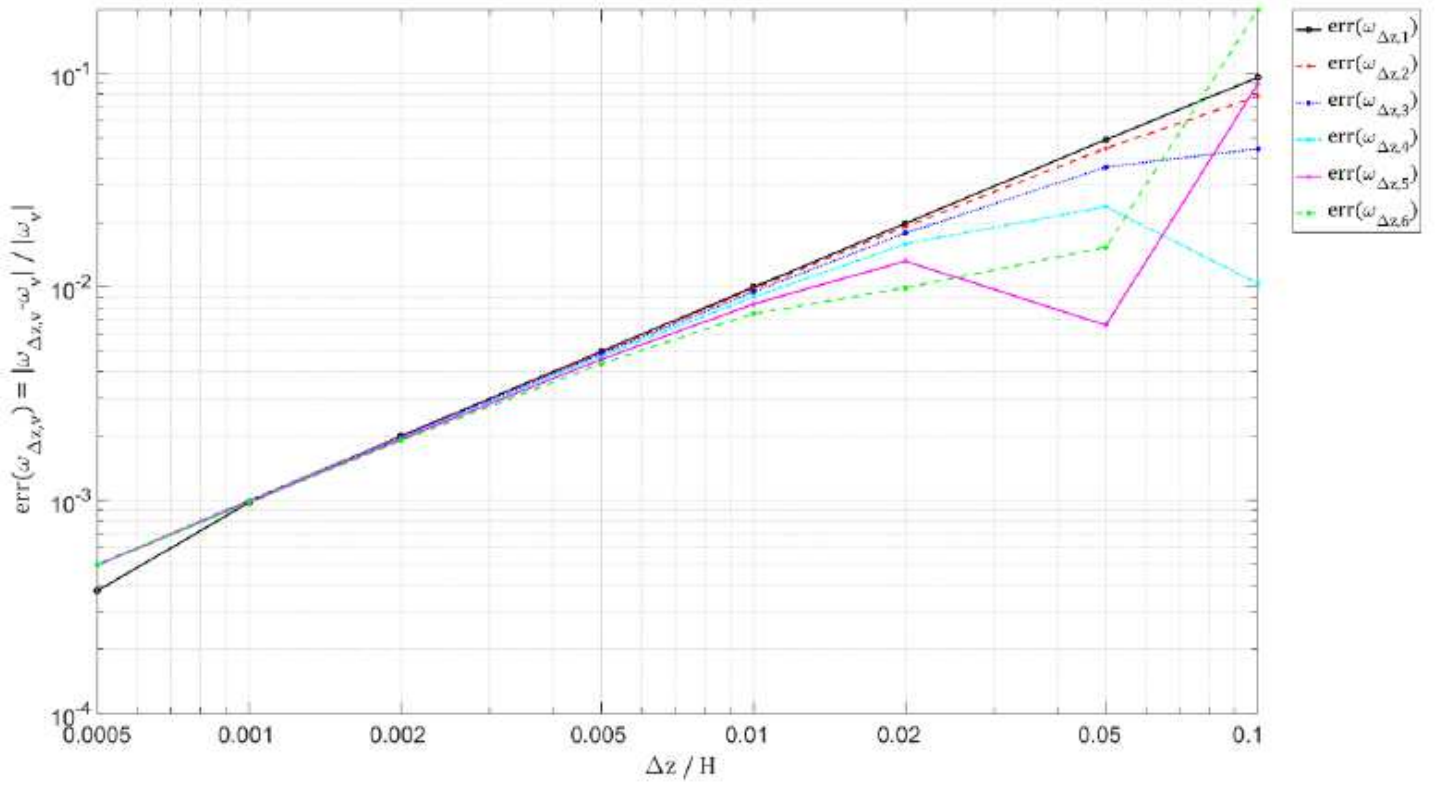


Figure 3

The relative error of the modal angular frequency approximation

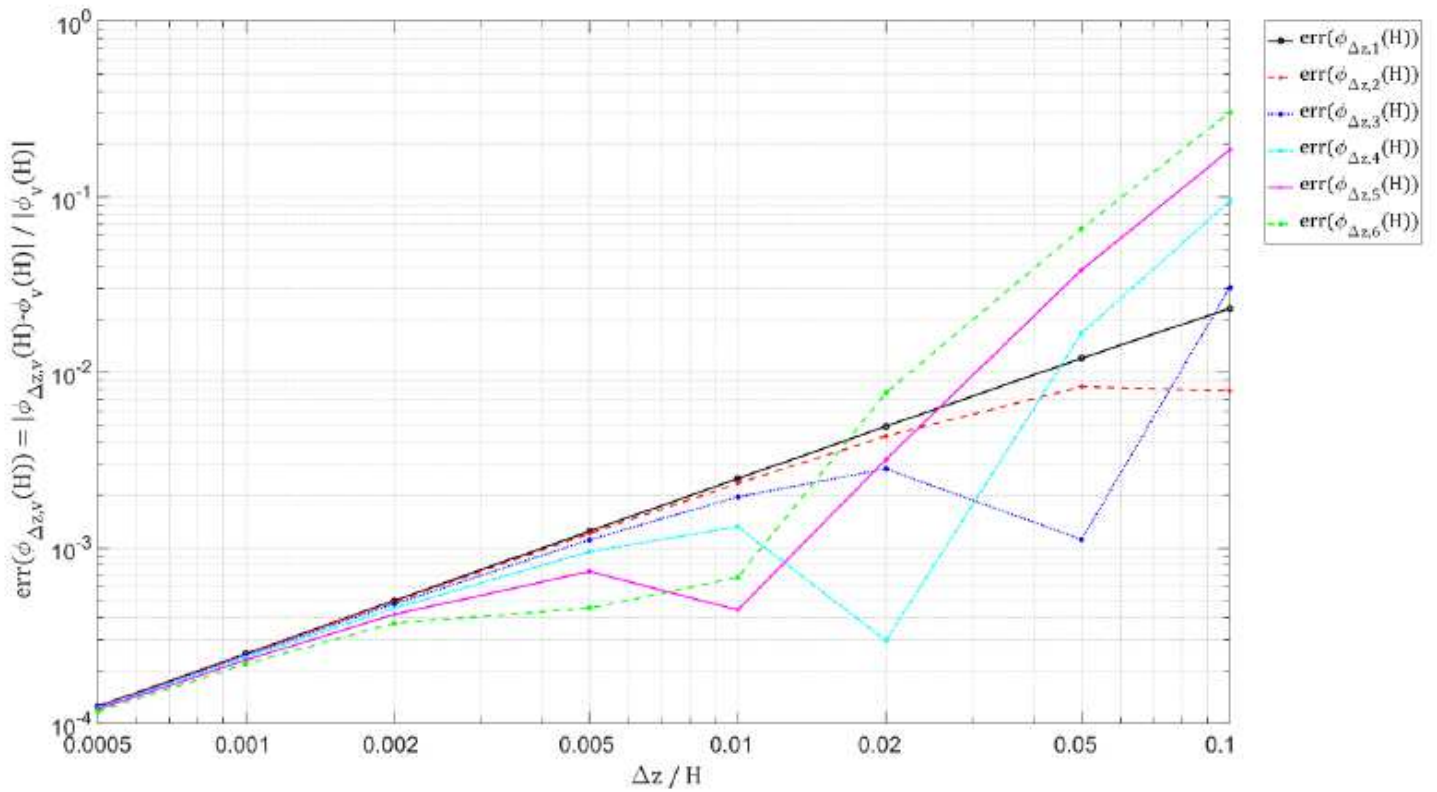


Figure 4

The relative error of the modal roof displacement approximation

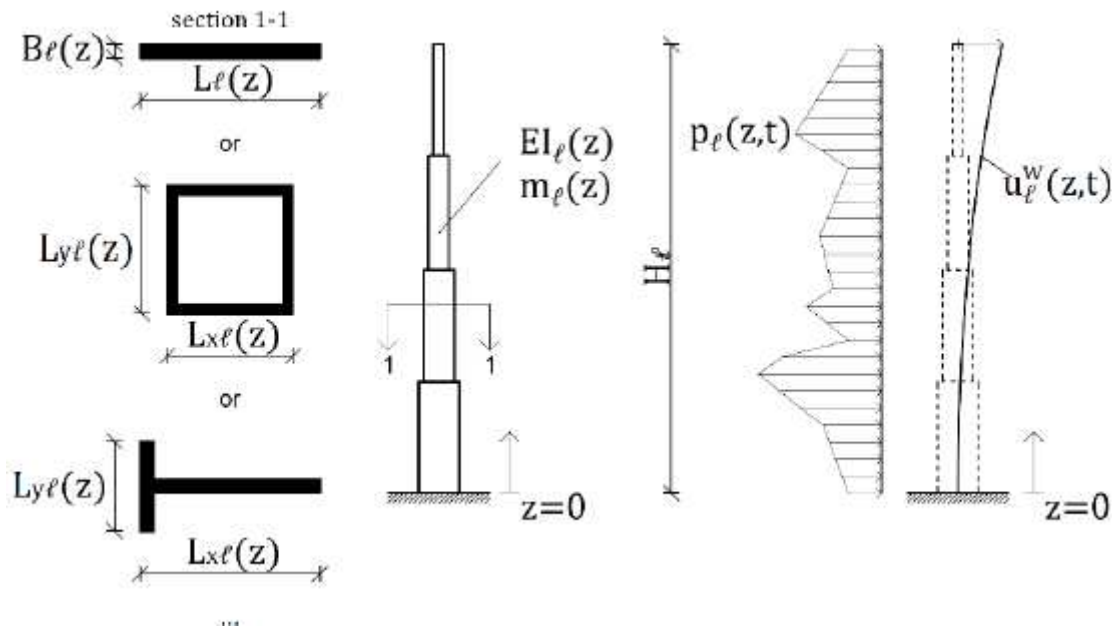


Figure 5

The  $\ell$ th element of distributed mass and elasticity

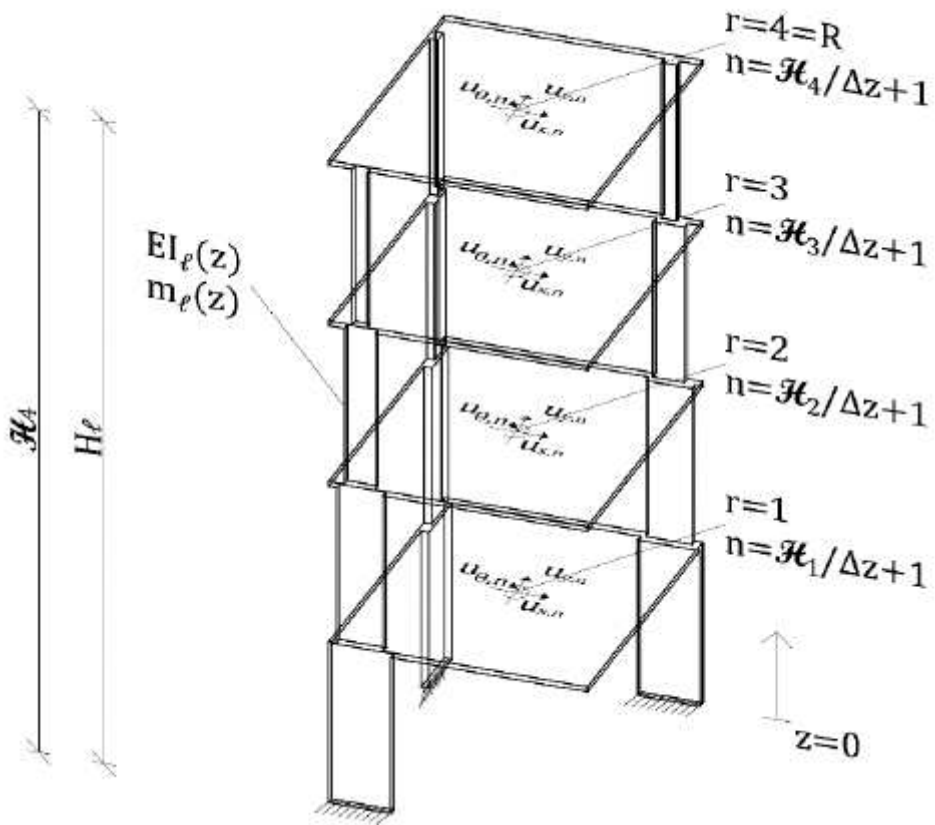


Figure 6

Three-dimensional structure with cantilever elements illustration

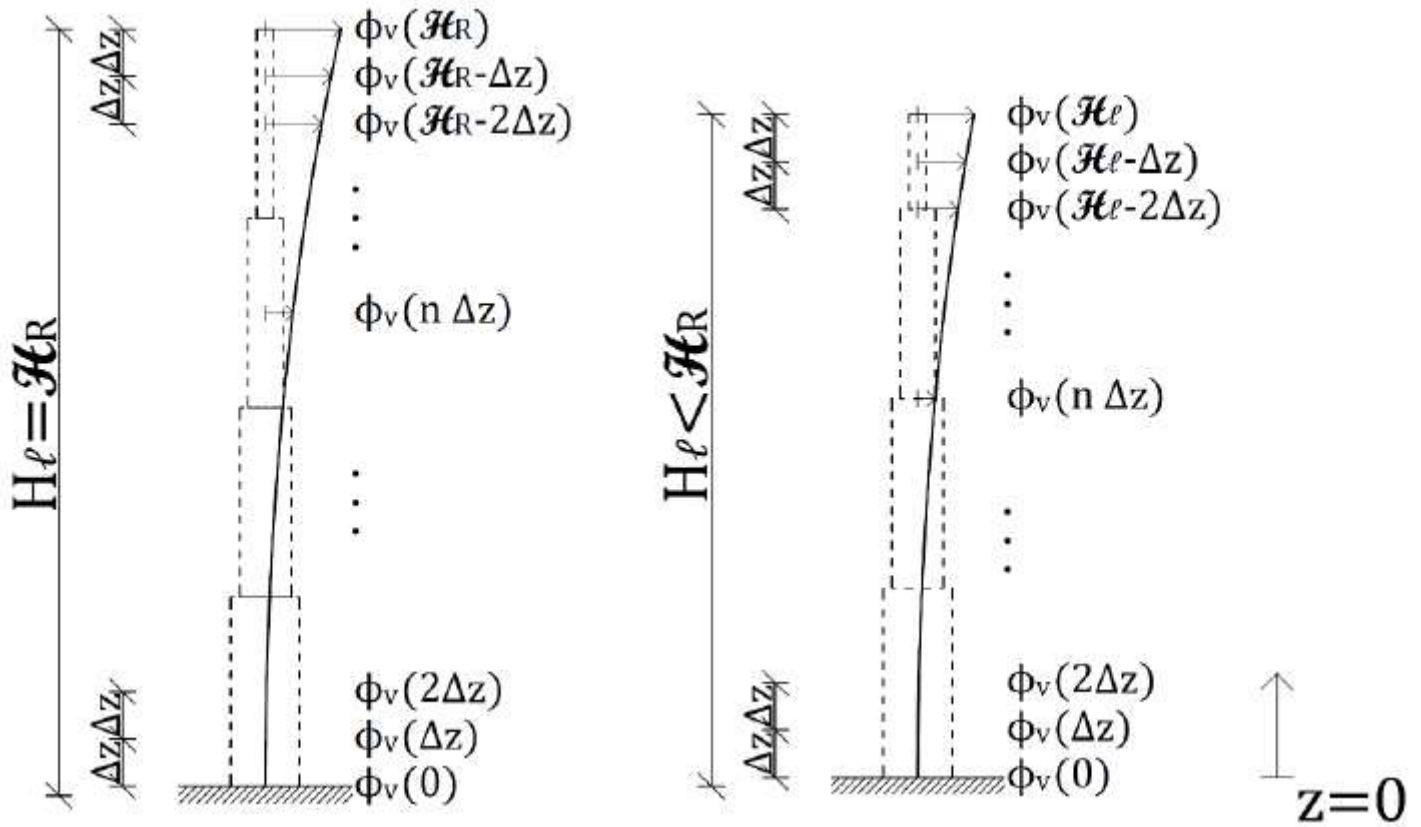


Figure 7

Element's DOFs for  $z=0$  (left) and  $z < 0$  (right)

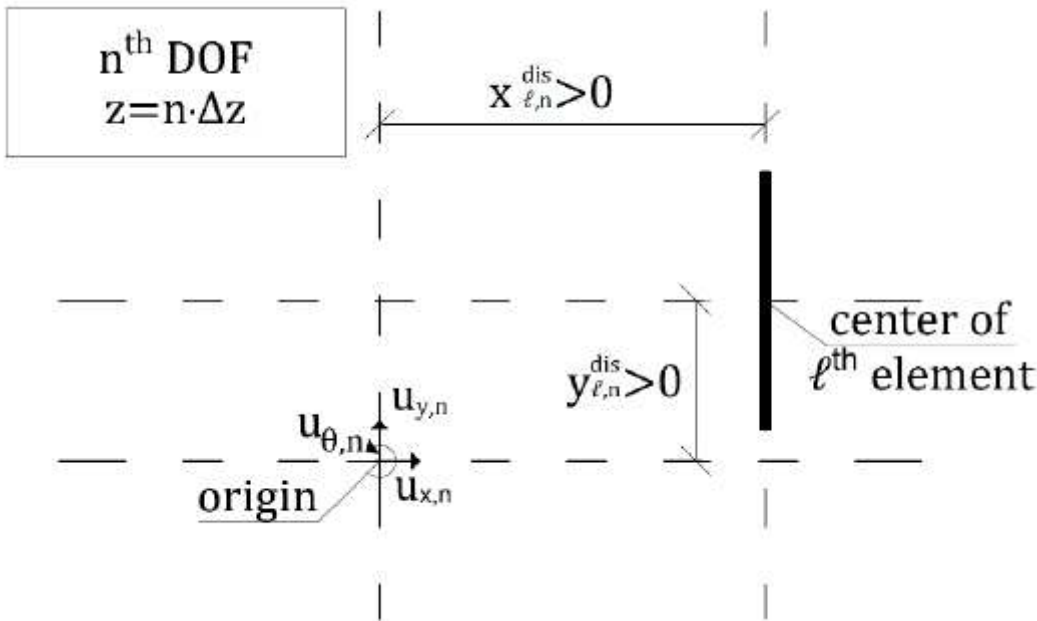


Figure 8

Distances between the  $\ell$ th element and the global DOFs origin

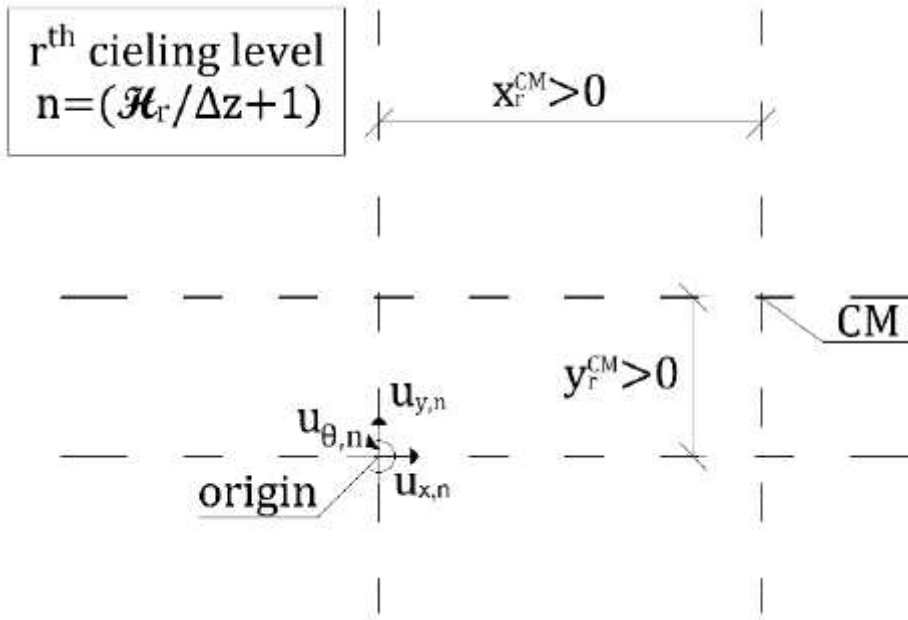


Figure 9

Distances between the CM and the global DOFs origin

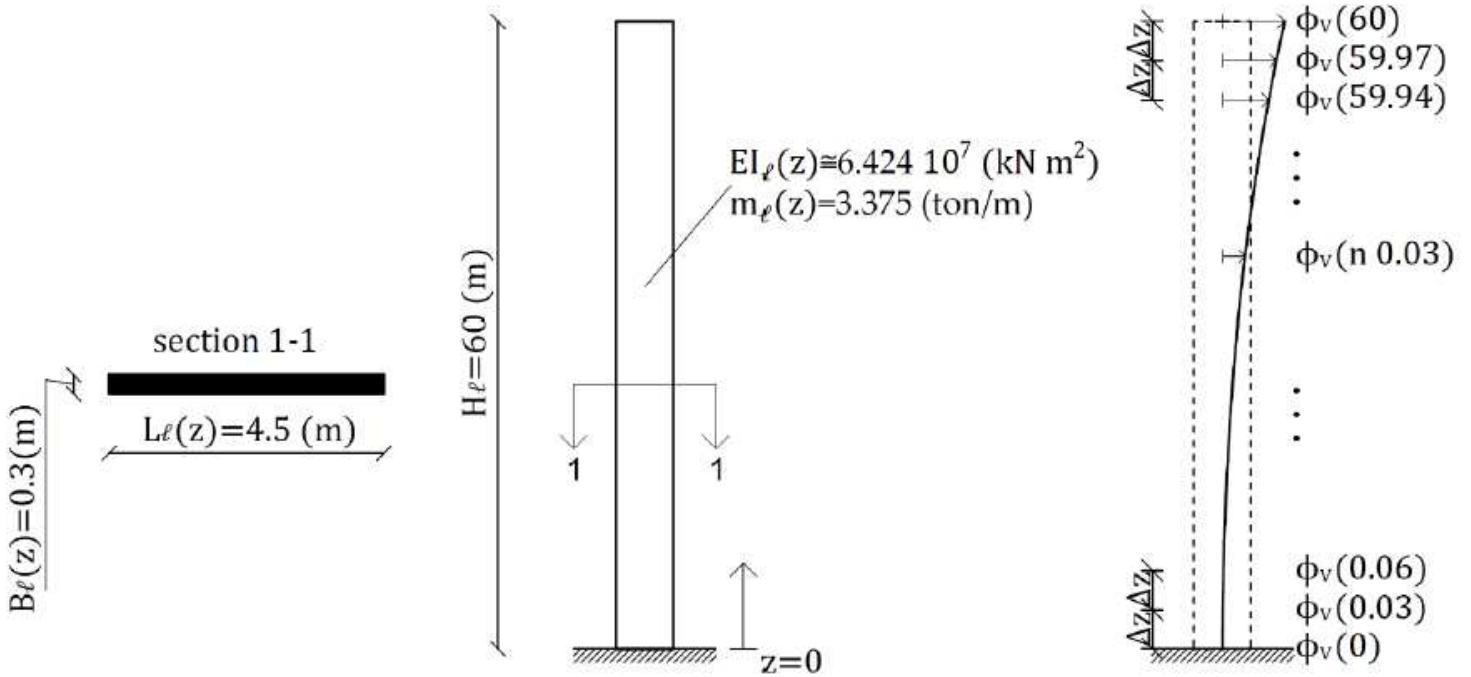
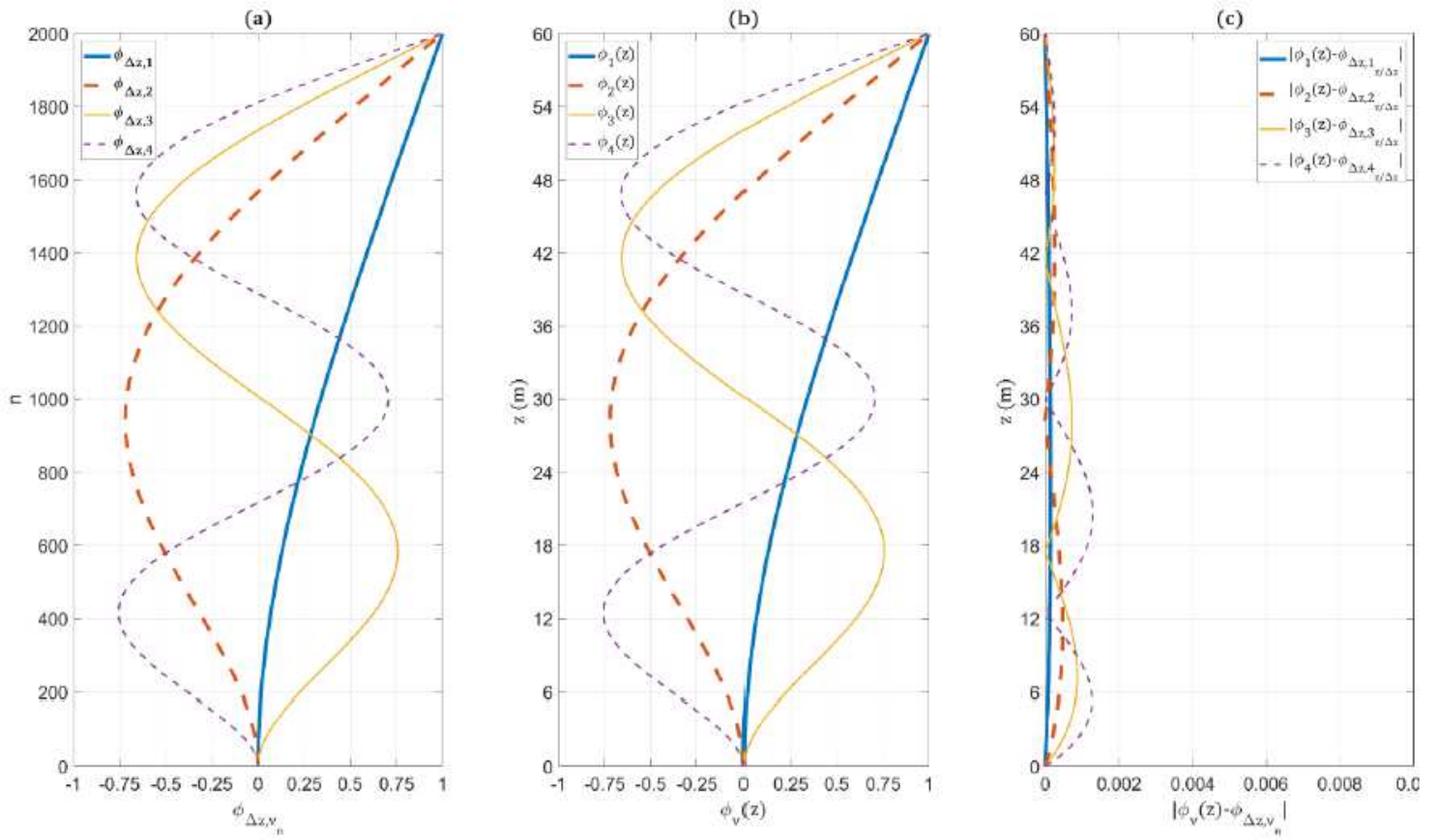


Figure 10

Elevation scheme of the RC cantilever wall



**Figure 11**

Example 1 RC wall's mode shapes  $v=1,2,3,4$ : (a) matrix model, (b) analytical solution, (c) absolute error

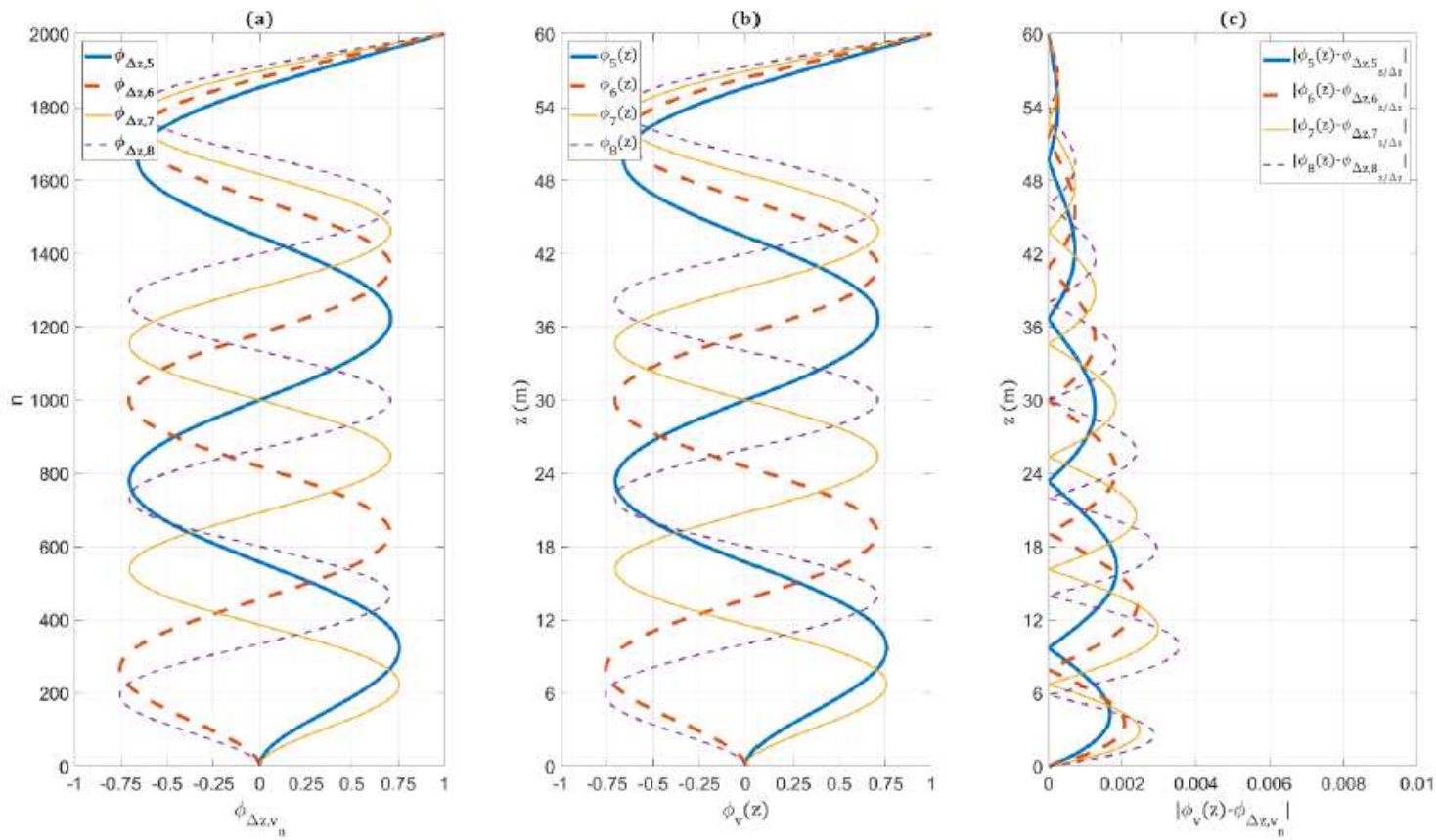


**Figure 12**

Example 1 RC wall's mode shapes  $v=5,6,7,8$ : (a) matrix model, (b) analytical solution, (c) absolute error

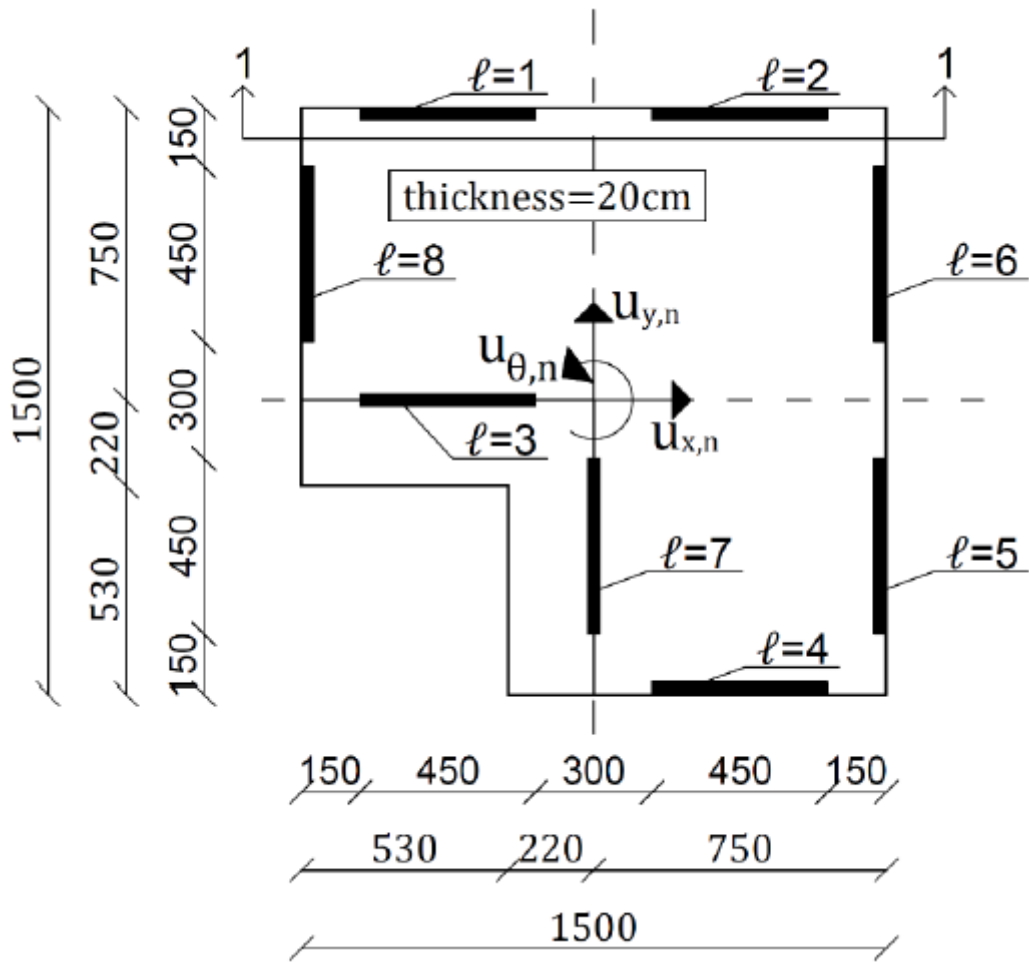
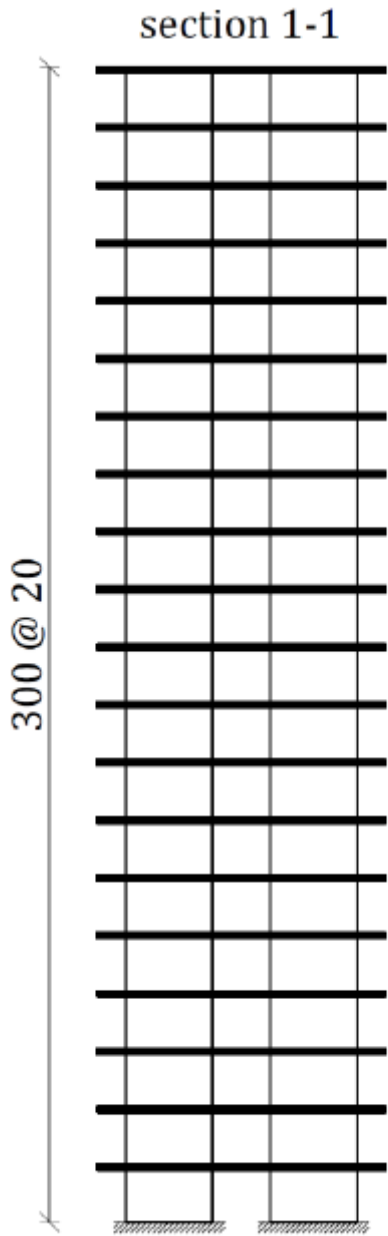


Figure 13

Example 2 asymmetrical floor plan



**Figure 14**

Example 2 building elevation scheme

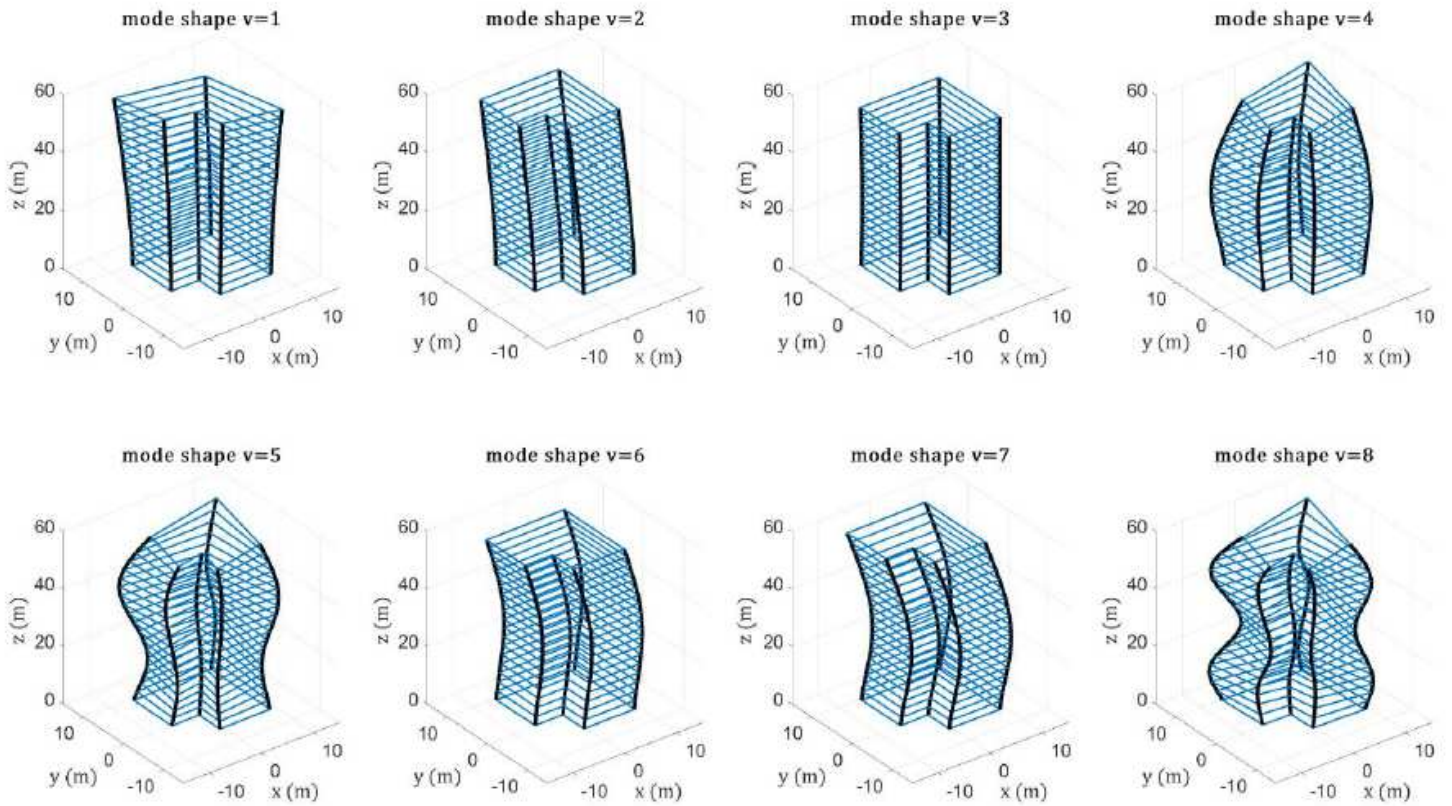


**Figure 15**

Example 2 three-dimensional structure's mode shapes  $v=1,2,3,4,5,6,7,8$

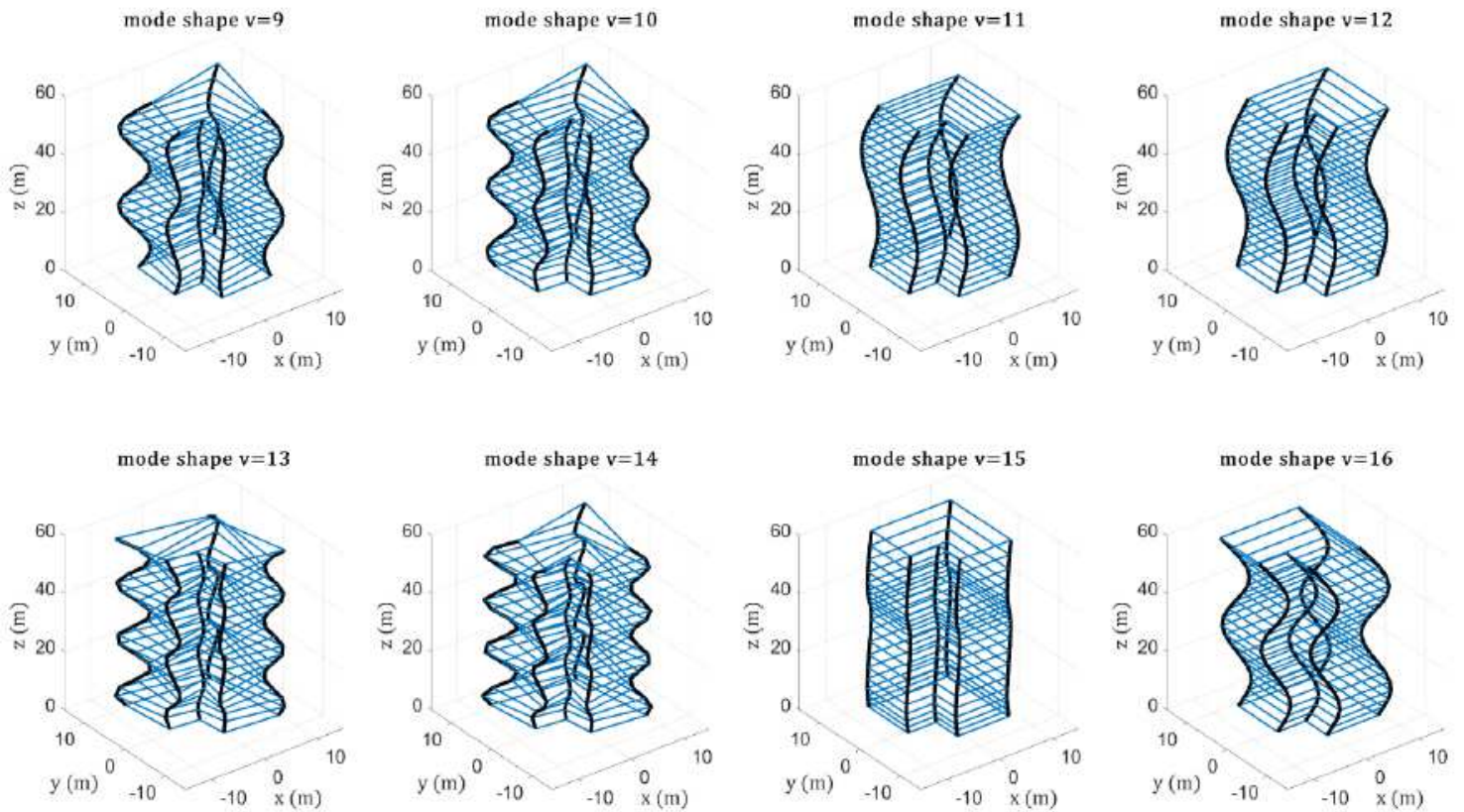


Figure 16

Example 2 three-dimensional structure's mode shapes  $v=9,10,11,12,13,14,15,16$

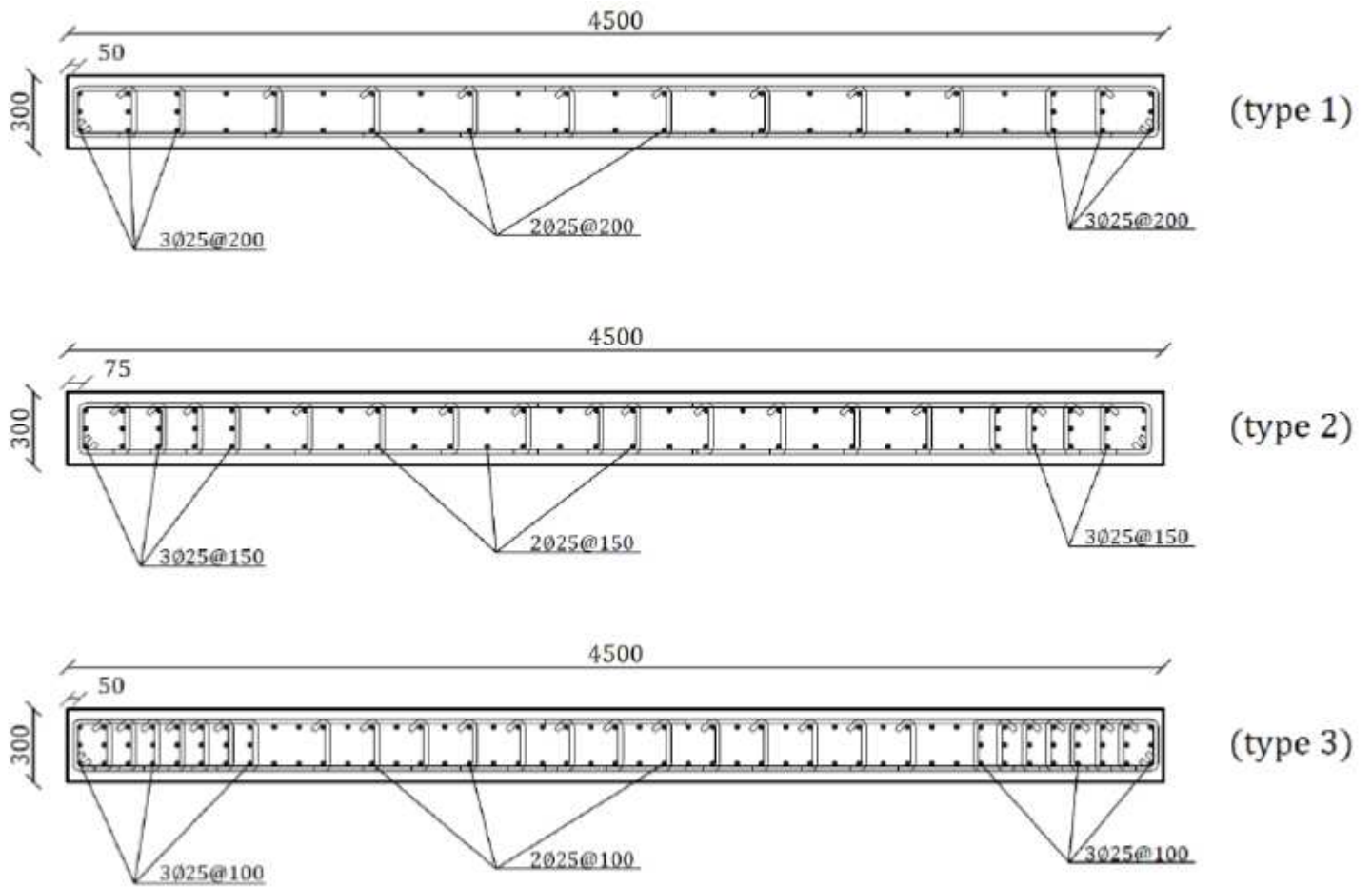
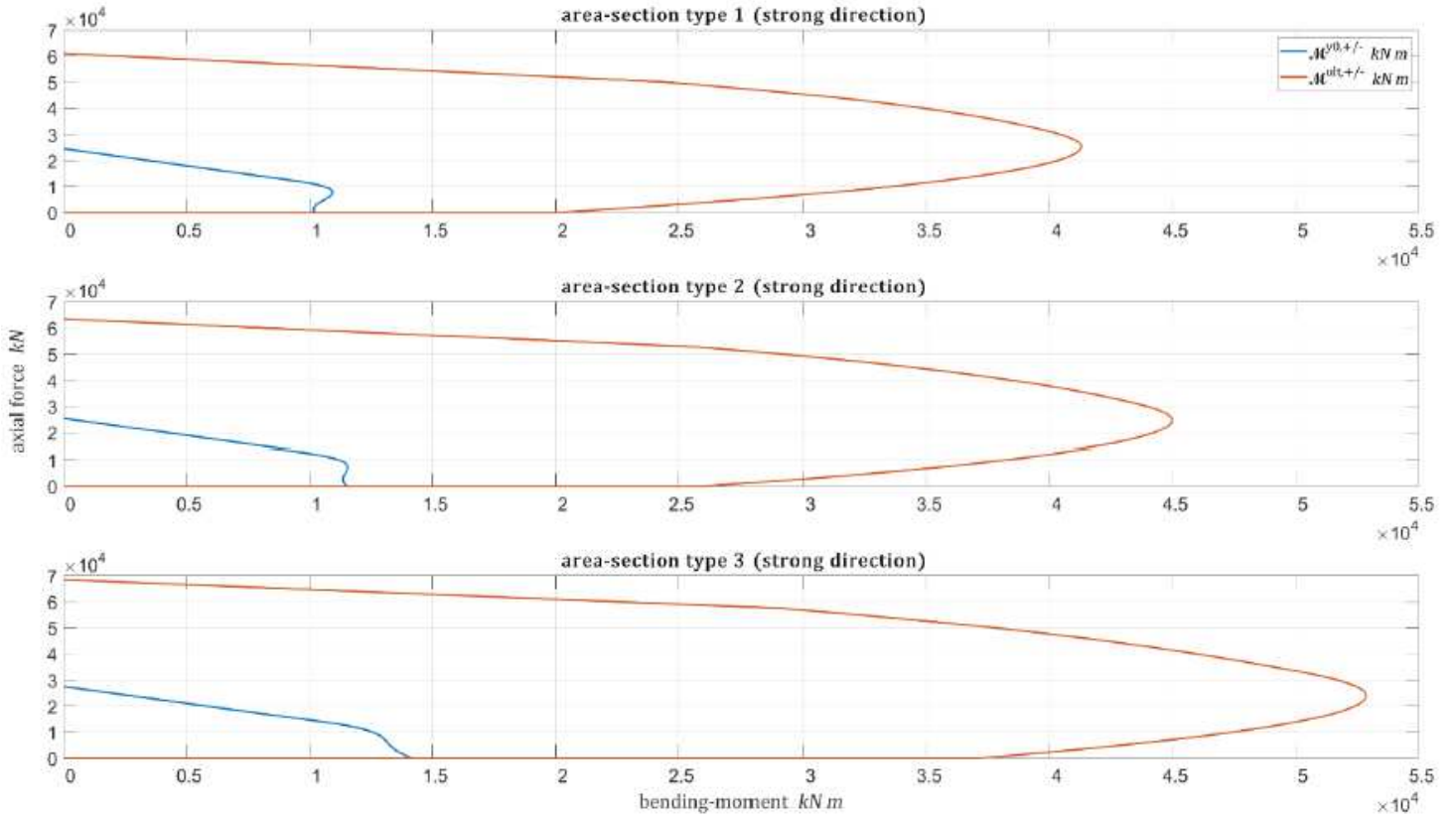


Figure 17

RC cross-section designs of varying vertical steel reinforcement distribution



**Figure 18**

Axial force bending-moment interaction diagrams – strong direction

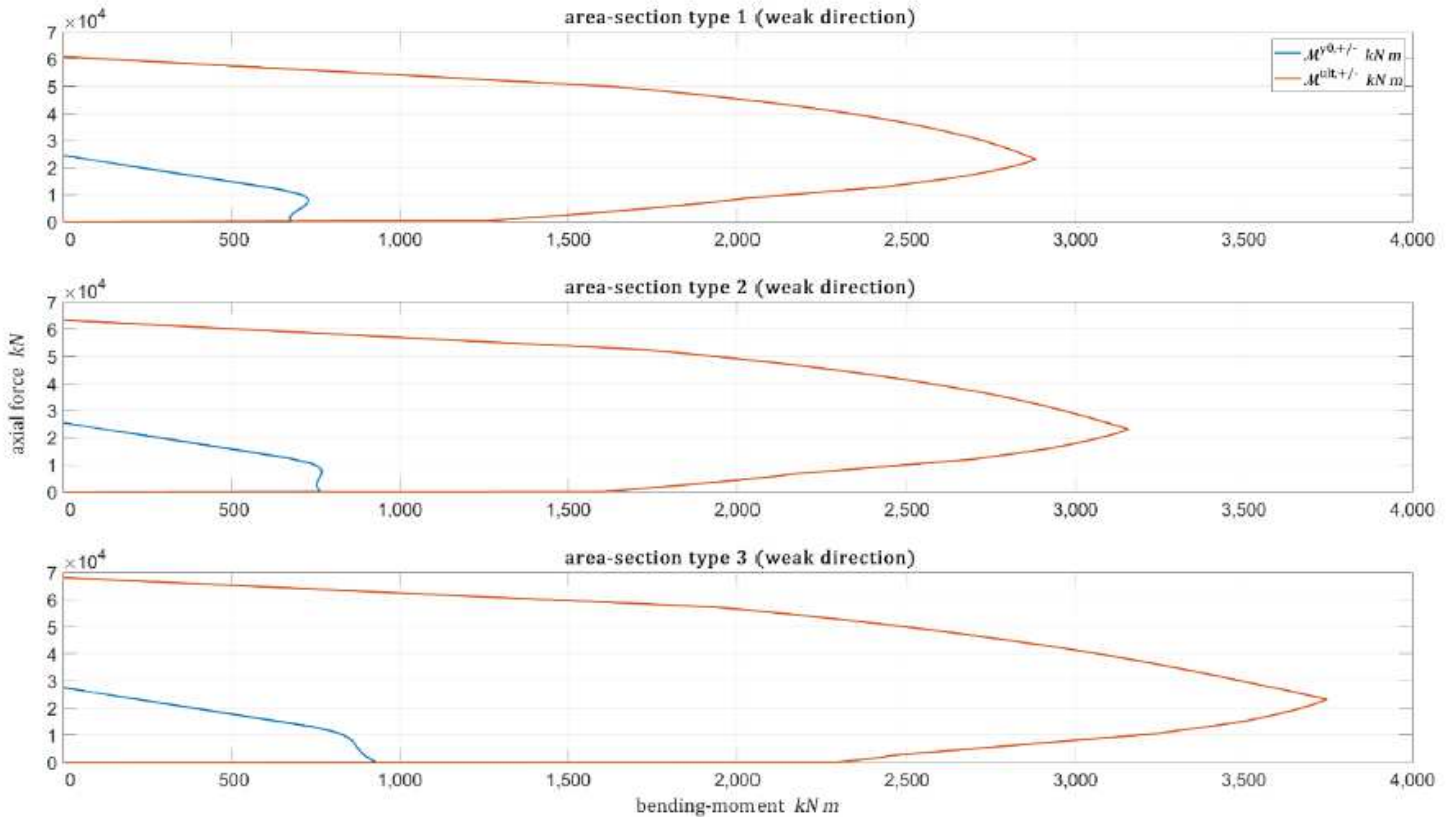


**Figure 19**

Axial force bending-moment interaction diagrams – weak direction

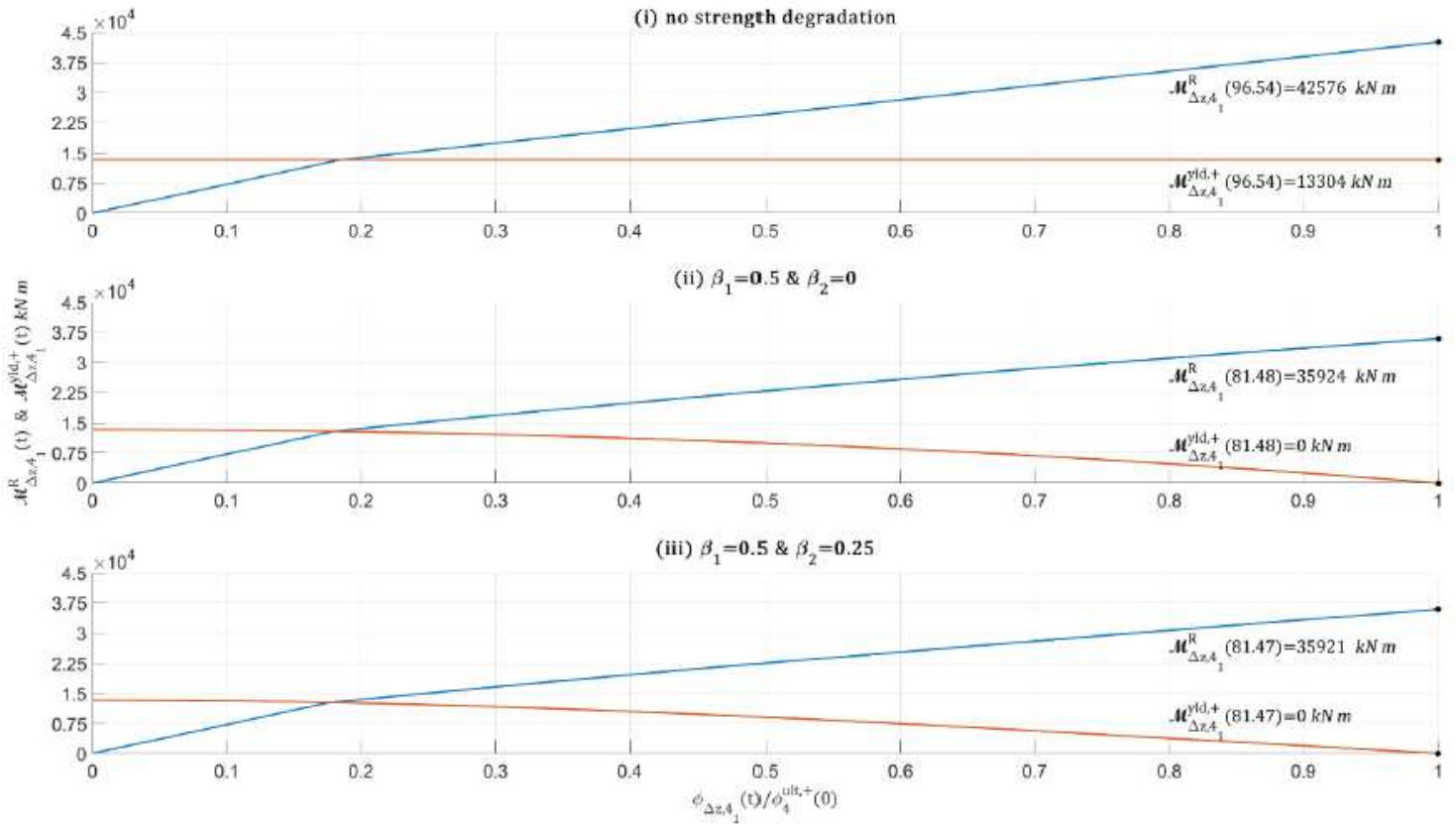


**Figure 20**

Wall  $l=4$  base bending-moment and yielding bending-moment versus normalized 658 bending-curvature

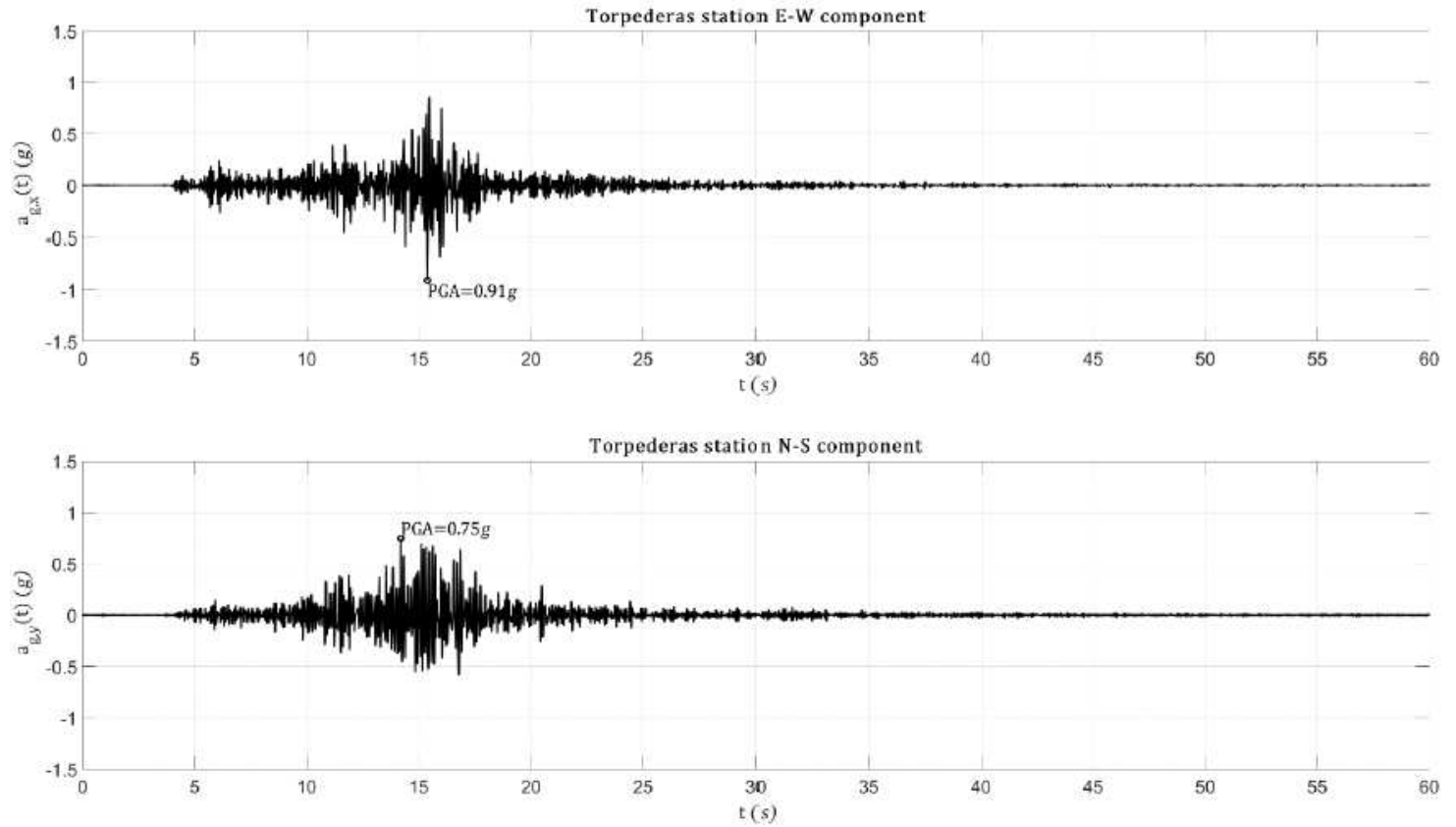


**Figure 21**

Valparaiso earthquake (Chile 2017) ground acceleration records

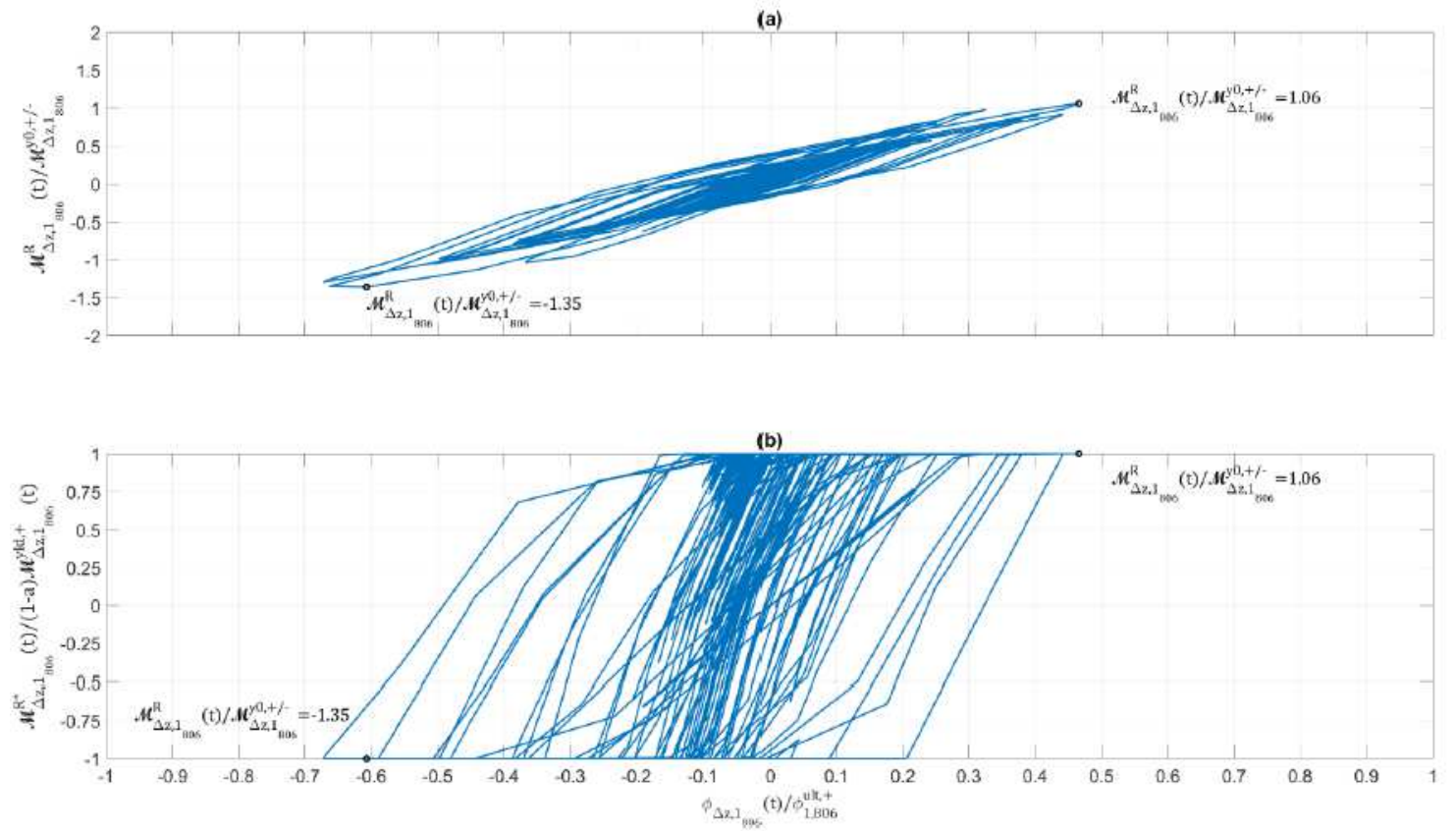


**Figure 22**

Wall  $\ell=1$  cross-section at  $z=48.3\text{m}$   $n=806$ : (a) normalized bending-moment cyclic earthquake response, (b) normalized hysteretic portion of bending-moment

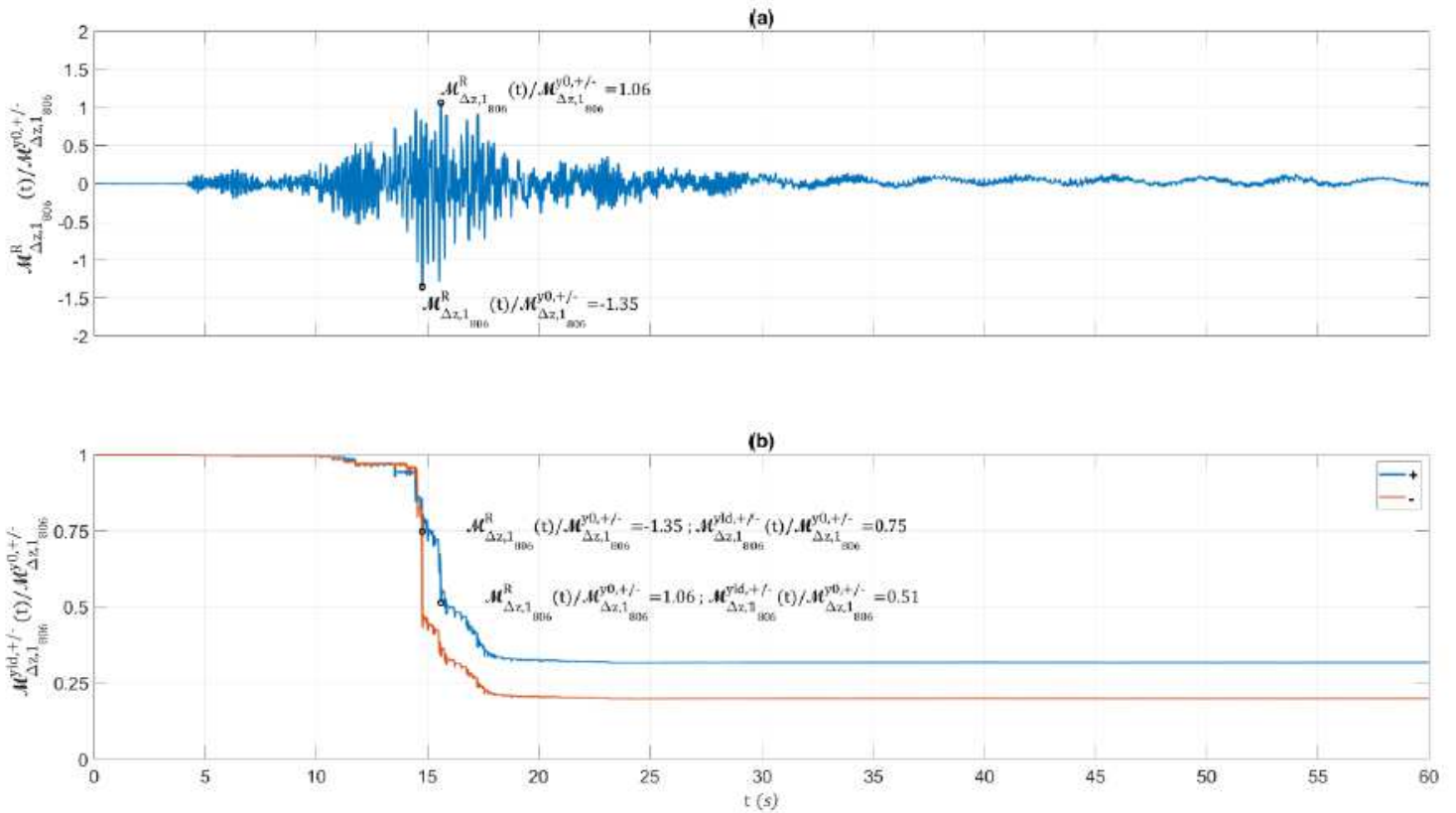


**Figure 23**

Wall  $\ell=1$  cross-section at  $z=48.3\text{m}$   $n=806$ : (a) normalized bending-moment in time, (b) normalized yielding bending-moment quantity in time

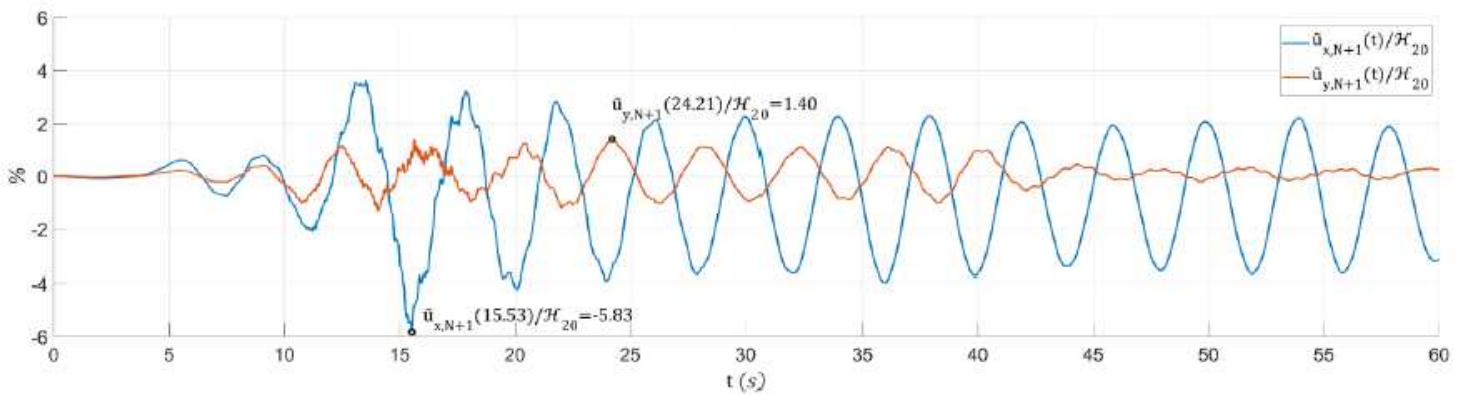


**Figure 24**

Relative roof displacement in the x and y directions

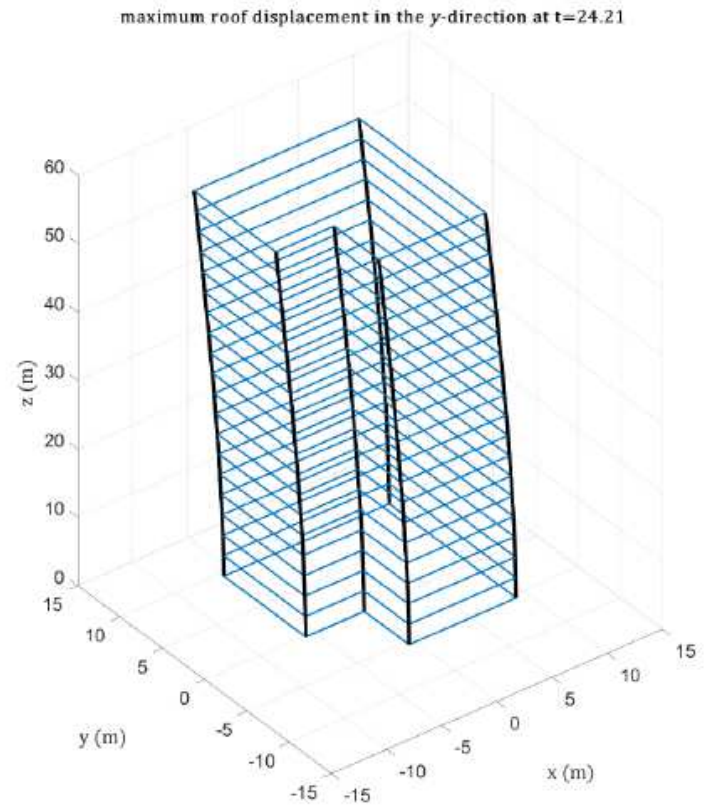
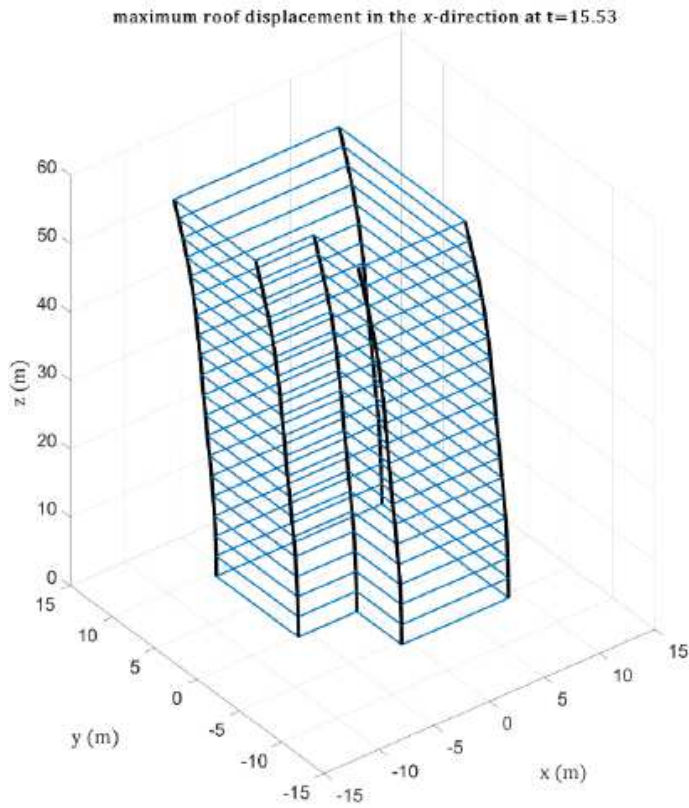


**Figure 25**

Structural deformation at maximum roof displacements

## Supplementary Files

This is a list of supplementary files associated with this preprint. Click to download.

- [Highlights.pdf](#)